The Mechanical Properties of Primary Feathers

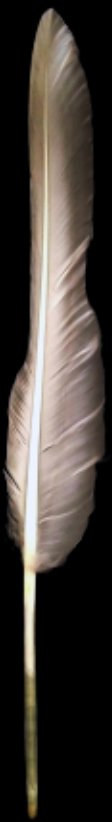

Christian Laurent

The Mechanical Properties of Primary Feathers

Christian Laurent

Published by Independent Publishing Network on 07/07/20

Printed by Book Printing UK

ISBN 978-1-83853-556-8

Supervisors Dr Roeland de Kat
Dr Richard Cook
Dr Richard Boardman
Dr Philipp Schneider
Dr Gareth Dyke
Dr Colin Palmer
Prof. John Dyke

To Alex

"Questions you cannot answer are usually far better for you than answers you cannot question"

—Richard Feynman

Abstract

The mechanical properties of biological materials often surpass their man-made counterparts. However, due to their complexity many of these materials are yet to be fully understood. As a result, their solutions to engineering problems cannot benefit the design of man-made analogues.

Lucas and Stettenheim (1972) stated that feathers are probably the most complex derivatives of the integument to be found in a vertebrate animal and recent work suggests that the longest, stiffest, strongest, and most deserving of mechanical investigation are the flight feathers. These feathers attach to the manus and allow birds to fly. A small amount of research into the broader aspects of their mechanics is already present in the literature, but some of the finer details, such as the shaft's laminar microstructure, have only been superficially explored.

This thesis develops a method based on ultra-high resolution CT scanning to measure the orientation and thickness of layers in the shaft of the first primary feather from three swans. Results show the first quantifiable and repeatable measure of thickness and orientation at different locations in the feather shaft. These results are supported by other techniques and longstanding definitions of the calamus:rachis delimitation are shown to be inappropriate.

Raman spectroscopy is used to show that secondary protein structures vary within, and between layers, and a discussion is presented from a mechanical perspective.

Tensile tests are then completed on smaller pieces of feather

from different places on the shaft and analysed using Classical Laminate Theory.

Results from all three experiments are then discussed together, and suggestions are made to future workers who might further the methods developed as part of this work, and contribute to a new and exciting area of science, in which many international groups are now working.

Acknowledgements

Such a multidisciplinary project would not have been possible without the help and guidance of so many. Among those to whom I am most indebted are Roeland, who taught me that it only takes a *"little"* longer to do things right; to Rich B for his guidance in all things computational, to Gareth for expanding my horizons, to Rich C for always smiling, to Philipp for his help in applying for beamtime, to John for so much of his time, and to Colin, who was the first of us to work on feathers. Also to Ben for his friendship and troubleshooting and to my forever encouraging house mate, landlord and friend Alex, for his contagious enthusiasm. I'm so glad to have spent the last of my formative years with all of you, and so many others.

The project was also supported by the Natural Environmental Research Council [grant number NE/L002531/1], the Engineering and Physical Sciences Research Council [grant number EP/M50814711] and UEFISCDI Romania [grant number PN-III-P4-ID-PCE-2016-0572] and for that I am also grateful.

Thanks also to my examiners, Professor Adrian LR Thomas and Dr Neil Gostling, for their time, effort and interest.

And of course, I would be remiss if I didn't thank my parents: *Thank you,* Mum and *Thank you,* Dad.

Contents

Chapter 1

Introduction

Biological structures exhibit remarkable mechanical properties that often surpass those of their man-made counterparts (*Wegst et al.*, 2015). However, because of their complexity, many of these structures are yet to be fully understood (*Müller*, 2009, *Olorunnisola and Olorunnisola*, 2017, *Wang et al.*, 2018, 2015). If these structures are not further investigated, their evolutionary solutions to engineering problems will never benefit the design of man-made analogues.

As a result, biological structures have enjoyed a small renaissance of scientific interest in the last twenty years (*Boccaccio et al.*, 2011, *Chou et al.*, 2012, *Meyers et al.*, 2013, *Wang*, 2016, *Weaver et al.*, 2012, *Wegst et al.*, 2015), as contemporary techniques in imaging and materials science have developed and become more accessible. Feathers are one of these remarkable structures—seemingly more complex, less studied and less understood than bone or wood (*Meyers et al.*, 2008). They are versatile and allow almost ten thousand species of bird to fly. They support the soaring flight of an albatross, the aquatic takeoff of a heavy swan, and the high-frequency flapping of a hovering hummingbird. All feathers of flighted birds have evolved to be light, stiff and strong (*Wang et al.*, 2011, 2012).

It is now clear that the central shafts of these feathers are a

naturally occurring, fibre-reinforced laminar composite (*Laurent et al.*, 2014) and that the longest, stiffest, strongest, and most deserving of mechanical investigation are the flight feathers. These are found at the end of the wing and play an important role in flight.

Flight feathers and the broader aspects of their mechanics have already been the subject of a small number of publications since scientific interest in biomaterials has been renewed (*Bachmann et al.*, 2012, *Feo et al.*, 2015, *Laurent et al.*, 2014, *Lees et al.*, 2017, *Lingham-Soliar*, 2013, 2017, *Nudds et al.*, 2011, *Wang and Meyers*, 2017), but some of the finer details, such as the laminar micro-structure of the shaft, have only been superficially explored.

To fill this important gap in the literature and bring feathers into sharper focus through an engineering lens, this thesis will consider three questions and compile the answers into a more comprehensive understanding of feather mechanics, which can be expanded upon in future work.

Project aims

1. What is the geometry of the laminar composite in the cortex of a primary flight feather shaft?

2. Are there differences in the structure of the proteins which make up the different layers of the feather shaft?

3. Are the layers mechanically relevant or is the isotropic assumption appropriate?

A key step in this process will be the development of new methods, which are themselves part of the contribution made by this thesis, and which the author hopes will continue to be developed by future workers.

Figure 1.1 shows how the questions relate to one another and to the literature.

The answers to these questions lie at the interface of several scientific areas. This is both exciting and problematic. Alan Turing

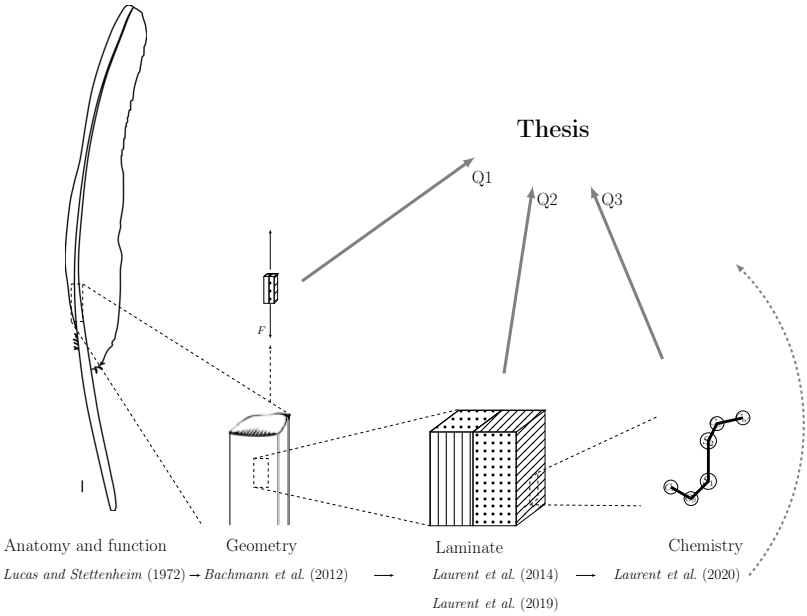

Figure 1.1: *An illustration to frame the current work in context of the literature. The feather is a line drawing of a swan's third primary feather, the scale bar is 10 mm, and it's cross-section is taken from CT scans presented later in the thesis.*

described this problem in the abstract of his own interdisciplinary paper "The Chemical Basis of Morphogenesis" in 1953:

> The full understanding of the paper requires a good knowledge of mathematics, some biology, and some elementary chemistry. Since readers cannot be expected to be experts in all of these subjects, a number of elementary facts are explained, which can be found in text-books, but whose omission would make the paper difficult reading.

The same applies to this thesis, which concerns biology, engineering and chemistry. As with Turing's paper, the work of this thesis might pose more questions than it answers, so it is important to

define the structure and scope of the work to be presented, as well as to be clear on the objectives.

Structure of the thesis Chapter 2 is a literature review that covers the structure of feathers, the proteins from which they are made and the mechanical studies to date. Chapter 3 is a methods section, which covers data acquisition and the subsequent treatment of data from three experiments. Chapters 4-7 present experimental results and discuss them in the context of the questions posed above. Chapter 8 then discusses how the conclusions of the previous chapters fit together to consolidate our understanding of the mechanical properties of primary feathers. Chapter 9 summarises the conclusions of this thesis and considers work to follow.

Some of this work has already been published. Although not wholly included (though some results are revisited) in this thesis, a paper on the nanomechanical properties of bird feather rachises was published in *J. R. Soc. Interface* in 2014 (*Laurent et al.*, 2014). Chapter 3 follows a paper on imaging techniques (*Laurent et al.*, 2019) published in *J. Microscopy*. The results presented in Chapter 5 are on the spectroscopic properties of proteins in layers of the bird feather shaft, and have been published in *J. Structural Biology*.

Chapter 2

Literature

Structure, Material & Mechanics, to date.

Feathers were the subject of a seminal review by *Lucas and Stettenheim* (1972), thirty years before the role of biological structures in such materials became an active research topic. In two volumes that collated more than 100 years of anatomical work, feathers were described in great detail and demonstrated to be probably the most complex derivatives of the vertebrate integument. However, the mechanical properties possessed by these complex tissues were not given any real examination. At a time when the fibre-reinforced plastics industry was still in its infancy, feathers, and in particular the feather shaft, had not been considered from an engineering perspective.

This chapter will introduce the anatomy and terminology presented by *Lucas and Stettenheim* (1972) to describe feathers and show that they are hierarchically complex structures. Then, it will detail the more specialised form of flight feathers and outline a gap in current functional understanding by reviewing the available literature on their mechanical properties. *Mechanical properties*, can be subdivided into *structural properties* and *material properties*, and they will be covered separately. The distinction between them is an important one to make because in the case of feathers, and

many other hierarchical *structures*, considering this difference reveals exactly where there exists a gap in current knowledge. *Structural properties* are macroscopic and are affected by changes in geometry, but *material properties* are intrinsic, being determined by chemical structures, and should be constant. In the case of flight feathers something is known about each but not about how they relate. Section 2.1 will focus on the larger-scale structure of feathers, and Section 2.2 will focus on the much smaller-scale material from which they are made.

These two approaches conceptually meet at a gap in our understanding of feathers, where there is a laminar structure. This laminar structure is not well understood and might vary in structural as well as material properties. The form and function of this laminar structure is the main subject of this work.

2.1 Structure

Primary flight feathers are the feathers on the distal[1] end of the wing. These feathers (usually ten) are denoted P1-10, with P1 corresponding to the feather attached at the very end of the wing[2]. These feathers are adapted for flying and articulate[3] with the bones of the bird's hand. This is so the aerodynamic stresses of flying can be transferred to the skeleton and the musculature for active flight[4] (*Corning and Biewener*, 1998).

The major parts of a flight feather are shown in Figure 2.1. The lateral projections of a feather are called the vane. The vane has two parts, an open *plumulaceous* part which has a fluffy appearance and insulates the bird, and a closed *pennaceous* part which

[1]Distal (adj, anatomy): *away* from the body.

[2]This is consistent with the notation used by most European workers but it should be noted that some American workers use P1 for the primary feather closest to the body (*Lucas and Stettenheim*, 1972).

[3]Articulate (v, anatomy: Where two tissues are attached for a functional purpose.

[4]These are the feathers which bird keepers trim to stop captive birds from escaping.

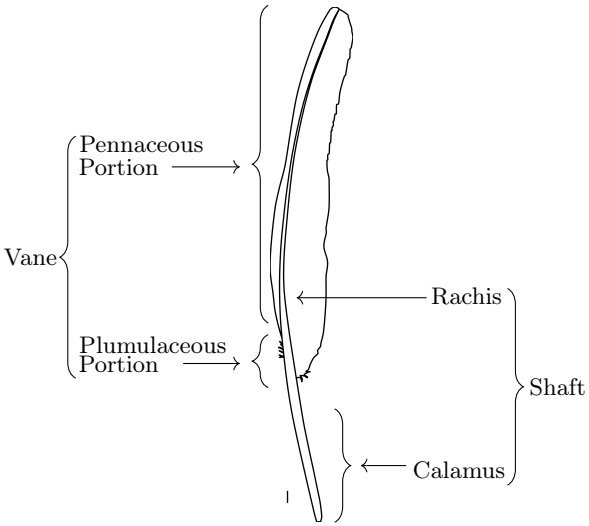

Figure 2.1: *The anatomy of a typical primary flight feather.* ***Scale bar****=10 mm*

acts as the flight surface. The pennaceous part is formed from a three-tiered hierarchical branching system. The largest of these branches—barbs—attach directly to the shaft. Barbules are the smaller secondary projections and hooklets, the tertiary projections, tightly couple the barbs and barbules to form the wind-tight flight surface (vane). The vane is strongly attached to, and supported by, the shaft.

The central shaft is the longitudinal axis of the feather. It has two parts, the rachis and the calamus. The calamus is the name given to the proximal part of the shaft that inserts into a follicle beneath the skin. The proximal[5] end articulates with the phalanges and minor metacarpus. It has a varying oval cross-section (*Lucas and Stettenheim*, 1972) and is essentially hollow (see Figure 2.2) except for the membranous pulp caps left over from the formation of the feather.

[5]Proximal (adj, anatomy): *close to* the body.

The rachis is the distal segment of the shaft that protrudes from the skin. The cross section is normally quadrilateral and most birds present a ventral[6] groove and relatively thicker dorsal[7] and ventral walls, which are shown schematically in Figure 2.2. The rachis is always filled with a medullary pith and accounts for 70–80% of the shaft's total length in most birds. However, there is no strong consensus which defines exactly where the calamus ends and the rachis begins. Some birds have more deeply articulated feathers or the vane forms more distally to accommodate more insulation. Some workers propose a zone of discontinuity (*Maderson et al.*, 2009), which this work will argue is more appropriate from both a functional perspective and a morphogenetic perspective. However, probably the most common definition from *Proctor and Lynch* (1993) will be used *i.e.* the transition point will be the superior umbilicus, a small opening on the ventral surface that forms from the epithelial tube from which a feather develops.

The calamus, the rachis and the vane are all made from a fibre-reinforced composite. In the rachis and the calamus, the composite forms layers (the composite itself will be discussed in Section 2.2). These layers were first reported by *Earland et al.* (1962b), who used X ray birefringence to observe two layers in the calamus of a feather from a white goose (*Anser anser domesticus*), although it was not clear from which feather this sample was removed. Three layers (four including a superficial membrane) were reported from X ray diffraction work by *Busson et al.* (1999) on a piece of feather shaft from the tail feather of a peacock, *Pavo cristatus*, though no directional information was given and it is not reported which feather was studied[8]. Later, between two and four layers have been identified in the primary calami of the mute swan (*Cygnus olor*), partridge (*Perdix perdix*), and bald eagle (*Haliae-*

[6]Ventral (adj, anatomy): the belly or lower surface of an animal or appendage.

[7]Dorsal (adj, anatomy): the back or upper surface of an animal or appendage.

[8]Tail feathers follow a similar naming convention to the primaries and are denoted T1-T6 (left or right), with T1 being the central tail feather.

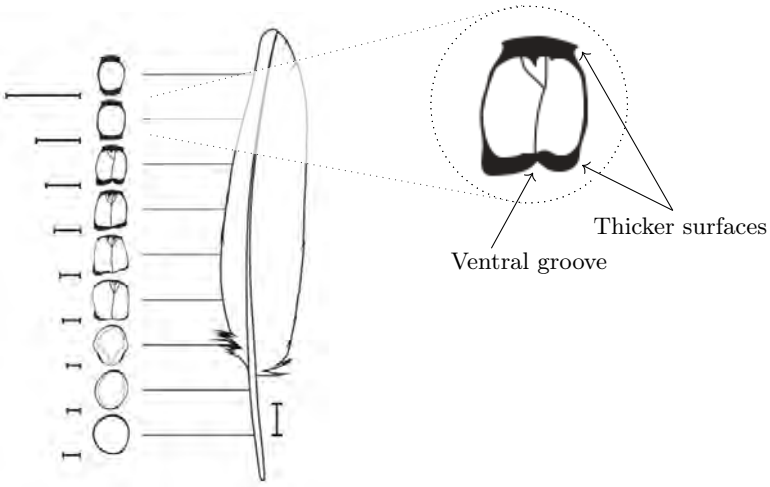

Figure 2.2: *Cross sectional geometry at 10% increments along the rachis. This shows that the calamus is a hollow tube but the rachis is a an adapted quadrilateral. The rachis also has thicker dorsal and ventral walls, and a ventral groove. Modified from* Bachmann et al. *(2012).*
Scale bars *1 mm.*

tus leucocephalus) by *Laurent et al.* (2014). The study by *Laurent et al.* (2014) presented some directional information, which was inferred by computed tomography (CT) scanning and nanoindentation measurements, although no clear pattern could be discerned between different birds at the time of writing. The CT data from this study (*Laurent et al.*, 2014) is reproduced as Figure 2.3, where three layers can be seen in a swan *C. olor* rachis. This rachis is illustrated in Figure 2.4, and the original paper reported three layers, oriented at -5°, 0°and 45 °from the long axis. This data will be reinterpreted in Chapter 4.

Two recent studies (*Lingham-Soliar et al.*, 2010, *Lingham-Soliar and Murugan*, 2013)[9] have presented Scanning Electron Micro-

[9]Prof. Lingham-Soliar sadly passed away in 2018 after a long career working on the vertebrate integument, but his work, and pictures of feather shafts remain.

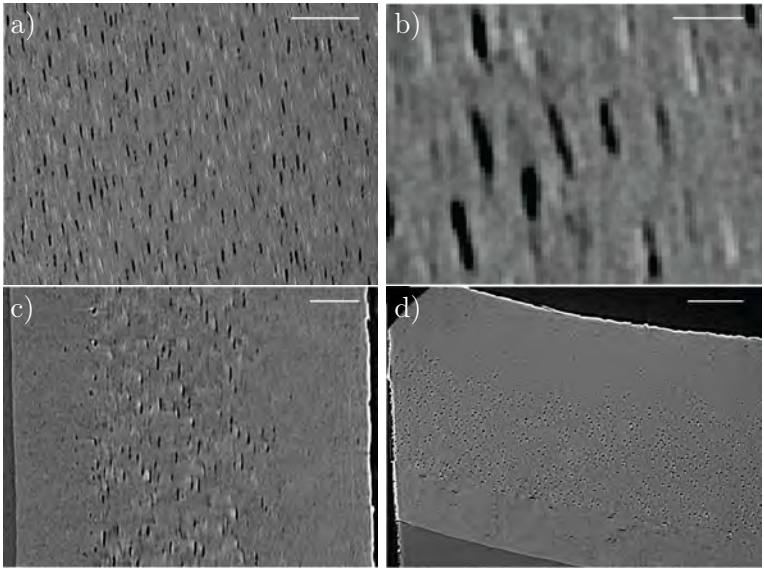

Figure 2.3: *Four slices of a micro-Computed Tomorgraphy, μCT, reconstruction show that voids and fibres can reveal laminar geometry, reproduced from* Laurent et al. *(2014). Subfigure **a)** is a view of the central layer, which clearly shows oriented voids. Subfigure **b)** is a magnified view of **a)**, which shows the void - fibre texture more clearly. Subfigure **c)** shows a long section, in which fibres of the central layer run parallel to the feather axis. Subfigure **d)** is a cross-section, which shows the void spaces and fibres of the central layer end-on.*
***Scale bars** a) 100 μm, b) 20 μm, c) 50 μm and d) 100 μm.*

graphs (SEMs) of microbially degraded primary feathers from a chicken (*Gallus gallus*). These images show at least two layers in the dorsal part of the rachis (*Lingham-Soliar et al.*, 2010), and a single, woven, layer in the distal side-wall (*Lingham-Soliar and Murugan*, 2013).

In summary, the presence of layers has been confirmed in multiple taxa[10] using different techniques. However each of these stud-

[10]Taxa (n, pl, Biology): a group of one or more populations of an organism or organisms seen by biologists to form a unit. s. taxon.

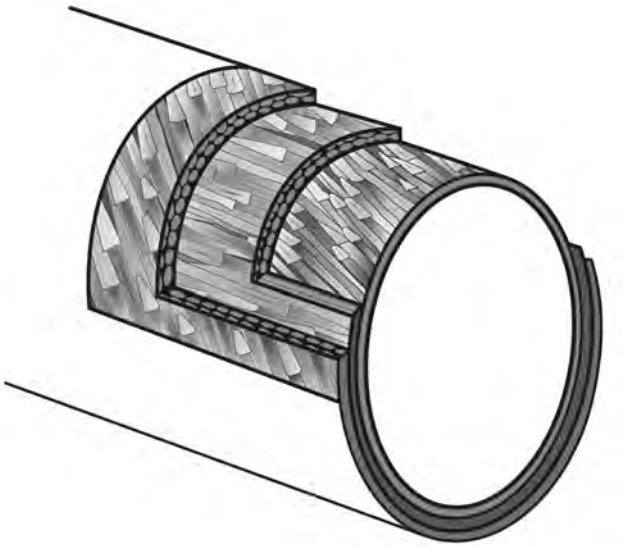

Figure 2.4: *A cartoon which shows an interpretation of the computed tomography (CT) data presented in Figure 2.3. It suggests there are three layers of fibrous material in the calamus of a swan's primary feather.*
Reproduced from Laurent et al. *(2014)*

ies only considered a small sample or even a single piece of feather and it is unclear whether the number, orientation and thickness of layers varies within and between species.

2.2 Material

Feathers are composed almost completely of proteins. Therefore, it is first necessary to understand the basic concepts of protein structure before the structure of the tissues made from those proteins can be considered. A more complete description of protein structure than the overview presented in this section is given in textbooks on structural biology, such as *Buxbaum* (2015).

Basic Concepts of Protein Structure

Amino acids are the building blocks of a protein. They have three functional groups, which are illustrated in Figure 2.5a; an amine group - NH_2, a carboxyl group - COOH, and an R group, which represents a varying side group. There are 20 different R groups in biological amino acids, and the different components of these groups determine the properties of the amino acid.

Two amino acids can combine by condensation of the amine and carboxyl groups with loss of water to form a strong bond, see Figure 2.5b. A series of condensations of this type gives rise to a polymer of amino acid residue. The polymer formed is called a *polypeptide* or a backbone and is the primary structure of a protein.

As well as the peptide bond, inter-proton hydrogen bonding involving the amino and carbonyl groups can occur and this results in local folding to form a secondary structure. Two common folding motifs are the α-helix and the β-pleated sheet[11].

The folding of the polypeptide introduces new attractive forces within the molecule when it places the 'R' groups of non-adjacent residues close together. Also, the amino acid cysteine contains a thiol (S-H) group. This can dimerise on oxidation with loss of water to form a dimer called *cystine*. This molecule contains a cross-link (CC-S-S-CC) called a disulphide bridge (*Essendoubi et al.*, 2019).

This bridge can exist in three conformations, pictured in Figure 2.6, each of which confers a different amount of reinforcement to the protein structure. The proportions of these conformations can also be used to infer stability of the disulphide bonding, which correlates with mechanical properties.

The amino acid methionine also contains sulphur but cannot form a disulphide bridge because a methyl group ($-CH_3$), attaches to the sulphur in a thiomethoxyl group ($-SCH_3$). Methionine is

[11]The $\alpha, \beta, \gamma...$ notation used here does *not* refer to the $\alpha, \beta, \gamma...$ carbon atoms in the amino acid residue but to the types of secondary structures in proteins. This nomenclature has been retained from very early work on protein structure by *Astbury and Woods* (1934)

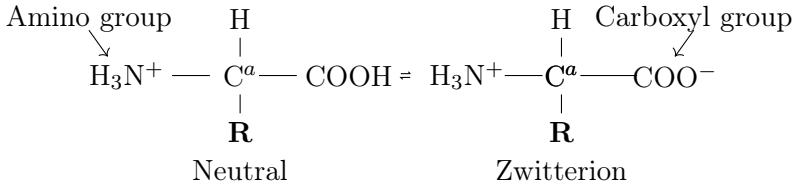

a) The Zwitterion Structure of a protein

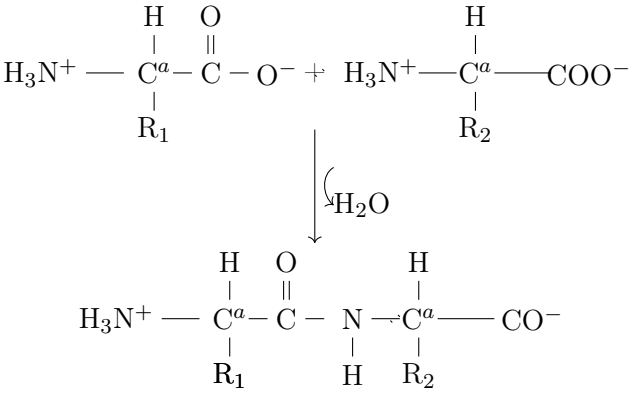

b) The formation of a peptide bond from two amindo acids.

Figure 2.5: ***a)*** *The Zwitterion structure of an amino acid. 20 different acids appear in the genetic code, polymers of which form proteins. The central α-carbon atom and the peptide linkage forms the polymer backbone, which folds into common motifs because of H-bonding along backbone groups. Interactions between the functional groups within the 20 different amino acids determine tertiary protein structure.* ***b)*** *The formation of a peptide bond from two amino acids.*

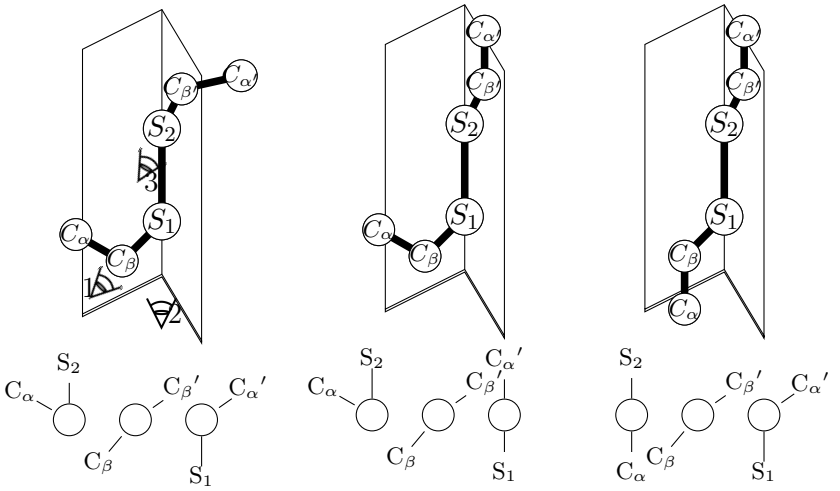

(a) *G-G-G* **(b)** *G-G-T* **(c)** *T-G-T*

Figure 2.6: *A diagrammatic representation of CC-S-S-CC bond conformations of the disulphide bond in keratins* ***a)*** *gauche-gauche-gauche,* ***b)*** *gauche-gauche-trans and* ***c)*** *trans-gauche-trans. Three bond angles are shown beneath each subfigure, which correspond to viewpoints 1,2 and 3, which are illustrated in* ***a)****. Reproduced from* Akhtar and Edwards *(1997)*

more hydrophobic, sterically[12] larger and much less reactive than cysteine. Bonding between non-adjacent groups (*e.g.* by a disulphide bridge) causes the folded polypeptide to pack in three dimensions and this determines the shape and function of the protein. Individual proteins or families of proteins are named according to this tertiary structure, which form part of a multiple-protein complex.

Feather Keratin and Fibrous Superstructure

This section will use the basic concepts and terminology of protein structure covered in the previous section to describe the molecular structure of feather keratins and the interactions between

[12]Steric (adj, chemistry): relating to the spatial arrangement of atoms

molecules in a feather. As the term *feather keratin* suggests, keratin is not a single protein but a family of proteins. Clades[13] of particular keratins can be associated with phylogenetic[14] animal groups *e.g.* the evolution of β -keratin is roughly parallel to the evolution of reptiles (*Dalla Valle et al.*, 2010). This means that keratins can be considered both generally and specifically.

Generally, keratins are filament proteins found in the epidermii of all vertebrate taxa (*Fuchs and Marchuk*, 1983) and mostly consist of the amino acids valine (Va), leucine (Leu), serine (Ser), proline (Pro), aspartic acid (Asp) and glutamic acid (Glu), with some cysteine (Cys). As a group they are thought to be highly conserved. They have shared a similar amino acid sequence since their divergence from a common ancestor 280 million years ago (MYA) (*Fraser and Parry*, 2011, *Greenwold and Sawyer*, 2011).

Specifically, there are small differences which can be very significant but in order to discuss these differences it is necessary to be careful with keratin names. Conventions can refer to structures or to the phylogenetic group to which the protein belongs and naming schemes also change as more is learned about the protein. Ideas and results from experiments on one taxon of keratins may or may not be likely to apply to others, and this likelihood will vary with cladistic distance.

β -keratin and α-keratin refer to β-pleated sheet and α-helix secondary structures, usually in the context of sauropsid[15] keratins. The β -keratin and α-keratin terms are not used for synapsid[16] keratins. These are instead divided into (soft) cytokeratins (α-keratins) and Keratin Associated Proteins, KAPs (β-configured

[13]Clade (n, biology): a branch on the tree of life - a group of organisms which consists of a common ancestor and all its direct descendants.

[14]Phylogenetic (adj, biology): relating to the evolutionary history of groups of organisms

[15]Sauropsida ("lizard faces", n., biology): a taxonomic clade which includes all living reptiles and birds.

[16]Synapsida ("arch group", n., biology): a group of animals that includes mammals and every animal more closely related to mammals than to birds or reptiles. They are diagnosed by an opening in the skull, which has a prominent arch

keratins). It has been argued that the cytokeratin / KAPs terminology should be used in future study of sauropsid keratins because the α-keratin / β -keratin distinction is an oversimplification (*Alibardi and Toni*, 2006) and is insufficient to explain the variability and complexity of keratins in a polyphyletic[17] group. Feather keratins (or sometimes, F-keratins) are one sub-family of four β-configured keratins (scales, feathers, claws, hairs) in the avian genome and are only produced in feathers. F-keratins, the most derived sub-family, are more closely related to feather-like keratins, claw keratins, and scale keratins, in that order (*Greenwold and Sawyer*, 2011). Recent work has even gone so far as to identify a number of genes which code for the production of keratin in different areas of the chicken integument (*Ng Siang et al.*, 2014). Three genes are identified for the production of β -keratin in flight feathers, on chromosomes 2, 6 and 25. These genes and a large number of diad contributions that they can produce are thought to be responsible for the morphological and structural differences between contour feathers and flight feathers. Genes which produce α-keratin were conserved between different types of feather and it is therefore thought that α-keratin production is less important in the context of feather variation.

Thankfully, differing terminologies are not a huge problem in learning about the structure of F-keratins because a lot of the work which describes their structure shares two common lead authors. Professor Bruce Fraser[18] and Professor David Parry have been working on the structure of sauropsid keratin since the late 1950's (*Fraser and Parry*, 2019, *Fraser and MacRae*, 1963, 1976, *Fraser et al.*, 1971, 1973a,b, *Fraser and Parry*, 1996, 2008, 2011) and two of their most recent papers specifically address feather keratins.

That work contributes to the e contemporary understanding

[17]Polyphyletic (adj, biology): derived from more than one common evolutionary ancestor or ancestral group and therefore not suitable for placing in the same taxon

[18]Prof. Fraser sadly passed away in the process of publishing his most recent paper in 2019, nearly 70 years after he published first paper in 1950.

that the feather keratin complex is a dimer[19] of parallel or anti-parallel β-sheets which is 2.4 nm in cylindrical diameter. These dimers assemble to form a filament, which has four dimers per turn, a pitch length of 9.6 nm and a unit length of $\approx$45 nm.

The major components are α-keratin and β -keratin , which are encoded in multigene families [10]. β -keratin adds more rigidity than α-keratin . Cellular and biochemical studies have shown that α-keratin has played an important role in the early formation of the rachis, barbs, and barbules (*Alibardi and Toni*, 2006). The exact structure of feather keratin remains unknown, although a reasonable model for the dominant protein secondary structure has been proposed based on X-ray diffraction data (*Fraser and Parry*, 2008, 2011). Results show that feather keratin is tightly packed in β -sheet s into a coiled polypeptide chain that exhibits a high degree of disulphide cross-linkages, hydrophobic interactions, and hydrogen bonds (*Pabisch et al.*, 2010, *Zhao et al.*, 2012). This confers mechanical strength and chemical resistance, and the structure is largely insoluble due to the disulphide bridges. Structural studies have shown that in birds the β -keratin chain is typically 100-200 molecules long and contains a central conserved region of about 34 residues. This is believed to adopt a twisted antiparallel β -sheet conformation with three central strands and two partial outer strands (*Calvaresi et al.*, 2016, *Fraser and Parry*, 2019, 2011). Attached to the central region (or domain) are Amino-terminal and Carboxy-terminal domains. In the Amino-terminal domain, there are two subdomains (A and B) while in the Carboxy-terminal domain two subdomains (C and D) have been identified. Subdomain B is not present in birds. The central domain of the β -keratin chain is rich in β and turn structures, and the rest of the structure contains mainly random coil units with some β-propensity. The most likely β-containing region in the feather shaft, apart from the conserved central 34-residue domain, is the variable length segment C, with its potentially β-favouring se-

[19]Dimer (n., chemistry): a compound formed by two subunits (monomers). Many units form a polymer.

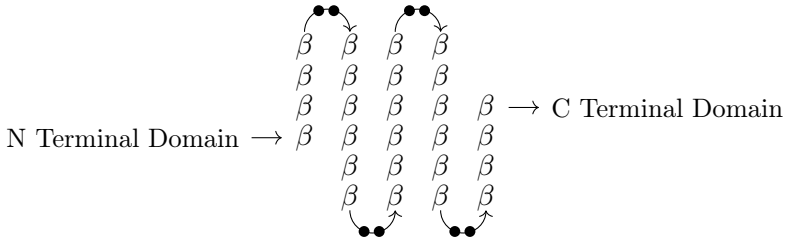

Figure 2.7: *Schematic diagram of β -keratin filament structure. This shows five contiguous segments of β-sheet tending residues, separated by turn-tending residues (filled circles) to form a filament-matrix texture from the* same *protein. Modified from (*Fraser and Parry, *2011)*

quence repeats (*Fraser and Parry*, 2019, 2014, *Parry et al.*, 2019).

Even more information can be found on how these residues form secondary structures by using vibrational spectroscopy (*Barth and Zscherp*, 2002). X-ray diffraction and vibrational spectroscopy have been applied to feather keratins in recent years, though there is not yet any work which relates results to mechanical properties of an intact feather. So far, work compares secondary structures to proteins from different animals (*Akhtar and Edwards*, 1997), investigates pigmentation (*Galván et al.*, 2013, *Thomas et al.*, 2013), hydration (*Khosa et al.*, 2013) or proteins in solution (*Church et al.*, 2010). While the conclusions of these studies are not relevant to the present work, their work sets out which regions of the vibrational spectrum contain relevant information and describe the methods used in analysing spectra. These workers also assign molecular vibrations to particular structures and set the stage for work that could relate molecular vibrations to protein structure and ultimately to mechanical properties.

Figure 2.7 shows that the β-tending segments are separated by turn tending residues which make the unit twist. The molecule is about 100 residues in length. Approximately 40 residues make up the filament and the remaining residues *of the same protein* compose the matrix.

Pabisch et al. (2010) reported that differences in the matrix

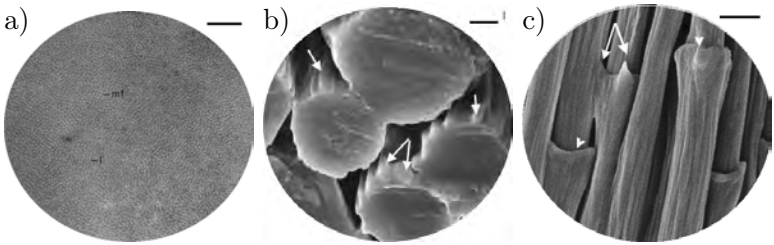

Figure 2.8: ***a)*** *A transmission electron micrograph (TEM) from* Earland et al. *(1962a), which shows intermediate filaments, the smallest structural element and the filament matrix from an ultra-thin section of feather keratin.* ***b)*** *A scanning electron micrograph (SEM), which shows a cross section of a group of fibres from G. gallus . In this figure, arrows indicate macrofibrils.* ***c)*** *Another SEM of G. gallus , showing whole keratin fibres, arrows point to syncitial nodes. Figures b and c are from* Lingham-Soliar et al. *(2010).*
Scale bars a) *100 nm,* ***b)*** *1 µm and* ***c)*** *5 µm.*

influence the axis of the filament, giving rise to changes in its bending resistance along the length of the feather.

Weiss and Kirchner (2011) have demonstrated that plasticity of the feather results from breaking electrostatic bonds. Therefore, the filament-matrix texture, or filament composite, deserves its own place in the hierarchy of feather shaft structural complexity, and is a synapomorphy[20] of sauropsid β -keratin (*Fraser and Parry*, 2011) because the filament-matrix complex in mammals consists of about 20 different proteins (*Alibardi and Toni*, 2006).

Filshie and Rogers (1962) were the first to image this texture using Transmission Electron Microscopy (TEM). Their image is reproduced here as Figure 2.8a.

This filament composite arranges itself in tows[21] (d = 0.1 µm) (*Lingham-Soliar et al.*, 2010, *Wang and Clarke*, 2015). These form

[20]Synapomorphy: a characteristic present in an ancestor and shared exclusively (in more or less modified form) by its evolutionary descendants, which can be used to diagnose membership of a certain clade.

[21]Tows (n., chandlery): A short fibre used to make yarn.

a roving[22] of macrofibrils (d = 0.5 µm) (*Lingham-Soliar et al.*, 2010), which in turn form a fibre (d = 5 µm) (*Lingham-Soliar et al.*, 2010). It has also been reported that these fibres change direction along the length of the shaft (*Cameron et al.*, 2003) but layers are not mentioned in this work. It now seems that layers might have much more influence on the direction of fibres. This hierarchy can be seen in Figure 2.8, which shows a transmission electron microscope (TEM) and scanning electron microscope (SEM) image, recorded after the supporting matrix has been degraded. The matrix protein which has been removed in the sample used in Figures 2.8b and 2.8c (*Earland et al.*, 1962a) seems to be a different protein from the matrix described by (*Fraser and Parry*, 2011). It is sometimes described as amorphous (*Lingham-Soliar*, 2013, 2017, *Lingham-Soliar et al.*, 2010, *Lingham-Soliar and Murugan*, 2013, *McKittrick et al.*, 2012) and sometimes referred to as γ-keratin . However, almost no work has investigated this protein. It should be noted that this is not the same matrix which links the filaments. The late *Lingham-Soliar* (2017) postulated that it might be composed of the residual cytosol[23] of keratinocytes and effete organelles. There has been some investigation into the matrix of human hair (*Kadir et al.*, 2017), which shows that it has a granular structure, although extrapolating this to F-keratins would require new data. Whether or not this is the case in synapsids has not been thoroughly investigated.

Wang (2016) offers a good review of keratinous material in general, and describes the fibre-matrix texture as tightly packed and well bonded. However, this is not always true because the dark texture in the CT scan presented by *Laurent et al.* (2014) shows there are voids, and that there are more voids in the middle layer of a swan (*C. olor*) feather than the inner or outer layers. Unfortunately the paper by *Laurent et al.* (2014) is presently the only published evidence of interstitial spaces in the cortex and

[22]Roving (n., chandlery): A twisted roll of fibres, used to make rope.

[23]Cytosol (n. biology): the aqueous component of the cytoplasm of a cell, within which various organelles and particles are suspended

these interstitial spaces are not the main topic of that paper.

At this point in the chapter, the (macroscopic) structural and (microscopic) material perspectives meet, where it is known that the fibres form layers and that the layers are made from keratin. However, it is not known how these layers vary along or around the feather, between different primary feathers, or between genetic or ecological taxa.

2.3 Mechanics

Published values of Young's modulus of *feather keratin* vary between 0.045 (*Macleod*, 1980) and 10 GPa (*Purslow and Vincent*, 1978), which seems an unlikely range. These values are not comparable for a number of reasons. *Macleod* (1980) tested material from pelvic contour feathers of fowl birds and these feathers would not have been subject to the same selection pressures as primary flight feathers. *Purslow and Vincent* (1978) used flight feathers from the pigeon, which *have* been subjected to those pressures. *Macleod* (1980) tested a cross sectional piece but *Purslow and Vincent* (1978) test a whole feather. Their tests cannot be compared because they do not test the same level of the structural hierarchy. This would be analogous to comparing the properties of a brick, which is easy to break with a ball hammer to the sturdy wall that was made from those bricks and can only be broken with a sledge hammer, or maybe not at all.

They also used different methods. *Macleod* (1980) used a tensile test and *Purslow and Vincent* (1978) used a cantilever bending test, so they are not loading the material in the same way. Also, they made different mathematical assumptions about the material, which are implicit in the choice of test piece and technique (and which would have been valid in the narrow scope of each paper). However, for these reasons the results obtained cannot be compared. Also, stiffnesses were obtained which must not be considered as the Young's modulus. Because most of the current literature differs in technique, subject and sample (and therefore,

assumptions) it is not easy to build a larger picture of general shaft mechanics (*Bachmann et al.*, 2012, *Lees et al.*, 2017). A summary of these factors for relevant papers since *Purslow and Vincent* (1978) is presented in Table 2.1.

Study	Stiffness (GPa)	Species	Feather	Test Piece	Technique
Wang and Meyers (2017)	3(t) - 7(n)	Seagull	unknown primaries	dorsal, ventral, lateral pieces at three longitudinal positions	tension, compression, nanoindentation
Lees et al. (2017)	2 - 6	4 spp.	all primaries	calamus	3 point bending
Liu et al. (2015)	4	Peacock	unknown tail	calamus, middle rachis	tension, compression
Laurent et al. (2014)	5 - 10	Swan, Bald Eagle, Partridge	P3	multiple layers	nano-indentation
Bachmann et al. (2012)	6	Owl, Pigeon	P6	inner layer	nano-indentation
De La Hera et al. (2010)	BS	Black Cap	P10, T2	whole	cantilever bending
Weber et al. (2005)	BS	Chiffchaff, Warbler	P1	whole	cantilever bending
Borgudd (2003)	BS	Chiffchaff, Warbler	unknown primary	whole	cantilever bending
Cameron et al. (2003)	2 - 5	Swan, Goose, Ostrich	unknown primaries	unknown longitudinal strip	tension
Dawson et al. (2000)	2.5	Starling	P3	unknown longitudinal strip	tension
Corning and Biewener (1998)	BS	Pigeon	unknown primaries	whole	4 point bending
Worcester (1996)	BS	13 spp.	P1, P4, P7	whole	cantilever bending
Bonser and Purslow (1995)	2.5	8 spp.	P1, P2, P3	25 mm piece from dorsal surface at unknown length	tension
Macleod (1980)	0.045	Turkey	pelvic contour feather	whole, and pieces	cantilever bending, tension
Purslow and Vincent (1978)	10	Pigeon	outermost P3 / 4	whole, and pieces	cantilever bending, 3 point bending

Table 2.1: *A summary of studies on the mechanical response of feathers since the work of* Purslow and Vincent *(1978), who were among the first to investigate their stiffness. The results of these studies are not comparable because there are a number of differences. Modulus values are approximations,* not *Young's modulus, and* BS *denotes that a bending stiffness was reported, which includes the second moment of area: $BS = EI$, where E is modulus and I is the second moment of area. Out of plane couplings are also included in a bending stiffness.*

Structural Studies

The differences between various structural testing methods are introduced here in the context of the literature on feathers, but are comprehensively explained in undergraduate textbooks such as *Gere* (2008).

Cantilever testing

Cantilever bending fixes a beam at one end and measures deflection under loading, as shown by Figure 2.9, where a beam of length L and stiffness E, is fixed at one end and loaded at distance h from the fixed end. Deflection at the point of loading δz is given by the following static beam equation from Euler-Bernoulli beam theory and which was used in modified form by *Purslow and Vincent* (1978)[24]:

$$\frac{d^3\delta_z}{dz^3} = \frac{F_z}{E_z I_z} \tag{2.1}$$

where the beam is straight, composed of a linearly elastic material and the angle of rotation (of the radius of the deflection's curvature) is small (*Gere*, 2008). In this equation F_z is the force at point z, E_z is Young's modulus and I_z is the second moment of area (see Figure 2.9). Unless the material is isotropic or at least transversely isotropic and loaded normally, there will be unconsidered anisotropies within it and out of plane stresses. It might seem an appropriate choice for holistic approaches because the shaft of a flight feather is a natural cantilever (*Bachmann et al.*, 2012, *Bonser and Purslow*, 1995, *Purslow and Vincent*, 1978, *Wang*, 2016, *Wang and Meyers*, 2017, *Wang et al.*, 2015); the bones of the manus[25] and the tendons of the postpatagium[26] support the shaft which

[24] There is an implicit assumption here that $dEI/dz = 0$. This assumption will be discussed in more detail in Chapter 7.

[25] manus (n., anatomy): the terminal segment of a forelimb, corresponding to the hand and wrist in humans.

[26] postpatagium (n, anatomy): the triangular piece of soft tissue which connects the hand to the body, as in a bat's wing.

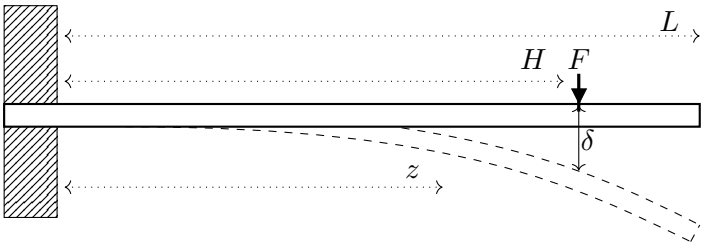

Figure 2.9: *A schematic diagram, which illustrates cantilever bending under static load, in a beam of length L, fixed at one end and loaded at some distance h from the fixed end by force F. The deflection at the point of loading, δ can be computed at any distance z along the beam. In this loading regime, the beam can be divided into a dorsal part which resists a tensile load and a ventral part which resists a compressive load. If the material is isotropic, these two parts are separated by an imaginary central line called the neutral axis, where there is no force. In anisotropic materials, this line might not be in the centre.*

is a beam. *Purslow and Vincent* (1978) compare the model with empirical observations. The model predicts bending well. However, it makes a number of assumptions which must be considered if other properties are to be extracted. A feather is not straight but always has a degree of longitudinal curvature, which will introduce a torsional load as well as simple bending. A feather also resists a non-uniform load in application, because the load is proportional to the vane width and angle of attack at an infinitely small cross section. This can be experienced when one sticks their hand out of the window of a moving car. The point load used in this method does not introduce a torsional load. These two considerations (bending and distributed load) are acknowledged by most workers but have not yet been added to models because the effect is quite small and models fit well.

3- and 4-point bending tests

Three and four-point bending tests are alternative methods which improve on cantilever bending in that they use a distributed load. In looking at elastic response, either technique would be suitable. Any of these bending tests would be appropriate techniques to test whole feathers or at least whole cross sections but not lower level structures because this is not how they are loaded in application and to test them in bending would introduce shear forces not present in application.

Finally, *all* bending tests do not determine a modulus (E) explicitly. They determine bending stiffness EI. Therefore, to report E requires a knowledge of I, and it has been shown in Figure 2.2 that this is highly variable (*Bachmann et al.*, 2012). Some studies simply report EI and do not obtain values of E and I separately. Others have attempted to overcome this limitation by measuring I at discrete intervals, or by modelling the rachis as a tube, square prism or tapering cone. Published results by *Bachmann et al.* (2012) and unpublished results by *Laurent et al.* (2014), *King* (2016) and *Palmer*(ongoing) have shown that these approaches are probably oversimplified. They observe I at discrete intervals and interpolating values in between might be a better approach until I can be properly modelled in terms of z.

The paper by *Lees et al.* (2017) presents models that confirm something more is afoot because simple anatomical measurements do not explain mechanical performance in feathers. This agrees with findings by *Laurent et al.* (2014) and *Lingham-Soliar* (2017), though Bachmann postulates that geometry explains a larger proportion of feather flexion than material properties and presents data which shows that more advanced measurements (I, the second moment of area, rather than d the diameter of the rachis) do have some fairly well fitted predictive power.

Additionally, if samples are laminated then I can be computed such that the distribution of load bearing and non-load bearing components with respect to the bending axis are considered, because falsely increasing the load bearing second moment could in-

troduce large errors in I. For example, the I of a circular section varies with the fourth power of the diameter, so assuming an outer layer is load bearing will have a very large effect indeed.

Suppose E has been extracted with an approximation of I, E still *cannot* be called the Young's modulus, because it is an approximation of a stiffness tensor (as all results of a constrained mechanical test are). The stiffness can only be thought of as Young's modulus in the special case of unconstrained uniaxial stress, when elements of the stiffness tensor can be filled by a single independent elastic constant which relates to a single material constant, Young's modulus. It will be an approximation of stiffness for *that* sample, in *that* stress state for *that* observer and will be an extrinsic property that should not really be extrapolated to different samples, or even the same structure under different loads, because it does not consider shear forces, moments or their couplings to out-of-plane strains. *The elastic modulus of a material is not the same as the stiffness of a component made from that material.*

Material Methods

Tension test

The methods described above obtain a reduced stiffness modulus with a reduced number of unique elements for either the whole feather or a piece of a whole cross section. A tension test can investigate the next level of hierarchy - either a cortical piece, or a cortical layer–by stretching a sample in an extensible frame and measuring load and displacement. A tension test could be applied to a whole feather (*Macleod*, 1980), but this is not how a whole feather is loaded in application. It is more appropriate, and geometrical differences are more easily accounted for, if the test is conducted on a piece of cortex excised from the dorsal or ventral wall which has had the medullary substantia carefully removed.

Loading an excised piece of cortex mimics how that piece is loaded in application and results between different studies would be more comparable because a test piece is normally a standard

shape and it is small enough that there is less structural variation within the piece. A tension test is simpler and probably the most fundamental mechanical test, as it is easy to constrain stresses.

Subtle differences in methodology such as the strain rate, or the clamping method should not impact the stress–strain relationship so long as the clamps do not slip and the strain rate is high enough that viscoelastic[27] effects do not introduce creep[28]. Loads between different sized test pieces are also not so important because feathers have a large safety factor (*Wang et al.*, 2012) so it should be simple to record adequate data in the elastic region[29]. One small consideration might be the transverse curvature of the test piece, because although only a small piece of cortex is loaded in tension, when it is a part of a tube, the distance from the neutral axis for any given longitudinal sub-sample will vary and therefore some anisotropy within the test piece might be expected. Because of this, the cortical sample should be as small as possible such that it can still be excised without introducing stress concentration points (*i.e.* by leaving a notch) and test pieces should be proportionally measured rather than absolutely measured so that they are comparable between birds. Comparing tests from a 50 mm gauge length (an absolute measurement) between species would be unfair, a 50 mm-long sample is the whole shaft of a small bird's feather, but only a small part of a large birds feather. A relative gauge length would probably compare a percentage length of the rachis. For example, *Bonser and Purslow* (1995) used an absolutely measured gauge length but specify that only the *dorsal* surface is tested, which means that the width of the sample is proportional. If the width of the test piece was absolute, a piece which might be 3 mm

[27] Viscoelastic materials exhibit time-dependent strain; that is the material properties vary depending on the rate that load is applied

[28] When a stress:strain curve does not begin and end at the origin, it is either because of plastic deformation, or because of viscoelastic effects. The latter is called creep.

[29] Safety factor is the difference between the force needed to buckle the feather and the force needed to sustain flight, *i.e.* buckling failure force / lift force equal to body weight.

wide would consider only the dorsal section of the quadrilateral prism in a swan, but would include parts of the lateral wall in smaller birds, which have adapted to a different loading regime. This would introduce a source of error.

Nanoindentation

An indentation test can consider a larger structure by using a map of indents, but each indentation really only considers a small interaction volume which is a half sphere proportional to its depth (*Oliver and Pharr*, 1992). By using this technique it is possible to consider the modulus of a single layer, although the modulus reported will also vary and will not be comparable unless the approach vector is known and relatable to the fibre orientation because the modulus will vary accordingly in a fibrous composite. An angle-modulus relationship has not yet been established for feather keratin, mostly because the angle of specific layers of fibres in the interaction volume has not been confirmed to a sufficient degree of precision and so indenting a cross-section or longitudinal section, even for similar samples would load the fibres differently due to varying orientation. However, it might be reasonable to compare indents normal to fibre direction. The protein structure would suggest that layers can only rotate through one plane (in polar space). *Laurent et al.* (2014) and *Wang and Meyers* (2017) both present longitudinal indentation results and transverse indentation results, which might be comparable but cross sectional indentations should not be compared because ply angle variation has a larger influence. Figure 2.10 shows that in a transverse or longitudinal sample, an indentation *should* be perpendicular to fibres whatever the angle but in a cross sectional indentation this is not the case.

Another important consideration in the comparability of indentation results is the probe shape used and the depth of the indentation. All nanoindentation studies so far (*Bachmann et al.*, 2012,

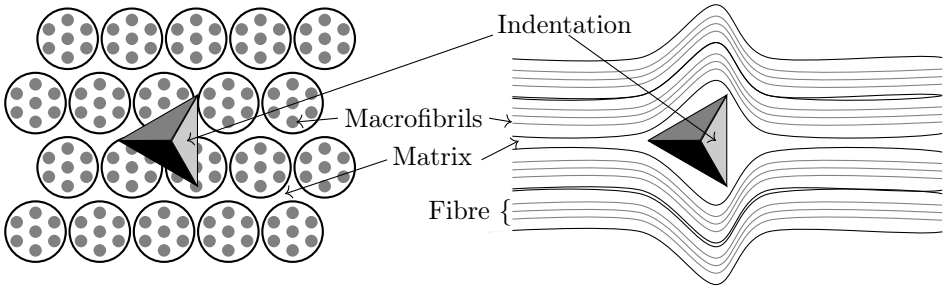

Figure 2.10: *A schematic diagram, which illustrates how the angle of approach in a nanoindentation test might be affected by fibre orientation. This shows how fibrous material deforms around a point-load. If the nanoindentation probe approaches a cross sectional face, the ply angle will have a large effect on the resultant modulus but if the indenter can approach from an angle perpendicular to the fibres then the ply angle will not have a large effect on the resultant modulus. Reproduced from* Wang and Meyers *(2017).*

Laurent et al., 2014, *Wang and Meyers*, 2017) used a Berkovich[30] diamond tip, but also indent to different depths, and so test a different interaction volume. This is relevant because the volume tests will have a selection error based on the size of the lower structural level *i.e.* the relative volume of matrix and fibres in the sample volume, although this can be accounted for by taking averages of multiple indentations in similar places. There are also small effects caused by the size of the indentation (*Huang et al.*, 2006) and also the shape of the probe (*Calabri et al.*, 2007) but they need not be considered in larger indentations (depth $>$ 500 nm). The most comparable results will test as large an interaction volume as possible (and be a proportional measurement) without moving into a different layer.

Moduli from tension tests and nanoindentation are much more relevant in considering the material properties of the cortex and the influence of layers, although to date no studies have applied

[30] A three sided pyramid of particular dimensions named after the Russian materials scientist *Berkovich* (1950)

Classical Laminate Theory, CLT, to properly account for the presence and variation of layers in the cortex. As it stands, the tensile modulus of either a single layer, or a laminate remains unquantified. However it is established that the modulus varies between hierarchical levels, between different birds and also according to humidity where increased humidity decreases stiffness (*Bertram and Gosline*, 1987, *Taylor et al.*, 2004). The tensile modulus also varies with sulphur content where increased sulphur content increases stiffness (*Akhtar and Edwards*, 1997, *Fraser et al.*, 1973a, 1988, *Naito and Arai*, 1996, *Wang*, 2016). However, there is a gap in the literature, which when filled will provide the modulus value of a single layer, information on how variation in layup affects the properties of the laminate, and a comparison of feathers from multiple birds. Another constant, Poisson's ratio ν, also becomes relevant here, because it to can be cited for the laminate and for the lamina. In this case the constant relates transverse contraction to axial elongation and it is also an intrinsic material constant, which is reported a few times in the literature, using different approaches on different keratinous materials, and without a consensus value (*Zhang et al.*, 2013). The issues of Poisson's ratio ν in keratinous material and more generally in biological materials is the topic of a section in *Vincent* (2012), who reports values ranging between 0.35 and 0.9. *Soons et al.* (2012) take ν to be 0.4 in their modelling work, on the basis of some agreement of values from work on bovine hoof (*Franck et al.*, 2006, *Li et al.*, 2010). It might be possible that an analytical perspective of mechanical test results could extract the value despite it being difficult to measure directly.

Summary

Feathers are hierarchically complex structures and component dimensions range from the nano-scale to the macro-scale. This complexity has made it very difficult to constrain mechanical tests such that material constants can be extracted, and stiffnesses re-

ported in the literature are largely incomparable. On this basis it is now appropriate to go one level deeper, to approach the feather shaft as a laminate. In looking at local mechanical properties and microstructure, this work will investigate fibre orientation (Questions 1,2) and one more important consideration: how the material varies (Question 3).

Chapter 3

Methods

Tools & techniques.

At this point the questions posed at the beginning of this thesis must become objectives. To answer the first question:

> 1. What is the layer geometry of the primary flight feather shaft, and does it change within the shaft?

It will be necessary to image and quantify layup geometry in multiple places of replicate primary flight feathers.

To properly consider the second question:

> 2. Are there differences in the material composition of those layers?

Material (protein) composition must be investigated as it occurs within in its natural state.

and to address the last question:

> 3. Are the layers mechanically relevant and is the isotropic assumption inappropriate?

Pieces of feather shaft must be mechanically tested and the results analysed from an approach based in Classical Laminate Theory, which considers both layup geometry and material.

This chapter contains three sections which present methods used to accomplish these objectives. Each section details the collection and processing of experimental data and, where appropriate, example data is presented but not interpreted. Results will be fully presented, analysed and discussed in later chapters, though certainly with regard for objectives 1 and 2, the methods presented here are a contribution themselves.

3.1 Layup Imaging

The most appropriate method to image and quantify layup geometry in a large number of primary feathers, should be able to:

1. image fibre orientation
2. sample each layer, or the entire cortical width of the shaft and
3. image a large number of samples in a given period.

A number of methods have already been used to gather information on the laminar geometry of the feather shaft, which appear in the literature and have been considered in Chapter 2. Some of these methods have been evaluated according to the above criteria in a recent paper (*Laurent et al.*, 2019). The paper tests a number of techniques against the attributes identified above and concludes that Synchrotron Radiation Computed Tomography, SRCT, is the most appropriate method in terms of those criteria. A summary of the techniques applied in that paper and in the literature are presented in Table 3.1.

SRCT uses X radiation from a synchrotron light source to produce three-dimensional, density contrasted images called tomograms, by compiling a series of planar X-ray images, called radiograms. The technique, when applied to feathers, can be used to infer fibre orientation by imaging pseudo-ellipsoid holes in the cortex, which align with fibre direction. This relationship between hole orientation and fibre direction was confirmed with correlative

Serial Block-Face Scanning Electron Microscopy (SBF-SEM) in a feather from the swan, see Figure 3.1. The holes measured approximately 6 µm in the major axis by 2 µm in the minor axis *Laurent et al.* (2019).

Technique	2D/3D	Resolution	Volume*	Destructive?	Fibres visible?	Throughput	Preparation
Light Microscopy							
Wide-field Light Microscopy	2D	200 nm	-	Yes	No	Fast	Significant
Polarised Light Microscopy	2D	200 nm	-	Yes	No	Fast	Significant
Confocal Laser Scanning Microscopy (CLSM)	3D	200 nm	0. 1 mm3	Yes	No	Fast	Minimal
Multi-Photon Laser Fluorescence Microscopy	3D	200 nm	0. 1 mm3	Yes	No	Fast	Significant
Scanning confocal PolScope	2D	200 nm	-	Yes	Yes	Fast	Minimal
Electron Microscopy							
Scanning Electron Microscopy (SEM)	2D	3 nm	-	Yes	Yes	Slow	Extreme
Transmission Electron Microscopy (TEM)	2D	$<$ 1 nm	-	Yes	Yes	Slow	Extensive
Serial block-face SEM	3D	$<$10 nm	0. 001 mm3	Yes	Yes	Very slow	Extensive
X Ray Techniques							
Micro-computed CT	3D	$<$ 1 µm	0. 1 mm3	Yes	Proxy	Very slow	Minimal
SRCT	3D	300 nm	0. 1 mm3	Yes	Proxy	Fast	Minimal
Scanning Probe Microscopy							
Nano-indentation	2D	15 µm		Yes	No	Very slow	Significant

Table 3.1: *A table of imaging techniques for observing fibre orientation in the rachis. Modified from (*Goggin et al.*, 2016,* Kherlopian et al.*, 2008). *Without tiling.*

3.1.1 Data acquisition: Synchrotron Radiation Computed Tomography

Samples of feather rachis were scanned during three trips to two different synchrotron light sources. These were the TOMCAT beamline at the Swiss Light Source (SLS) (Villigen, Switzerland) and the I13-2 beamline at the Diamond Light Source (Didcot, UK).

Different sample preparations and scan settings were trialled on a bench-top machine at the University of Southampton and with the help of beamline scientists at both synchrotrons (*Laurent et al.*, 2019). Two methods of sample preparation were used in this work. In the first method, four matchstick sections approximately 500µm× 500µm× 1cm were excised from the shaft and mounted directly onto an SEM stub with paraffin wax. In the second method, four region-of-interest scans were acquired from a whole cross-section, which would correspond to matchstick counterparts from the first method. Samples prepared using the first method were scanned at the SLS. They were placed 7 mm from the source in a 0.8 mm field-of-view and irradiated through 180°, with a 21 keV monochromatic beam (filtered through 100 µm Al and 10 µm Fe) to absorb low energy photons. A PCO Edge 5.5 CMOS detector (Kelheim, Germany) with a 100 µm LuAg:Ce scintillator and a 20× objective was used to capture 1501 projections each at 200ms integration time. This resulted in a total scan time around six minutes and a voxel size of 325 nm. Tomograms were reconstructed with the GridRec algorithm (*Dowd et al.*, 1999, *Marone and Stampanoni*, 2012).

Samples prepared according to the second method were scanned using a similar protocol at the SLS and at the Diamond Light Source I13-2 beamline with a 14 keV monochromatic beam. 4000 projections at 200 ms integration time, using a PCO 4000 (Kelheim, Germany) camera coupled to a Lu:Ag Scintillator and a 10× objective with another 2× in the optics system (20× effective magnification). This setup also resulted in 325 nm voxel resolution, but with a longer scan time, approximately 20 minutes. Tomograms were reconstructed with the Tomo-Recon algorithm (*Atwood et al.*,

2015).

Some supplementary optical micrographs were collected at a later date, using a very simple optical microscopy setup with a 20× objective and a digital camera.

3.1.2 Data processing: extracting layup information

Constructed tomograms were filtered using a $4 \times 4 \times 4$ pixel Gaussian kernel to remove noise and enhance the contrast between hole space and feather material. Tomogram data was then thresholded and binarised such that the holes had a value of 1 and all other voxels had a value of 0. Threshold values were selected manually, because the samples presented quite different histograms due to variation in thickness and number of holes. An automated method would have been more appropriate if all of the samples were the same size and had similar hole concentration but these differences seemed to make scripted use of thresholding algorithms *e.g. Otsu* (1979) *etc.* unreliable. However, the Otsu algorithm which is mostly used for background subtraction works well in cases where there is no medullary foam, and there are correspondingly only two phases—air and keratin. Though this is still true in cases where there is medullary foam, the histogram is multimodal and as the algorithm tries to threshold the picture into two phases of least variance (background and foreground), it does not return a threshold between air and keratin with an acceptable rate of success for these purposes.

Binarised scans were then evaluated using the BoneJ plugin (*Doube et al.*, 2010) for the Fiji platform, using the IRIDIS 5 computing cluster at the University of Southampton. A binarised tomogram can be seen in Figure 3.3.

The plugin was configured to consider holes between 24 and 3000 voxels (7.8 and 975 μm^3, respectively) so as not to include noise, phase artefacts, or cells of the medullary pith. Figure 3.4 shows an inner and an outer layer of segmented voids. The holes are longer than they are wide and ellipsoids can be fitted to each one. BoneJ calculates the Cartesian centroid location as well as moments of inertia for each hole. Figure 3.5 shows a small subsample from the CT scan with these data illustrated.

It is then necessary to transform the data, in the first instance to straighten the data in case the samples were not perfectly normal to the CT beam, and in the second to account for the curvature of

the feather's shaft. The first step uses a transformation matrix to tilt the scan data. The transformation matrix is calculated from point coordinates of the outer edge of the cortex from the top and bottom tomograms of the tomogram stack. The second transform fits three circles on the middle tomogram to convert the data from Cartesian space into polar space. These circles are shown in Figure 3.6; one circle is fitted to the outer cortical edge and a second to the inner cortical edge. The colours used in this figure, *i.e.* blue for the inner layer and orange for the outer layer are kept through successive chapters. The third circle, which has a centroid location and radius length which are averages of those from the first two circles, is equidistant from them both. This circle is used to 'unroll' the cylindrical feather into a flattened sheet. This encompasses a mapping from Cartesian space into polar space based on this circle and then transforming data which describes the holes in the feather as well. This transformation uses the slope of the third circle to transform the vector orientation of the major axis of the fitted ellipsoid, which was calculated from the moments of inertia obtained from the BoneJ package. Using this middle circle as the axis line accounts for samples which have diverging or converging cross sections.

After the second transformation, the cylindrical prism has been unrolled and the rachis can now be considered as a flat piece of material with parallel layers. To measure the layer thickness and orientation, the data can be binned, dividing the material into a large number of virtual layers ($\approx$30). Frequency data on hole orientation (the vector of the major axis) can be calculated for each virtual layer, and a two-dimensional histogram can be formed when all of these histograms are combined. Figure 3.7 shows that the frequency of holes oriented in 6° bins changes through 30 virtual layers of the flattened rachis. In each virtual layer, the angle bin with the highest count can be plotted and the position of the layer boundary can be calculated by using the slope of that line, which is the greatest between a point in the inner layer where the most populated bin has a value of approximately zero and the

next value which is in the outer layer and has a value of approximately 90. Once the boundary location has been calculated, the virtual slices can be treated as inner layer or outer layer and new one-dimensional histograms can be made which consider these two real layers rather than 30 virtual layers.

Figure 3.8 shows orientation-frequency data for each layer. We can use a double Gaussian because the dominant direction will be normally distributed about the mean but there will also be a noise component introduced because small holes are less precisely discretised and less precisely fitted. This is likely also normally distributed but with a different distribution than the main hole alignments. The distribution of hole orientation should have a similar mean and a smaller standard deviation. Both the mean and the standard deviation are more precise once the noise has been subtracted, and the standard deviation shrinks from approximately 45° to approximately 30°. A Gaussian distribution is used to remove extraneous signal because it is versatile: Where noise is random, the Gaussian fits a straight line; where noise is caused by small aspect ratios or imprecise and imperfect discretisation of of holes, the Gaussian can be fitted with a different mean. This is also needed for some feather samples which have very square shapes and the cortex cannot be fitted as well by the circles. This leads to a skewed histogram, despite the main peak being very similar. Most often, a straight line is fitted, or two Gaussians are fitted with very similar means. By fitting two Gaussians, all possibilities are covered and changing *a priori* knowledge about each scan does not need to be input manually.

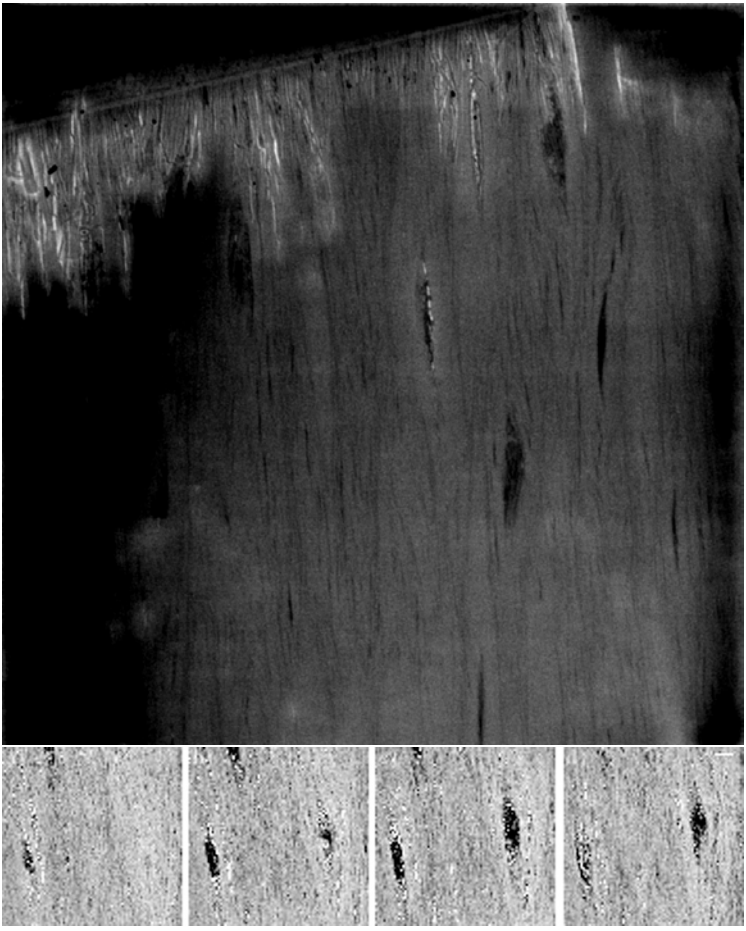

Image series

Figure 3.1: *This figure shows image series taken using a Serial-Block-Face Scanning Electron Microscope (SBF-SEM). These images are 350 nm apart and show multiple slices through the same 3 holes. These voids have a major radius of approximately 6 µm and a minor radius of 2 µm. These holes can be used to infer fibre orientation.* ***Scale bar*** *5 µm.*

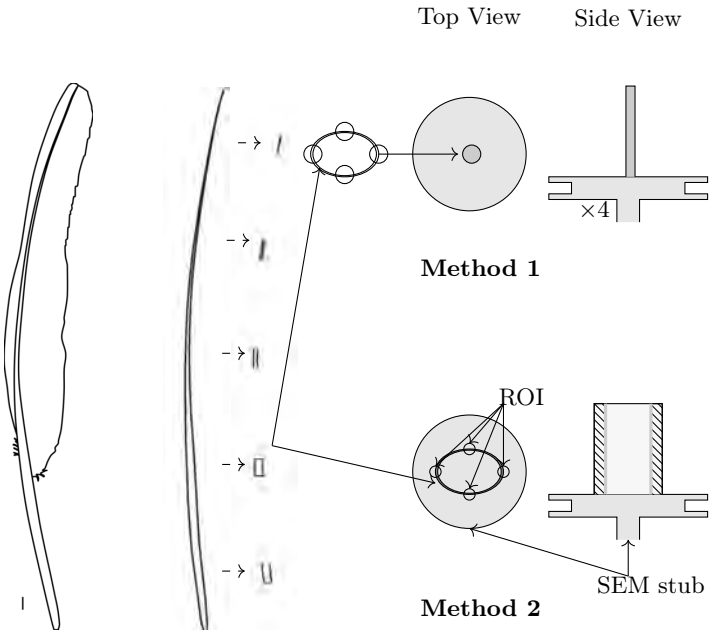

Figure 3.2: *A schematic diagram to show two different methods of sample preparation for Synchrotron Radiation Computed Tomography (SRCT) scanning. Method 1 involves excising smaller pieces of feather and supporting them in paraffin wax. Method 2 involves using region-of-interest scanning on larger, more stable samples.*

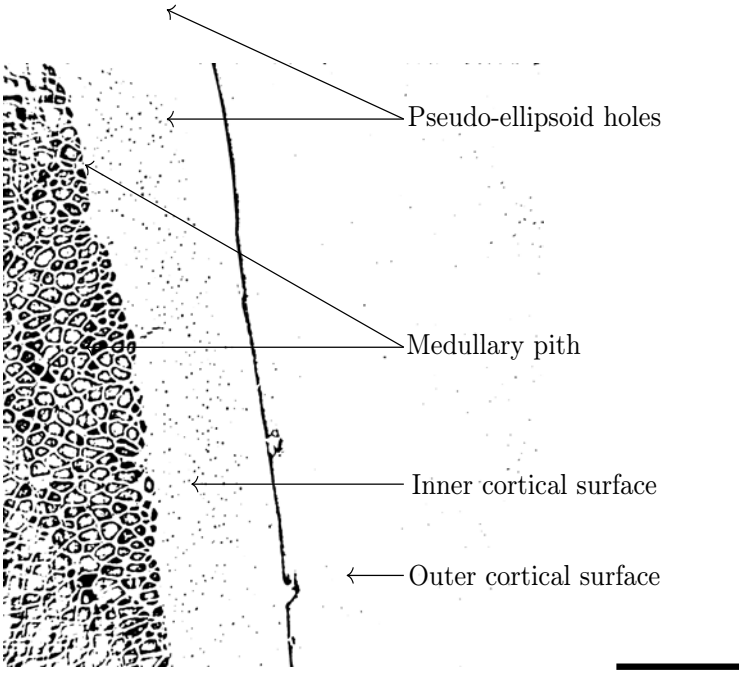

Figure 3.3: *A tomogram of a cross section of a swan's first primary (P1) at 30% length. The tomogram has been filtered with a 4 × 4 × 4 pixel Gaussian kernel, then thresholded and binarised ready for the BoneJ 'analyse' macro (*Doube et al.*, 2010) Here the voids (pseudo-ellipsoid holes)have been segmented (black). Circular voids can be interpreted as longitudinal voids which are oriented transversely to the page, and elliptical voids can be interpreted as voids whose long axis is parallel with the long axis of the feather.* ***Scale bar*** *0.2 mm*

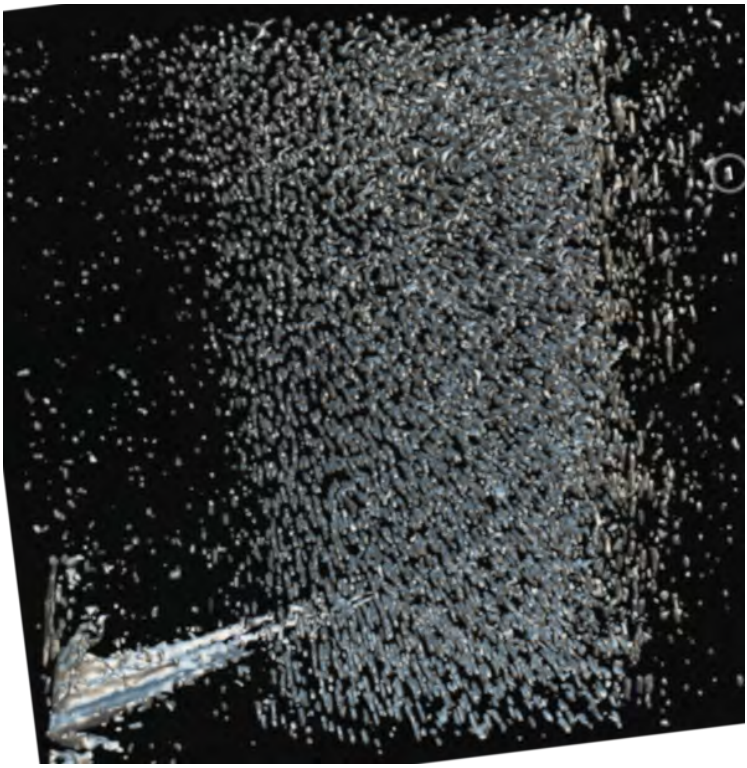

Figure 3.4: *A figure which shows / plays a video of a small 3d slice of the cortical holes, after the volume has been thresholded, and the holes have been segmented. Two layers are visible and also how the number of holes decreases towards the inner edge (on the left). The video later zooms in on the holes to show their elliptical shape.*

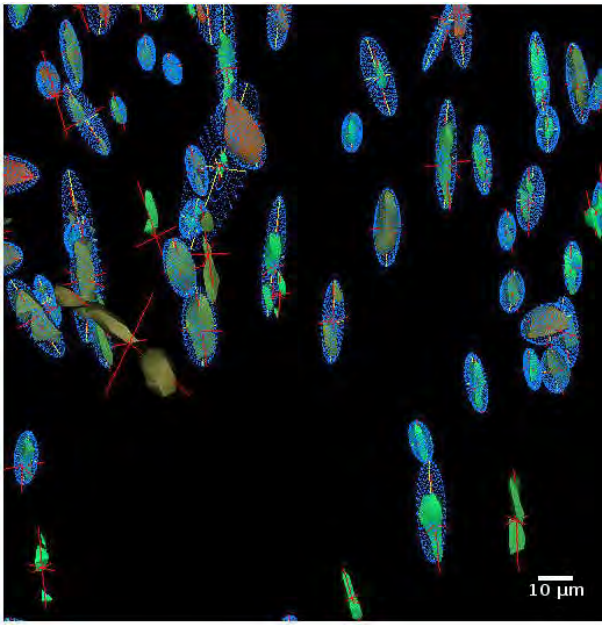

Figure 3.5: *A figure which shows how voids in the rachis cortex can be segmented, and ellipsoids can be fitted to binarised data.*
***Scale bar** 10 µm*

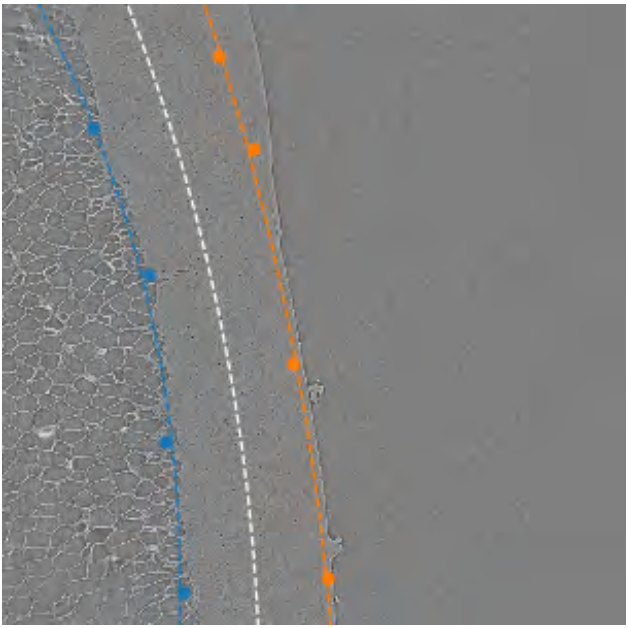

Figure 3.6: *A diagram to show how fitted circles are used to transform a Cartesian space into a polar space and also account for diverging/converging boundaries in a non-standard shape. Points along the inner and outer edges of the scanned feather shaft are captured from mouse-click events. For each edge, a circle is fitted which is shown by corresponding dashed lines. Another circle, which has a centroid between the centroids of the two fitted circles and a radius which is the average of the radii from the these circles is displayed as a white dashed line. Distance (i.e. cortical width) will be measured (and offset) from this line, to account for samples where cortical width is diverging or converging. The slope of this line will also be used to transform the data from Cartesian space into polar space. The material outside of the orange line is cyanoacrylate glue used to mount the sample to a holder.*

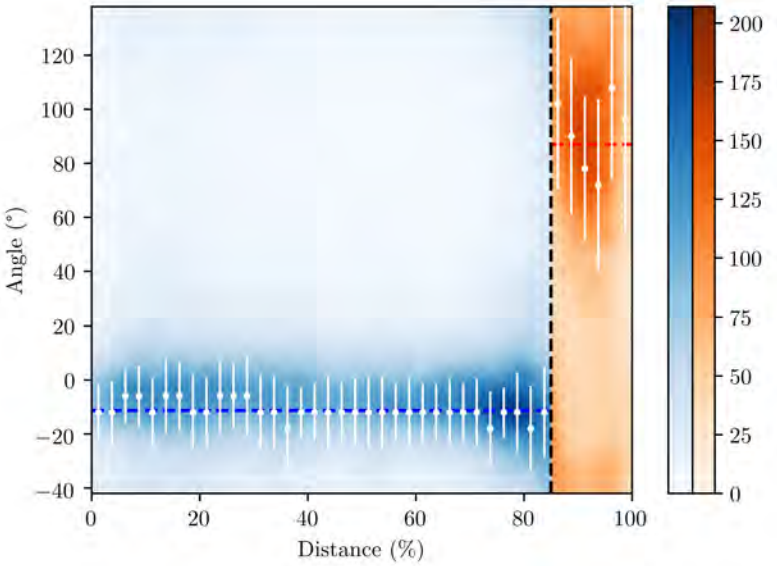

Figure 3.7: *A two-dimensional histogram showing information on the orientation of cortical holes in the feather shaft. The histogram presents frequency counts of holes constrained to a bin which contains six degrees of major axis orientation and 3% of the cortical width, in polar space. The data has been bi-cubicly interpolated to smooth the data and in this example, the inner and outer layers of the feather shaft use orange and blue colour maps, respectively. White markers indicate the rotation bin with the highest count in each distance bin, and bars are the standard deviation within that distance bin. The black dashed line indicates the layer boundary, and is determined by the derivative of a set containing the values of these white markers. Blue and orange dashed lines indicate the fibre direction for each layer, which is the mean value of the second fitted Gaussian distribution, when the first accounts for noise caused by imprecise thresholding and/or imperfect scan parameters. The standard deviation is very close to the average values of the white markers in each layer. This plot indicates that there are two layers, the first one is 84% of the cortical width and is oriented at minus 10°. The second layer accounts for the remaining 16% of the cortical width and is oriented at 84°, though there is larger variance about this value.*

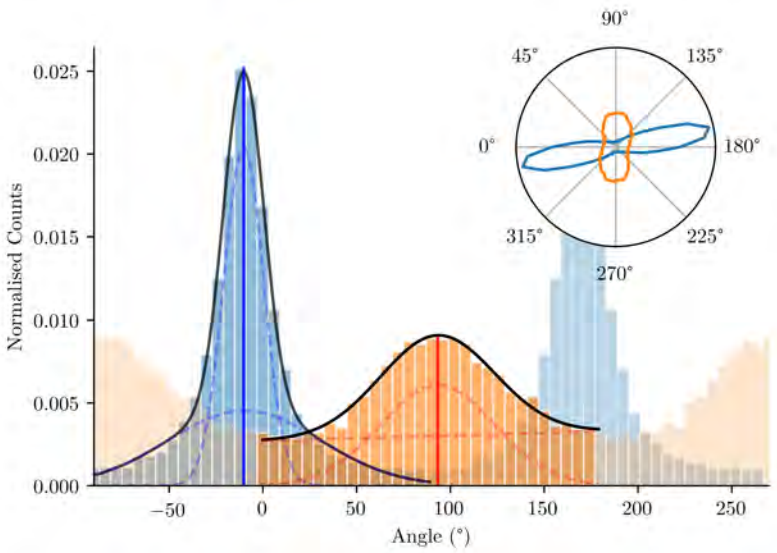

Figure 3.8: *This figure presents the distribution of holes in each layer of the rachis sample, with rotation bins of five degrees. The inner and outer layers use blue and orange colour schemes respectively. For each layer, the data is fitted with a double Gaussian distribution, shown by dashed lines. Blue and orange solid lines indicate the mean value of the second Gaussian, which is the in-plane fibre orientation of the layer in polar space. The first Gaussian accounts for noise caused by imprecise thresholding and imperfect scan settings. The black line is the sum of these two Gaussians and is shown to demonstrate adequate fitting. Because the data is cyclical, repeated data is shown but rendered transparently. The same data is presented as a compass plot in the top right corner, using corresponding colours to show this more clearly.*

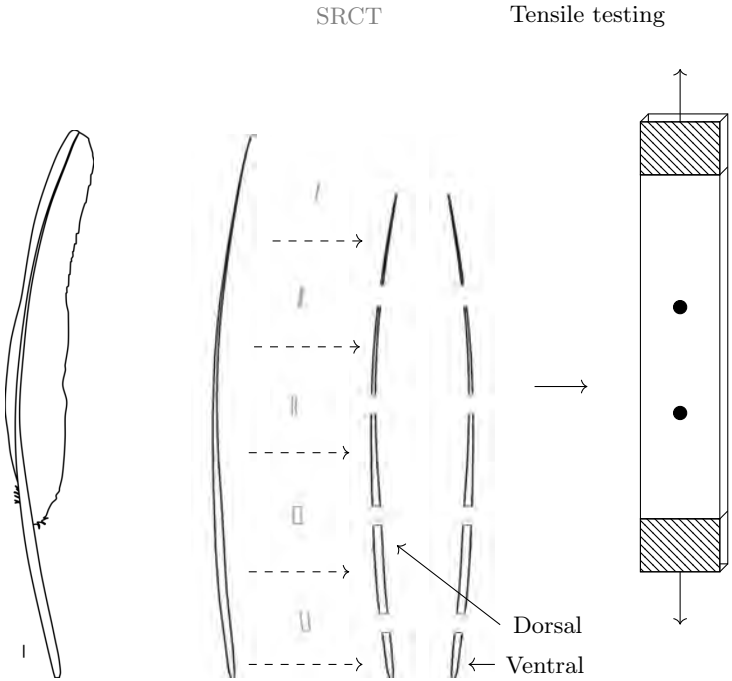

Figure 3.9: *A schematic diagram showing which parts of the rachis are used for tensile testing. The vane is removed from the shaft, which is cut into pieces. Small pieces were taken for CT scanning, and larger pieces were reserved for tensile testing. Dots are applied to these pieces and the pattern is used to measure strain using a video-extensometry setup.*

3.2 Tensile testing

Tensile pieces were excised from the shaft of the first, third and fifth primary feathers (P1, P3 and P5) from the right-hand wing of three swans, *Cygnus spp.*, with a Proxxon Minimot 40/E hand-held rotary saw (Föhren, Germany), and a point tracking pattern was applied to each tensile piece with a fine marker pen. Samples were mounted in an Instron™ ElectroPuls E1000 (Norwood, MA, USA) electric test instrument, equipped with a Dynacell ±2kN dynamic

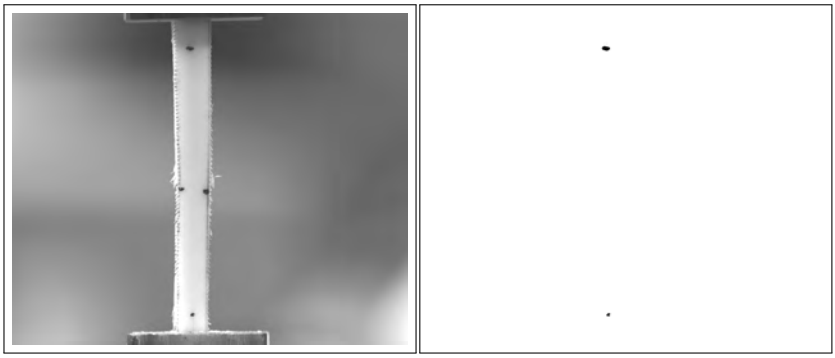

(a) *Raw video frame* **(b)** *Thresholded*

Figure 3.10: *A figure to show the points used to gauge strain, using digital image correlation. The wedge-action grips of the tension test machine can be seen at the top and bottom of subfigure* ***(a)****.*

load cell, gripped by mechanical wedge action grips with serrated jaw faces. Samples were then loaded in tension under displacement control at 25 mm/min to a 250 N load or until 5 mm extension is reached.

Extension was captured with a Manta G504-B camera from Allied Vision (Stadtroda, Germany) with a 2452 × 2056 CCD sensor with 3.45 µm pitch, an 8 bit gray scale, a 50 mm Nikon lens and a frame rate of 6.7 Hz.

For each frame, extension was measured centre-to-centre between reference points using the analyse particle feature in ImageJ (*Schindelin et al.*, 2012). Strain was obtained using a simple Python routine to compare the distances extracted by ImageJ to frame time-stamps.

3.3 Spectroscopy

Infrared (IR) and Raman spectroscopy are two of the main methods used to investigate secondary protein structure (*Barth*, 2007, *Cai and Singh*, 1999, *Hahn et al.*, 2015, *Pelton and McLean*, 2000).

The vibrational signature of protein amide groups is very sensitive to polypeptide backbone conformation and, as a result, provides direct quantitative information regarding secondary structure. Differences in amide group geometric orientation and environment for α-helix, β-sheet, β-turn, and random coil structures in proteins lead to differences in amide vibrational frequencies and hence distinctly different amide absorptions. Raman spectroscopy makes use of scattered radiation rather than absorbed radiation (*Raman*, 1953, *Tuma*, 2005) and also has a number of advantages over IR spectroscopy in the investigation of protein secondary structures. First, sampling is much easier and Raman is capable of much greater spatial resolution (*Rintoul et al.*, 2000). The Raman spectrometer used in this work was fitted with a confocal microscope which allowed areas of 4 µm × 30 µm to be investigated whereas this spatial sampling was not possible with the available IR spectrometer which focuses to ≈1 mm^3.

Secondly, amide groups and other bands can be seen more clearly in vibrational Raman spectra than Infrared spectra. This permits the environment of numerous amino acid side chains to be characterised and studied, notably acidic residues (*Overman and Jr.*, 1999) and sulphur containing residues (*Rajkumar and Ramakrishnan*, 2001), including S-S units. Thirdly, Raman spectra are easily obtained from dilute samples in aqueous solution (*Dong et al.*, 1998, *Pelton and McLean*, 2000) or solid samples that contain water. This is very difficult using IR spectroscopy as the water bending vibration absorption (at ≈ 1645 cm^{-1}) obscures the main amide band (the Amide I band) in the IR spectrum. This is not a problem in Raman spectroscopy as the water bending mode has much lower intensity than in the IR spectrum. *n.b.* Feathers are naturally hydrated but usually at 10% or less by weight (*Taylor et al.*, 2004, *Wang and Meyers*, 2017).

Bird Material

To investigate differences between layers, feathers were removed from intact wings of four deceased birds (see Table 3.2). Species

were selected from across the avian phylogeny as different species require different material responses from their feathers. The feathers of a gull in soaring flight, for example, do not behave in the same way as those of a flapping swan or a hovering hummingbird. The birds used in this work encompassed a range of different flight styles and are as follows: swan, gull, mallard, and kestrel. The swan, *Cygnus olor* and the mallard, *Anas platyrhynchos*, are both Anseriformes. This is an ancient group of birds which diverged at the root of the avian family tree. However, they exist in very different flight niches. The swan is among the heaviest of birds (see Table 3.2) and requires very stiff feathers when it takes off from the surface of water because it is unable to jump. The mallard only flies short distances and it does so by rapidly beating its wings. The common gull (seagull) *Larus canus*, is a Charadriiform bird, which is another order nested at the root of the avian radiation. The gull spends a lot of time at sea, in soaring flight and with wet feathers. The common kestrel, *Falco tinnunculus*, is a raptor (bird of prey) which is more derived and spends a lot of time hovering into oncoming wind before it dives for food.

In order to investigate Raman spectra recorded at different lengths along a rachis, similar sections were taken from nine primary feathers from three swans.

In fact these were taken from the tensile samples already described in the previous section.

Table 3.2: *Information on different species of birds used in spectroscopic work.*

Common Name	Binomial name	Flight style	Order	Typical weight (g)
Gull	Larus canus	Soaring	Charadriiforme	430
Kestrel	Falco tinnunculus	Hovering / Soaring	Falconiforme	180
Mallard	Anas platyrhynchos	Continuous flap	Anseriforme	1000
Owl	Strix alco	Flapping, gliding	Strigiformes	470
Swan	Cygnus olor	Fast flap	Anseriforme	10,000

Sample preparation

5-mm-long sections were removed with a Proxxon Minimot 40 hand-held rotary saw (Fohren, Germany) at 40% of the rachis length from the base. Replicate sections were taken from the left and right wings.

In most cases the feathers were not cleaned because when the feather is removed from the follicle, a membrane is removed from the feather shaft which exposes clean rachis and calamus. In any case, once the samples have been embedded, the grinding process exposes clean tissue which is free of contaminants. These sections were embedded in an 8:1 mix (by weight) of Struers' EpoFix resin (Catcliffe, UK) inside a cylindrical mould (see Figure 3.11). This method is very similar to that described in an earlier nanoindentation study (*Laurent et al.*, 2014).

The swan pieces for longitudinal investigation (all from feathers of *Cygnus spp.*) were also embedded using the same process, this time in a custom mould. The block was then cut with a band-saw to bisect each piece of shaft, and then these blocks and the feathers from different species were ground using series of lapidary papers to expose the cross-section.

In some cases, a small gap formed between the feather rachis sample and the EPOfix resin. This is caused by bubbles in the resin and by the resin shrinking slightly as it cures. In the worst cases, on exposure to the laser from the Raman spectrometer, this results in burning of the sample, but also in saturation (even at low laser power) and in less serious cases, fluorescence. The solution is either to grind down the surface past the region of the gap, or to infuse the surface with less viscous resin (such as MetPrep (Coventry, England) EPO-Set resin) under vacuum. In the worst cases a new sample was required (using MetPrep resin only). Removal of bubbles from the matrix avoids the burning and fluorescence problem because the excited state responsible for the fluorescence readily loses energy to the matrix and the fluorescence is quenched.

The work on different species was planned because it was known that developing the method would take some time and probably

destroy a number of samples. This work took place when the tensile samples were needed for other experiments and spectra were taken from these samples soon after those experiments finished.

Acquisition of Raman Spectra

Spectra were taken using a Renishaw InVia Confocal Raman Microscope (Wotton-under-Edge, UK) equipped with a 100mW, line focused diode laser at 785 nm wavelength and a 50x objective. The spectrometer was calibrated using a silicon standard before each session. Eight accumulations were taken for each sample at 10mW from 3200–100 cm^{-1} with 60 seconds integration time. Spectra were taken from the Inner and Outer positions, at Dorsal, Ventral, Leading and Trailing positions, from both the Left wing and the Right wing for each bird, once the entire set-up had reached stable temperature. Spectra were baseline-corrected and fitted using a script generated from the MATLAB curve fitting toolbox. The Amide I region (1500-1800 cm^{-1}) was fitted with 6 bands, as was the Amide III region (1200–1350 cm^{-1}) and the SS region (400–600 cm^{-1}) was fitted with three bands. In all cases, following our own investigations as well as the work by *Zhang et al.* (2012), Gaussian bands were fitted with a half-width of 28.25 cm^{-1}according to the function:

$$y = y_0 + \frac{A}{w\sqrt{\frac{\pi}{2}}} exp{-2}\left(\frac{(x - x_c)}{w}\right)^2 \tag{3.1}$$

where A is the area, w is width and x_c is the x-axis intercept. A half-width of 28.2 cm^{-1}corresponds to $w = 24.0$ cm^{-1}.

The tensile samples include P1, P3, and P5 feathers for three birds, cut at 20, 40, 60 and 80% length and separated into dorsal and ventral positions. Where two layers could be clearly seen on the cross-section of each sample, the laser was positioned in the middle of the layer to be investigated, using the spectrometer's XY stage and the microscope eyepiece. Where they could not, the laser was positioned at the outside edge of the cortex and

roughly halfway between the two cortical edges. T A total of eight accumulations were taken for each sample at 10mW with 60 seconds acquisition time for each accumulation. These parameters (power, number of accumulations, acquisition time) were selected after recording test spectra using a range of conditions. The selection of final parameters to be used was based on the resolution and signal to noise in these test spectra, comparison of R^2 values once the spectra had been fitted, time taken for data collection, and also the maximum time which would avoid burning.

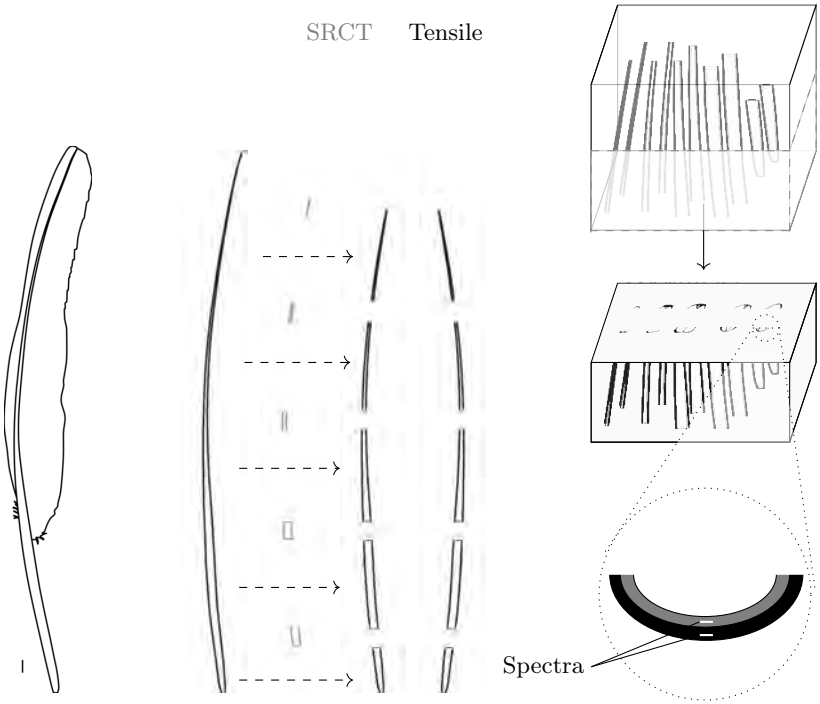

Figure 3.11: *A schematic diagram shows how samples are prepared for Raman spectroscopy and the locations from where spectra are taken from the Tensile pieces. The vane is removed from the shaft, which is cut into pieces. Small pieces were taken for CT scanning, and larger pieces were reserved for tensile testing. After tensile testing, these pieces were embedded in resin, bisected, and polished for spectroscopic analysis. A similar process was used to prepare samples from different species, but this time only at 40% length and spectra were taken from the dorsal, ventral, leading and trailing positions*

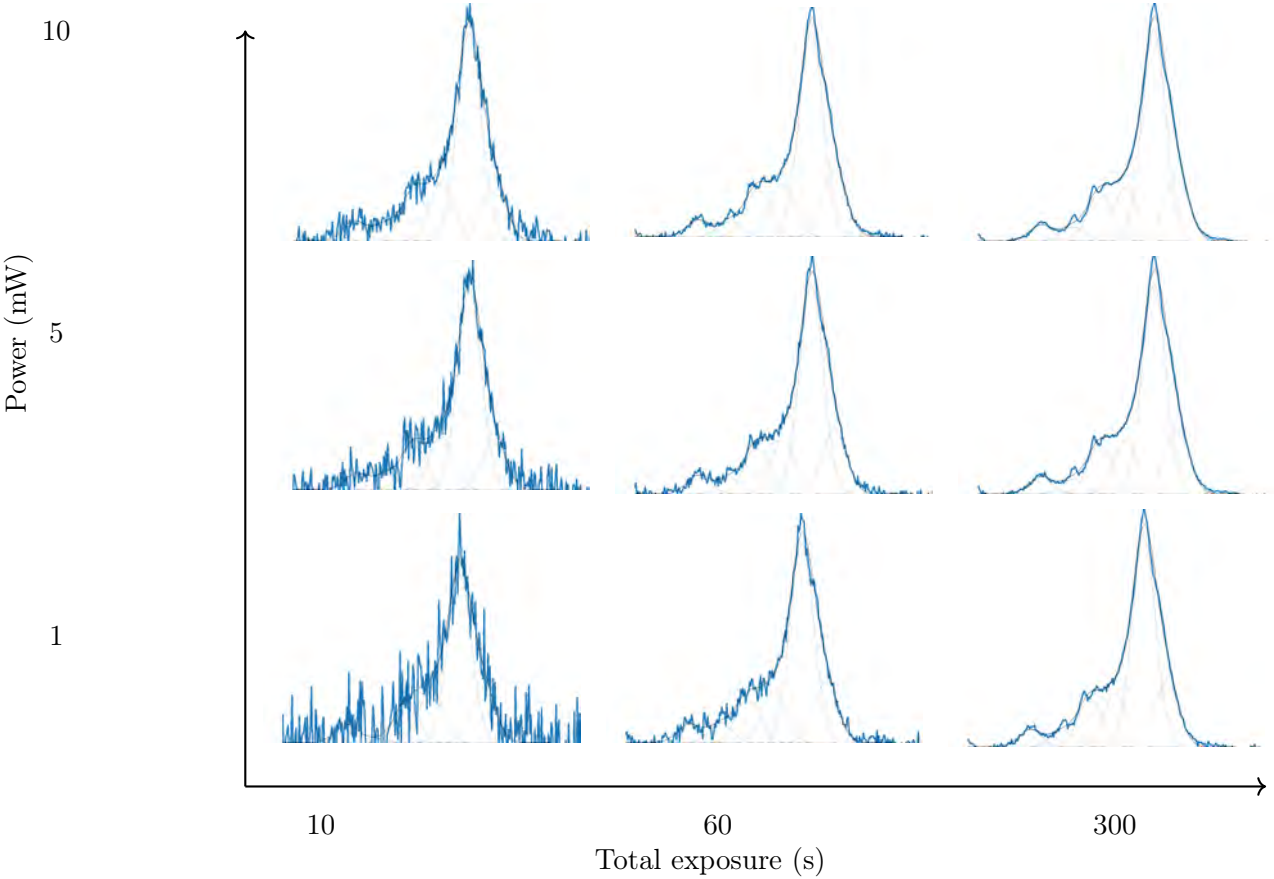

Figure 3.12: *Continued on next page*

Figure 3.12: *A figure to show how increasing power and exposure leads to an improved spectrum with better signal to noise in the Amide I region. The axes obscure the data and so they are not included. However, they match those in figure 3.13. The Y axis is scaled intensity and the x axis shows wavenumbers (cm^{-1}) from 1500 to 1800. The orange lines are the recorded data, the black line is the sum of the six-band Gaussian fit, and each of those six is shown with a grey line. In this work, the settings used were 60 seconds exposure, for 8 accumulations (8 minutes total exposure) at 1mW. These settings balanced the time needed to acquire data with the risk of sample burning and returned spectra with good signal-to-noise that were normally fitted with $R^2 > 0.99$. In this figure, the R^2 values are as follows:*

0.97789	*0.99613*	*0.99701*
0.95524	*0.99485*	*0.99657*
0.8676	*0.98984*	*0.99618*

3.3.1 Spectral regions investigated and band fitting of Raman spectra

Although experimental spectra were obtained between 3,200 $cm^{-1}$and 100 cm^{-1}, particular attention was given to the Amide I region (1500 - 1800 cm^{-1}), the Amide III region (1200 - 1350 cm^{-1}), and the SS region (400 - 600 cm^{-1}). Assignments made in these regions follows those in previous work (*Akhtar and Edwards*, 1997, *Blanch et al.*, 2003, *Cai and Singh*, 1999, *Church et al.*, 2010, *Essendoubi et al.*, 2019, *Fu et al.*, 1994, *Hahn et al.*, 2015, *Khosa et al.*, 2013, *Maiti et al.*, 2004, *Zhang et al.*, 2012), and are presented in Chapter 5

The Amide I region arises from C-O stretching vibrations. It provides information on protein secondary structure in the samples investigated (*Akhtar and Edwards*, 1997, *Blanch et al.*, 2003, *Fu et al.*, 1994, *Hahn et al.*, 2015, *Maiti et al.*, 2004, *Zhang et al.*, 2012). The Amide III region (1200 - 1350 cm^{-1}) arises from a combination of N-H bending and C-N stretching vibrational modes. Previously, this region has also been used to investigate protein secondary structure (*Cai and Singh*, 1999, *Fu et al.*, 1994, *Maiti et al.*, 2004, *Zhao et al.*, 2012), notably in cases where infrared spectra were recorded from protein-containing samples in solution, where the water bending mode absorption overlaps with the Amide I region and makes the Amide I region of limited use.

However, in the present work, Raman spectra were recorded for solid samples embedded in a resin matrix and in any case, the water bending absorption is much less intense in Raman spectroscopy than infrared spectroscopy. An initial investigation carried out as part of this work investigated both the Amide I and Amide III regions, and obtained similar information in both regions, though because bands in the Amide III region overlap one another, error bars of the bands fitted in the Amide III region increase (*i.e.* confidence decreases) to a point where the conclusions are much less clear than the Amide I region. Therefore, in this work, only the Amide I band will be investigated. The Amide II region (1510 – 1580 cm^{-1}) is also related to absorptions of combinations of

N-H bending and C-N stretching modes. However, the absorptions observed in this region correspond mainly to change in the H-bonding environment and the Amide II bands are often overlapped by bands originating from amino acid side chain vibrations (*Almutawah et al.*, 2007, *Cai and Singh*, 1999, *Chirgadze et al.*, 1975, *Jackson and Mantsch*, 1995, *Zhang et al.*, 2012). Hence, this region is usually not used for investigation of protein secondary structure because the correlation between secondary structure and band position is much harder to establish than in the Amide I and Amide III regions. The S-S region provides information on the CC-S-S-CC conformation of disulphide bonds in keratin (*Akhtar and Edwards*, 1997). This region was analysed and fitted as part of the initial investigation in this work, but the region suffers badly from background fluorescence and poor signal-to-noise, so band-intensity ratios from this region are not considered any further, though they relate to the the conformations around the S-S bonds in the cystine groups in the protein. These bands are centred at 510, 525 and 560 cm^{-1}. The 510 $cm^{-1}$and 525 cm^{-1}vibrations arise from the CC–S–S–CC band conformations Gauche-Gauche-Gauche (G-G-G) and Gauche-Gauche-Trans (G-G-T) respectively and the 560 cm^{-1}absorption arises from a sulphur-sulphur stretching mode coupled with a cystine residue absorption (*Akhtar and Edwards*, 1997, *Church et al.*, 2010, *Essendoubi et al.*, 2019).

Experimental spectra were baseline corrected and fitted using a script generated using the MATLAB curve fitting toolbox. Following the work by other researchers (*Akhtar and Edwards*, 1997, *Blanch et al.*, 2003, *Cai and Singh*, 1999, *Church et al.*, 2010, *Essendoubi et al.*, 2019, *Fu et al.*, 1994, *Hahn et al.*, 2015, *Khosa et al.*, 2013, *Maiti et al.*, 2004, *Zhang et al.*, 2012), Gaussian bands were used in the fitting (with a half-width of 28.2 cm^{-1}). The number of Gaussian bands used was chosen based on the results of trial fits with different numbers of bands as well as fits performed in these regions by other research groups (*Akhtar and Edwards*, 1997, *Blanch et al.*, 2003, *Cai and Singh*, 1999, *Church et al.*, 2010, *Essendoubi et al.*, 2019, *Fu et al.*, 1994, *Hahn et al.*, 2015, *Khosa*

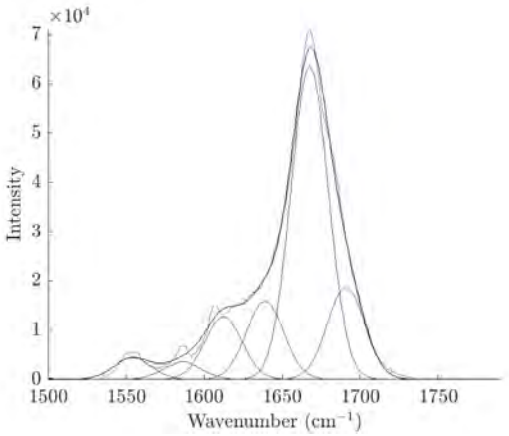

Figure 3.13: *An example fit of data from the Amide I region. The orange line is the data recorded, the black line is the fitted curve from six component Gaussian functions, shown in grey. The spectrum is from the outer layer of the dorsal part of the first primary (P1) from the mute swan (C. olor), taken at 40% length from the base of the calamus. The R^2 value of the fitted curve is 0.9898.*

et al., 2013, *Maiti et al.*, 2004, *Zhang et al.*, 2012), see Figure 3.12.

The Amide I region was fitted with six Gaussian bands and a typical fit is shown in Figure 3.13. A summary of the band assignments made in this region, along with those from previous work is shown in Table 3.3(*Akhtar and Edwards*, 1997, *Blanch et al.*, 2003, *Fu et al.*, 1994, *Hahn et al.*, 2015, *Maiti et al.*, 2004, *Zhang et al.*, 2012). Each band intensity ratio was quoted with an error which is derived from the 95% confidence interval of each fit.

3.3.2 IR spectra

For the sake of completeness, an IR spectrum of a feather rachis sample for a swan is included here and fitted in the same way as the samples in the sections above and in the main text. The infra-red spot-size on the sample was ≈ 1mm and no spatial sampling of the type carried out in the Raman work was possible. As this was only a preliminary spectrum, the sample was investigated “as received”

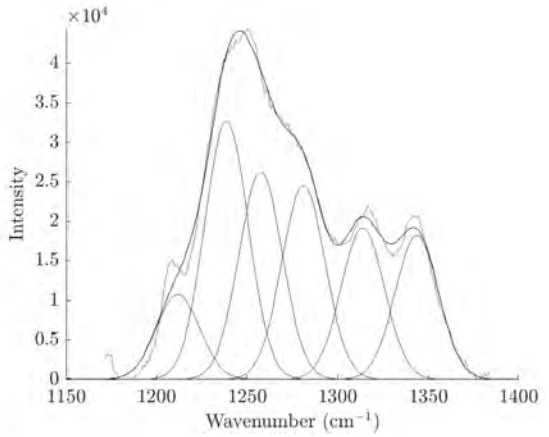

Figure 3.14: *An example fit of data from the Amide III region. The orange line is the data recorded, the black line is the fitted curve from six component Gaussian functions, shown in grey. The spectrum is from the outer layer of the dorsal part of the first primary (P4) from the mute swan (C. olor), taken at 40% length from the base of the calamus. The R^2 value of the fitted curve is 0.9930.*

and spectra were taken from the side of the rachis *i.e* with the infrared beam incident on the side of the rachis not "end-on" as in the Raman work.

The spectrum was taken using a Thermo Scientific Nicole iS5 FTIR Microplate Spectrometer, equipped with iD7 ATR optics and a DTGS detector. The spectrum (see Figure S5.1) was recorded with 16 scans in the range of 4000–400 cm^{-1}at a resolution of 4 cm^{-1}.

Bands were fitted using the same model used in previous sections (See Figure S5.2), though a seven-band fit was used in the Amide I region The fitted band positions are presented in Table S5.1.

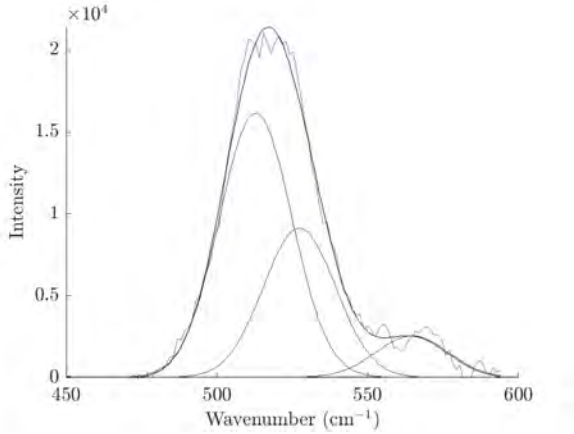

Figure 3.15: *An example fit of data from the Amide III region. The orange line is the data recorded, the black line is the fitted curve from two component Gaussian functions, shown in grey. The spectrum is from the outer layer of the dorsal part of the first primary (P4) from the mute swan (C. olor), taken at 40% length from the base of the calamus. The R^2 value of the fitted curve is 0.9949.*

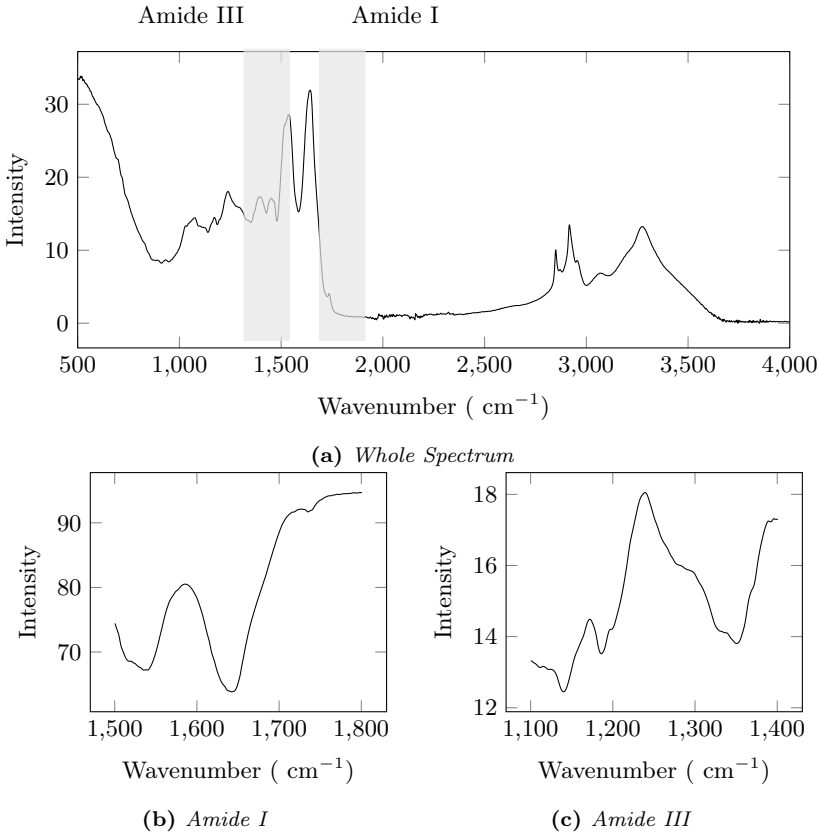

(a) *Whole Spectrum*

(b) *Amide I*

(c) *Amide III*

Figure 3.16: *An IR absorption spectrum of a swan rachis sample shows less detail in the Amide I region than a Raman spectrum. The Amide III region is better resolved than the Amide I region and shows similar features to the spectra obtained using Raman spectroscopy. Bands were fitted using the same model used in previous sections.*

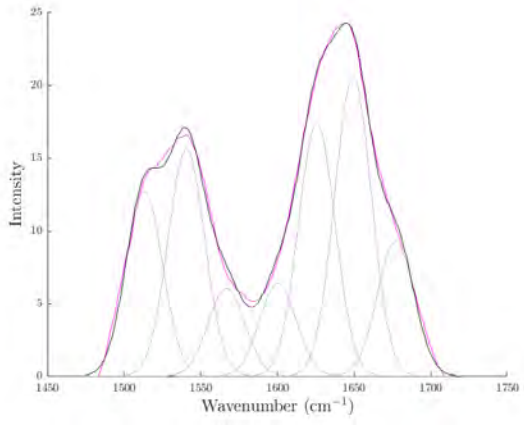

(a) *Amide I*

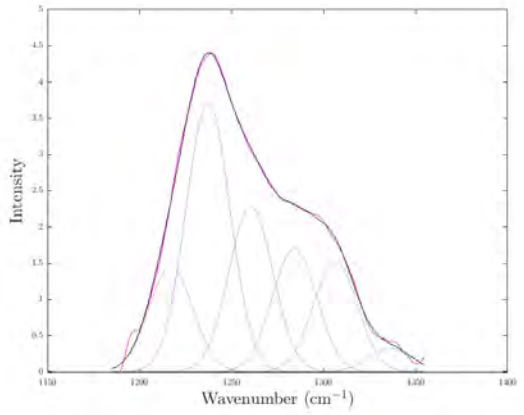

(b) *Amide III*

Figure 3.17: *An example of the fits used for a preliminary IR spectrum obtained of an "as received" rachis sample of a swan . The same method used to fit a Raman spectrum was used to fit an IR spectrum.*

Band	Amide 1			Amide 3			SS		
	Raman	IR	Assignment	Raman	IR	Assignment	Raman	IR	Assignment*
1	-	1515	-	1214	1217	Ring Mode	510	518	G-G-G
2	1553	1542	Ring mode	1240	1237	β-sheet	525	535	G-G-T
3	1585	1570	Ring mode	1262	1261	Random coil	560	558	S-S stretch and
4	1613	1604	Side chain, Ring mode	1283	1284	β-turn			cystine residue absorption
5	1640	1627	α-helix	1313	1306	α-helix			
6	1668	1650	β-sheet	1343	1336	α-helix			
7	1692	1678	β-turn						

Table 3.3: *Band positions from Raman and IR data (G=Gauche, T=Trans). Gaussian bands were used in the fit with a half-width of 28.2 cm^{-1}.*
** These vibrational assignments refer to S-S vibrations of the CC-S-S-CC bond conformations between two cysteine residues (the dimer is formed on oxidation and is called cystine) in keratin, see Akhtar & Edwards(1997).*

Chapter 4

Looking at layers

Imaging layup with Computed Tomography.

Chapter 2 introduced work from a number of different groups (*Bachmann*, 2014, *Busson et al.*, 1999, *Earland et al.*, 1962a, *Laurent et al.*, 2019, 2014, *Lingham-Soliar*, 2013) which together present data obtained using 13 different techniques to image layup in a feather shaft. This body of work establishes that there are differently oriented layers, but does not quantify the layup in a systematic way or even within a single feather. *Lingham-Soliar et al.* (2010) presents a qualitative narrative based on degraded feathers and *Laurent et al.* (2014) presents a semi-quantified layup in a small piece of a single feather.

The method used to collect CT data in this work has been set out in Chapter 3, and a single example has been analysed from the calamus of a swan. It demonstrates how three-dimensional CT data can be conceptually flattened, and fitted ellipsoids can reveal by proxy in which direction fibres are oriented in two different layers. It was presented in Chapter 3 as a protocol due to convention, but the method is a standalone result because this is the first attempt at measuring laminar orientation and thickness in a reproducible way. The development of this method is therefore an important contribution and will be reviewed as the first section in

this chapter. This review includes some important considerations, and limitations, of collecting data using Synchrotron Radiation Computed Tomography (SRCT) that were not presented in Chapter 3 and explains why not all the data which has been collected in the course of this project was usable. Observations on thickness and orientation are presented in Section 4.2. Section 4.2 presents information recorded from feather material in different places from the shaft and although most of the data has been collected from a single feather, it is supported by data from two replicate feathers. Then, the data presented by *Laurent et al.* (2014) will be reinterpreted in Section 4.5, using the software protocol developed in this work. A summary of the chapter will follow.

4.1 Method development

The method used to gather, process and present data on orientation and thickness includes many steps and many potential failure points. As a working method is something of a result in itself and because the author hopes work in this area will continue, these points are covered in more detail over the next four sections and summarised.

4.1.1 Bird material, dissection and storage

Although the results are not included in this work, CT data was acquired on more taxa than just the swan. Unfortunately, much of this data has not been usable. This is due in part to some of the factors considered below but is mostly to do with the size of the feather. Swans have very large feathers and are probably the most easily accessible taxon with large feathers available in the UK. The primary feathers of an adult swan have a cortical thickness between approximately 0.1 and 0.5 mm. They are easily handled, sectioned and then mounted for CT scanning.

Birds with feathers much smaller than those of a swan have proven to be much more difficult to section and mount, and seem

to have smaller and less frequent cortical holes. Such holes are also more easily obscured by artefacts of the CT method such as noise and movement and it will be shown that even with large swan feathers, the technique at the time of data collection was at the edge of its capabilities

Feathers of smaller birds can usually be pulled out by hand, but the flight feathers of larger birds are not easily removed and it is difficult (often impossible) to remove a flight feather without damaging it in one way or another. With that in mind, this project has found that dissecting the follicle with a scalpel, letting the wing biodegrade, and even boiling the soft tissue of the wing did not make the removal of the flight feathers, without damaging the rachis, any easier. The best way to remove the feather from its follicle is with some pliers. This is actually quite easy but it will damage the feather so care should be taken to grip the feather at a place which will not be observed during the course of experimental measurement.

Once feathers have been removed from the follicles, they should be stored in an envelope at room temperature and pressure.

4.1.2 Mounting method

Two methods were presented in Figure 3.2 for holding samples on the synchrotron beamline. Both of these methods involved fixing a piece of feather shaft to an SEM stub. In original experiments by *Laurent et al.* (2014) the sample was held directly in the jaws of a drill chuck which is already mounted in the CT scanner. Synchrotron beamlines usually present a microscope stage rather than a chuck and users often make their own fittings.

Both methods can be used to scan material at a synchrotron beamline and one additional method was considered whereby a small, matchstick-shaped piece of shaft was excised and placed inside a carbon fibre tube such that 2 mm of feather shaft was left protruding from the tube. The shaft could then be filled with resin, glue or wax. This method was quickly set aside because the samples are buoyant and filling the tube with resin is difficult,

messy and resulted in the destruction of samples.

The two methods are as follows:

Method 1 (which involved sticking a matchstick shaped piece directly onto the SEM stub, see Figure 3.2) was semi-successful. Attaching the sample to the SEM stub proved quite difficult and there was a considerable number of failures. Glue did not always adhere to the stub surface or the sample would move out of place before the glue dried. Successfully glued samples moved and vibrated during scanning which meant no usable data was recorded.

Immobilising the sample in blue-tack and gluing the blue-tack to the stub prevented some movement. However, the blue-tack often became detached even if stored carefully in a specially designed stub-holder box. Embedding the feather in paraffin wax was more successful and usable data was collected for a number of samples. However, samples prepared in this way were still very delicate, and difficult to store and transport. When wax was used to stabilise the sample, and no small movements or vibrations were detected. It was found that the wax may soften and cause the sample to move during a long beam exposure though this was unusual.

The advantages of this method are that the medullary foam can be removed and there will be no region-of-interest artefacts, because the entire sample would fit inside the field of view. However, preparation is delicate and time consuming work, and storing the samples is difficult.

Method 2 involved gluing a whole cross section of feather shaft to the SEM stub and scanning the imaginary matchstick as a region of interest. This method is much easier to prepare, much more stable while glue is drying and attaches a much larger surface area to the SEM stub, which makes it more secure. Samples can be easily stored and transported in SEM stub-boxes. However, artefacts arise from phase changes in the medulla, which have to be overcome by making sure that the scan rotates the sample through 180° such that the rest of the sample is never upstream of the region-of-

interest. This, along with appropriate reconstruction and filtering seems to resolve most of the problem. The advantages of this mounting approach are securely mounted samples which do not move or vibrate, which are not contained in an X-Ray absorbing or scattering medium and which can be stored and transported easily. The disadvantages of this method are region-of-interest artefacts and some time and difficulty in scan setup, where mistakes are easily made after a long day in a time-pressured environment.

4.1.3 Acquisition parameters

The problem of optimising acquisition parameters for CT scanning is a multi-dimensional one. The factors to be considered are sample preparation, acquisition time, the number of projections taken, frame averaging, beam energy, beam frequency, beam filtering, scintillation, detection and many more. These might also change upon selecting a particular reconstruction algorithm. So, in order to record data of high quality, some kind of pilot scan and hopefully a small parameter sweep is necessary. With so many variables at play, the process of finding an acceptable image must be an incremental one guided by an experienced eye. Of course, it is likely that the first scan may be almost acceptable, and with a bit of luck may even be good *enough*.

However, CT facilities around the world are oversubscribed and time is expensive, so it is unlikely that one or two pilot scans can be performed. Such over-subscription and expense means that (especially for academic time at nationally funded synchrotron light sources) there is usually some kind of competitive application process for beam-time. A key factor in success at this stage is the presentation of pilot data. Thus, a circle is created; beam-time requires pilot data, but pilot data requires beam-time.

The salient point here is that the resulting scan must be good *enough*, because a truly artefact-free tomogram is quite elusive. Some of the data collected in this work has been good *enough*, but some has not. Crucially though, while collecting data which has not been usable has limited the scope and impact of this chapter,

the process has revealed some ways in which the method could be improved. Those improvements will be considered again in Chapter 9.

Beam energy Ten projections of the same sample were taken at 8, 11, 14, 17 and 20 keV at the Diamond Light Source. After flat-field correction, projections were averaged and Weber contrast ratios were calculated. It was concluded that 14 keV was the most appropriate energy for the scanning of feather keratin. This is lower than scans performed at the µ-vis X ray imaging centre, Southampton. 80 keV was used at on a bench-top machine at Southampton and 22 keV was used at the Swiss Light Source.

Number of projections Scan quality increases with the number of projections (*Kak and Slaney*, 2001). The theoretical value to fully resolve a volume is calculated as follows (*Dudgeon and Mersereau*, 1985):

$$N = \frac{\pi \cdot d}{R} \tag{4.1}$$

where N is the number of projections in 360°, R is resolution in nanometers and d is the diameter of the region of interest, also in nanometers (*Dudgeon and Mersereau*, 1985). 4000 projections would be needed to fully resolve a volume of $\approx 0.8mm^3$, scanned at 325 nm voxel resolution with 180 degrees of rotation.

Rotation speed and step Depending on the stage present at the beamline, the stage might rotate and then stop, and take an acquisition, or it might make use of a *flyscan*. A flyscan is a term given to the practice of using a slower rotation speed, and taking exposures of a moving sample. This is *much* faster if the beamline setup allows this mode of operation, but usually requires taking more frames for a shorter exposure, which creates more data (though this can sometimes be reduced by averaging consecutive frames).

Other variables More variables have been listed at the beginning of this section such as scintillation, exposure time, filtering and collimation. They are important but should only be considered with the help of a beamline scientist. They are mentioned here only to present what is not considered. Books such as *Kak and Slaney* (2001) and *Banhart* (2008) are good resources for background information and guidance in planning an experiment. Automated sample loading robots, scripting, and clever tricks to place two samples on one pin can also save time (possible if scanning through 180°of rotation.

4.1.4 Reconstruction

Some reconstruction methods have been mentioned in Chapter 3. During the course of this project, data has been acquired and reconstructed using a range of parameters and scan set-ups at different beam-lines. It has become clear that the choice of reconstruction algorithm is an important one, and data reconstructed with all the major classes of algorithm are subsequently presented here. The CT scan presented by *Laurent et al.* (2014), and some of the pilot scans used to apply for beam-time during the present work were reconstructed with a filtered back projection algorithm. The GridRec algorithm (a Fourier gridding approach) and the Paganin algorithm (a phase-retrieval approach) were used at the Swiss Light Source and the Tomo-Recon algorithm (a filtered back-projection approach) at the Diamond Light Source. Two additional datasets have been reconstructed using the SART algorithm (algebraic reconstruction) and the results obtained were included in the discussion so far as they relate to the scanning of bird feathers.

Reconstruction practices at synchrotron beamlines will be outlined before these algorithms are considered to show that the resources needed to perform a rigorous pilot study before arriving at a synchrotron beamline are not commonly available.

Reconstruction methods used at synchrotron beamlines and evolving standard practice

At the time of data acquisition, tomographic beam lines did not offer many different reconstruction algorithms. Usually there was an option to use a phase-retrieval algorithm, but this requires extra setup time and expertise to find the correct sample-to-detector distance. For most purposes, light sources had a 'data pipeline' that is developed in house and is as close to fully automated as possible. Using these quasi-automated pipelines with a computing cluster based at the light source meant that users could reconstruct their data quickly and efficiently, such that they may be able to adjust scan parameters during their beam-time under guidance from a beam line scientist.

Light-source based reconstruction is a technical and demanding area. Normal users probably lack the expertise, software and computing power to be able to reconstruct their scans away from the light source. There are open source options available to the expert, but by far the best option is to reconstruct projection data at the light source, and a careful user would have consulted their beam-line scientist ahead of time, and considered pilot data wherever possible.

However, what this does mean, is that a user might return home with many terabytes of reconstructed data which look reasonable visually, but without knowing whether advanced analysis is going to work, and probably without comparative scans that had been reconstructed using a different algorithm.

In this work, multiple scanning sessions have been completed at two different light sources and data has been reconstructed using a number of different algorithms. A comparison of these reconstructions is especially useful now that computers and storage media have advanced, and a number of light sources have implemented pipelines which enable a lay-user to reconstruct data themselves. Without some experience or at least sample reconstructions using similar material, a lay-user would struggle. For example, the Savu tomography reconstruction pipeline (*Atwood et al.*, 2015) is a

python package now in use at Diamond Light Source (though not at the time of acquisition) which has implemented a large number of reconstruction algorithms. It has also become standard practice at the Diamond Light Source to allow remote access so that users can make use of the Diamond Light Source computing cluster and storage for a limited time after their beam time finishes. Similar advances have been made at the the Swiss Light Source (*Buurlage et al.*, 2018, 2019).

Reconstruction algorithms and example tomograms

Tangible differences in the tomograms resulting from different methods, as well as recent developments in reconstruction and computational ability for the end user, warrant a comparison of different reconstruction algorithms. However, it should be noted that tomographic reconstruction can only produce high-quality tomograms from high-quality projections.

Three main classes of algorithm will be presented here. The earliest tomographic reconstruction algorithms use algebraic reconstruction. The grey value of each voxel is calculated by summing line integrals of every photon path which passes through it. The algorithms are very computationally expensive, though with the pace of computer hardware development some new algorithms use iterative methods to reconstruct them several times over.

The second is a filtered back projection type algorithm. This algorithm reconstructs tomograms from projection data (sinograms) by applying a high-pass filter and then a backward projection step.

The third class of algorithm reconstructs the data in Fourier space and maps it back onto a Cartesian grid. More information on these algorithms can be found in the literature (*Willemink and Noël*, 2019).

It will become clear from Tomo-Recon (FBP) and SART (algebraic) reconstructions, see Figures 4.1 and 4.4, that data did not have a sufficiently high number of projections and contain the region-of-interest artefact. The GridRec (Fourier) reconstructions look better than these reconstructions despite having a smaller

number of projections. This is because of the way the data in Fourier space are mapped onto the Cartesian grid, explained in the original paper by *Dowd et al.* (1999):

> With the FFBT [Fast filtered back transform] algorithm, a somewhat different technique called "gridding" is employed. Gridding was first developed by radio astronomers for use in aperture synthesis as a means to back-transform irregularly sampled Fourier data. Since then it has been suggested as a robust method of reconstruction for computed tomography and implemented for MRI data. In this method, the data on the polar grid are first weighted (or "filtered") by factors which take into account the non-uniform area elements on the polar grid. The weighted data set is then mapped onto a Cartesian grid – not by simple interpolation, but by convolution with the Fourier transform of a certain function, w(x,y). Next, the 2-D inverse is applied, and finally, the resulting image is divided by w(x,y) to correct for the effects of the convolution.

According to Equation 4.1 on page 74, it was calculated that ≈ 4000 projection would have been needed at the Diamond Light Source. This already makes scan time and the size of data more than twice as large as a dataset containing only 1500 projections. However, the scans at the Diamond Light Source *were* recorded with 4000 projections. This is therefore an intrinsic problem of RoI scanning, though it is suggested by *Kyrieleis et al.* (2010) that increasing the number of projections such that the d represents the whole sample and not just the RoI mostly solves the problem. However, this would require something like 30,000 projections, the scan time would have increased to approximately three hours and the dataset would be $\approx$ 600GB which is unfeasible for a large number of samples (it would cost £20 per scan just for Hard Drive Disk (HDD) space, not including the reconstruction).

So it seems that using a Fourier gridding algorithm is the most sensible choice in terms of tomogram quality, scan time and data

size. At the time of writing, non-specialist single workstation tools do not have enough memory and are not really able to perform most reconstruction tasks in reasonable times (even with graphics-card optimised algorithms). A computing-cluster is needed as well as software for reconstruction to be possible at an off-site location.

The digital storage of tomographic experimental data, the available reconstruction tools and even the availability of technicians for consultation and advice is very heterogeneous at synchrotron light sources and other CT facilities around the around the world. This is to be expected as facilities are often oversubscribed and / or expensive to access, and because the technique has become so ubiquitous, no beamline scientist could be expected to be familiar with every sample material they might come across.

Algebraic reconstruction (SART) The Octopus software package for Windows by TESCAN (Brno, Czech Republic.) was used to reconstruct two datasets (acquired at the Swiss Light Source, see Chapter 3 for acquisition parameters) in cone-beam mode using the SART algorithm (*Andersen and Kak*, 1984). A high-end desktop computer was used (A Dell T7500s with 192G RAM, 12 CPU cores and twin nVidia Quadro graphics adapters) to reconstruct 10 tomograms only (RAM limited), which took approximately 2 hours for each set of 10 tomograms. 10 tomograms were reconstructed to enable post-reconstruction filtering.

The software is normally used to reconstruct data acquired on bench-top CT scanners, which usually come in cone or fan beam setups. This data was collected at a synchrotron light source that produces a parallel beam and is not supported by the software. However, reconstruction can be forced by using a method intended for cone-beam CT and setting the source-to-sample distance to a very large value, thereby approximating a parallel beam. Reconstruction by this algorithm usually dispenses with many artefacts which are introduced by various time-saving tricks employed by other reconstruction algorithms. This is more computationally intensive by a factor of approximately 1500 when compared to

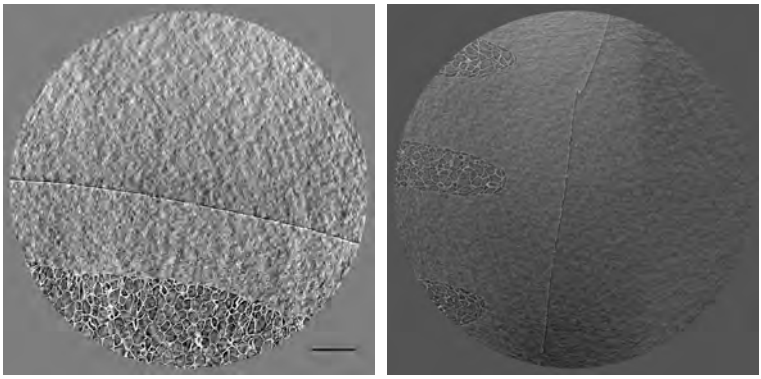

(a) *SART* **(b)** *SART*

Figure 4.1: *Tomograms which show two SRCT datasets reconstructed using the SART algorithm. These reconstructions show clear region-of-interest artefacts and some speckled noise, though cortical holes are resolved and contrasted. Subfigure* ***a)*** *shows a first primary (P1) at 30% length, in the leading position; it shows two layers, subfigure* ***b)*** *shows the dorsal part of the same feather at 50% length, which appears to have only one layer.*
Scale bar *(bottom-right of subfigure* ***a)*** *is 0.1 mm and applies to both subfigures*

GridRec and would usually require proprietary software.

Unfortunately the software has now been discontinued and the computer remains hugely oversubscribed because the software was only available on single licenses before it was discontinued. The size of a full stack of tomograms depends on the size of detector used for acquisition but between 2000–2500 tomograms is normal, which equate to hundreds of hours of reconstruction time. Figures 4.1a and 4.1b show tomograms from each dataset. Both tomograms show very obvious under-sampling artefacts, and though not so easily observed in these tomograms, some cortical holes are visible. 4000 projections were recorded.

Reconstruction in the Fourier domain (GridRec) Reconstruction using the GridRec algorithm was performed at the time

of acquisition using the software pipeline and computer cluster at the Swiss Light Source (*Marone and Stampanoni*, 2012). Reconstruction of the whole volume took approximately 10 minutes plus queue time. Only 1500 projections were recorded. A direct time comparison with the SART reconstructions mentioned above is not possible due to the very different hardware used but the GridRec algorithm is ≈1500 times faster (*Marone and Stampanoni*, 2012). Figures 4.1 and 4.2 show how this method compares to the SART algorithm for two samples. It is clear that the GridRec algorithm does not resolve the region-of-interest artefacts that are so obvious in the SART reconstruction, though a ring artefact is observed in both examples. For the datasets presented it is clear that GridRec produces clearer scans which are more easily thresholded for subsequent analysis, though they would have benefited from some sinogram filtering to remove the ring artefact.

Phase-contrast reconstruction (Paganin) Reconstruction using the Paganin algorithm was performed at the time of acquisition using the software pipeline and computer cluster at the Swiss Light Source. Reconstruction of the whole volume took approximately 10 minutes plus queue time. Figure 4.3b shows that no ring artefacts are observed using this algorithm and less speckled noise was observed. 1500 projections were recorded, and there is less noise but the phase-edge artefacts observed would not be helpful on each cortical hole.

Filtered back projection Reconstructions using filtered back projection algorithms were performed at the µ-vis imaging centre in Southampton using a high-end desktop computer and with a computing cluster at the Diamond Light Source. Data were reconstructed overnight using a batch system on the PC, and took approximately 10 minutes plus queue time at the Diamond Light Source. Figure 4.4 shows lots of speckled noise in the data and obvious ring artefacts when brightness and contrast is adjusted.

Of these different reconstruction algorithms, those reconstructed

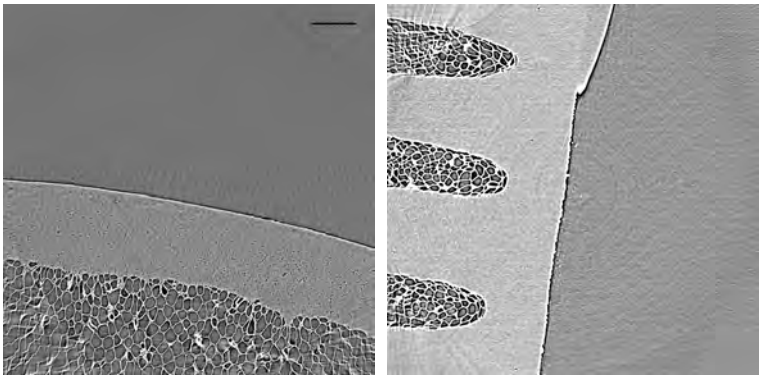

(a) *GridRec* **(b)** *GridRec*

Figure 4.2: *Tomograms which show two SRCT datasets reconstructed using the GridRec algorithm. Compared with Figure 4.1 overleaf, which reconstructs the same data using an algebraic approach, these reconstructions have much better signal-to-noise but do introduce a ring artefact. Cortical holes are resolved and contrasted. Subfigure* ***a)*** *shows a first primary (P1) at 30% length, in the leading position and clearly shows two layers), subfigure* ***b)*** *shows the dorsal part of the same feather at 50% length, which appears to have only one layer.*
Scale bar *0.1 mm and applies to both subfigures*

using GridRec were clearer, smaller and more quickly reconstructed. However, there is room for improvement with additional filtering, *e.g.* by filtering sinograms to reduce the ring artefacts. This case is made once more in Chapter 9, which summarises the main conclusions of the thesis and suggests further work.

Computational power in reconstruction and image analysis

Software availability Open source solutions are available but it is beyond the scope of this project to investigate them. At the time of image acquisition the use of different algorithms was not practicable at either the Swiss Light Source or the Diamond Light Source, though Diamond Light Source have recently introduced

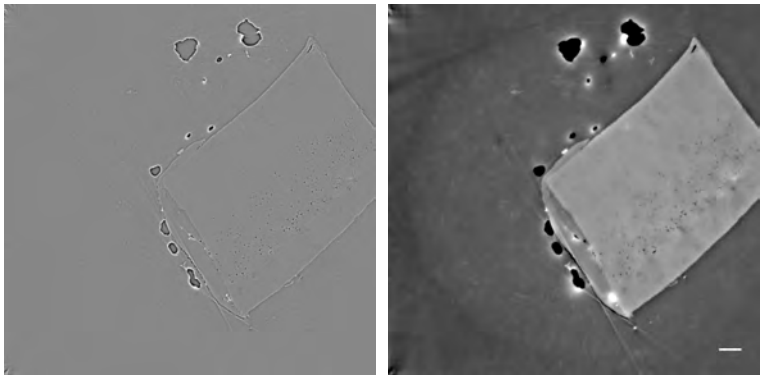

(a) *GridRec* **(b)** *Paganin*

Figure 4.3: *A figure which shows a dataset reconstructed with the GridRec algorithm (left) that uses a light-as-a-particle model and the Paganin algorithm (right), which uses a light-as-a-wave model.* ***Scale bar*** *0.05 mm and applies to both subfigures.*

a new reconstruction pipeline (*Atwood et al.*, 2015), which has made it possible for end-users to reconstruct data themselves using a number of different algorithms and filtering protocols which can be customised for particular data. Unfortunately this was implemented some time after the beamtime sessions for this work had finished. Access to a 'Data beamline' at the Diamond Light Source is now available by application, though this is actually two desktop computers, and the cluster is not necessarily accessible. This will be discussed more in Chapter 9.

User Interface and Cluster Computing FIJI is a popular open-source software package which focuses on biological-image analysis and runs on Java (*Schindelin et al.*, 2012).

An important package used in this work is the BoneJ plug-in (*Doube et al.*, 2010) for FIJI, which has been used to fit the ellipsoids to the cortical holes in computed tomography volumes.

It was developed to work with CT data of bones, and the feature which fits ellipsoids was intended for use in trabecular bone,

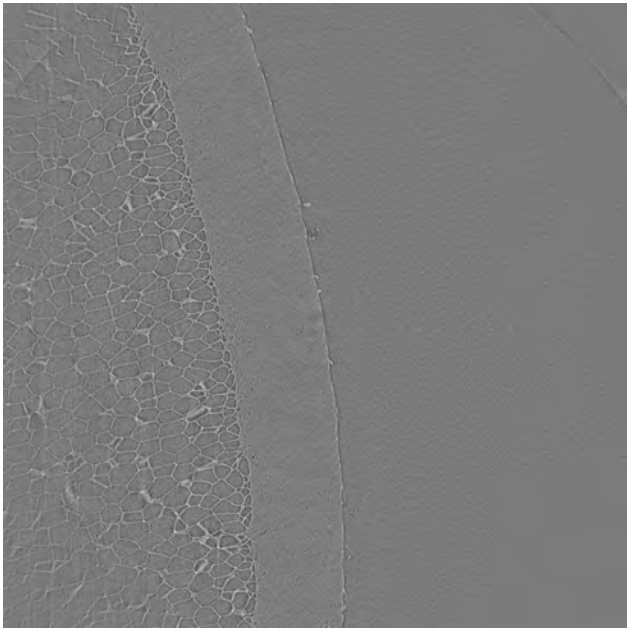

Figure 4.4: *A figure which shows an SRCT dataset reconstructed with the Tomo-Recon algorithm (filtered back projection). This data does not show a swan's primary, but one from the common pheasant, Phasianus colchicus. To an experienced eye, two layers are visible and the outer layer does appear to have holes, but speckle noise and the ring artefacts obscures data such that the histogram method presented in Chapter 3 did not work, even after trying a number of filters on the tomogram data. Figure 2.3 on page 10 also used a filtered back projection algorithm, but achieves much clearer data. This figure measures 0.8 mm from edge to edge.*

where spaces are hundreds of times larger than the holes investigated in this work and CT data sets are correspondingly smaller—small enough for analysis to run on a desktop PC.

This is not possible for the data acquired on holes in the feather cortex and as such the analysis needs to be run on a computing cluster.

A lot of time was spent trying to run the analysis protocol presented in Chapter 3 with the batch scheduling systems required for cluster computing with limited success because FIJI requires a GUI.

If thresholding could have been successfully automated then this may have been achieved. In the end, a new visualisation service came into operation in 2019 on the IRIDIS 5 computing cluster at Southampton which made graphical interaction possible, but analysis then comes with a significant time cost. This is known as 'transaction processing' or 'interactive processing'. For most big data applications, 'batch processing' is preferred, whereby a script is submitted to a job scheduler, which forms a queue and submits jobs such that computational resources can be used efficiently.

4.1.5 Summary

As the preceding section was quite large and covers several areas, it is useful to summarise the main conclusions. They are as follows:

Sample preparation Method 2 (pictured in Figure 3.2 on page 43) is certainly the best method of sample preparation. With this method, the samples are mounted securely and do not move or vibrate during the scan or in transport / storage. The method is simple and the possibility of sample destruction or human error is greatly reduced.

Acquisition parameters Although the most usable projections were measured in a 21 keV beam, a subsequent parameter sweep revealed that 14 keV would yield the best contrasted images (*Lau-*

rent et al., 2019). It should be noted that this is not the recommended value for bench-top CT machines, where the energy would be roughly three times higher (21 keV was selected because pilot scans on a bench-top machine at 80 keV were successful (*Laurent et al.*, 2019, 2014). This value could also be calculated if μ was known.

It has also been observed that faster shutter times, more projections and a continuously rotating stage facilitate much shorter scan-times to obtain equally good data. This is the reason that scan times were just 7 minutes at the Swiss Light Source but more than 20 minutes at the Diamond Light Source. The time saved here can then be used to scan a larger number of samples or to scan the same sample more thoroughly. The number of projections must also be considered from a resource/cost perspective because hard disk drives are expensive and from a computer-time perspective because computation and storage also increases.

These factors become particularly important if Method 2 is to prepare samples because certain artefacts are introduced by region-of-interest scanning (this will be considered more thoroughly in the next section) in samples where the region of interest is contained within or situated adjacent-to extraneous material, such as those prepared using Method 2. These artefacts can also be greatly reduced if the rotation of the sample in front of the beam is planned such that the beam passes through as little extraneous material as possible before it passes through the region-of-interest. The formula to calculate the optimum number of projections has been presented earlier in this section with guidance of how it should be applied to region-of-interest scans. Final acquisition parameters are listed in Section 3.1.1.

Reconstruction Due to the complex nature of reconstruction and that pilot data from bench-top machines have a number of small differences from the data collected at synchrotron light sources, it is difficult to carry out a rigorous pilot study before arrival at an SRCT beamline. It is also the case that beamlines at differ-

ent synchrotrons will also have subtle differences, similar to scans taken using bench-top machines made by different manufacturers.

Considering the data presented above and points made about computational power and data storage, it seems that the best reconstruction protocol would employ a Fourier-gridding algorithm. This has the advantages of requiring fewer projections, less storage and less computational power but still presents ring artefacts. These artefacts however, could be improved with some additional filtering (of sinograms) and with slightly more projections.

Reconstructed data from the Diamond Light Source contained ring artefacts, noise and region-of-interest artefacts. Presently, the data is not usable, though it is possible that some of this data might be usable with a different reconstruction protocol, which would include either filtering projections before reconstruction, using a different algorithm, or both. This would represent a large amount of work, require access to a computing cluster and expert knowledge of image processing. Reconstructed data from the Swiss Light Source *is* usable but contains some ring artefacts. Results from this data are presented later in this chapter.

Computational power This section has presented standard practices for tomogram reconstruction. It also warns of the computational power needed for image analysis using the methods listed in Chapter 3 and the cost of storing that data. These points should be taken into consideration in the planning of any further work and are discussed in Chapter 9.

4.2 Computed tomography and laminar geometry

This method outlined in Chapter 3 has been applied to multiple places around and along the first primary (P1) from three swans (*C. olor*), and histograms were generated using the method outlined in Chapter 3.

4.2.1 Layer thickness around and along the shaft

The method presented in Chapter 3 did not detail exactly how many samples were scanned, because in the development of the method many scans were carried out which do not contain usable data. These included scans from different feathers on the wing and from different species and are reconsidered in Chapter 9 which deals with further work. This section presents a large number of scans at 5 length-wise places on the feather, using Method 2 (cylindrical sections) from page 43. The scans overlap, which gives more weight to the results of individual scans, whilst allowing variation to be seen because a mosaic of sub-sample datasets is used which covers the whole sample. This number of scans cannot be replicated because of a huge time commitment, but a smaller number of scans on replicate feathers reinforce the results.

Figures 4.5-4.9 show the coverage of SRCT scans for sections removed at 10, 30, 50 , 70 and 90% of the shafts length from the tip of the calamus. Figure 4.5 shows there are two layers in the calamus at 10% shaft length. The mean thickness for the inner layer is 79.9% of the total thickness but varies between 65.5 and 100.0%.

The part where the inner layer spans the complete cortical thickness could indicate that the deposition of the outer layer by keratinocytes in the follicle does not switch off at a single point in time and instead forms a tapered termination on the leading edge of the feather. This part of the feather is where the vane attaches a little further up.

Lingham-Soliar (2017) reports that the fibres which constitute the ramus are continuous with the longitudinal fibres of the rachis. This structure would mean that the leading and trailing edges of the rachis could not include an outer layer. *Lingham-Soliar* (2015) actually makes three competing claims over the course of his work (each of which are all well argued and supported with evidence), which demonstrates the difficulty in characterising feathers and the need for an automated or semi-automated technique. So, it is not yet appropriate to claim that there are two layers in the part of the

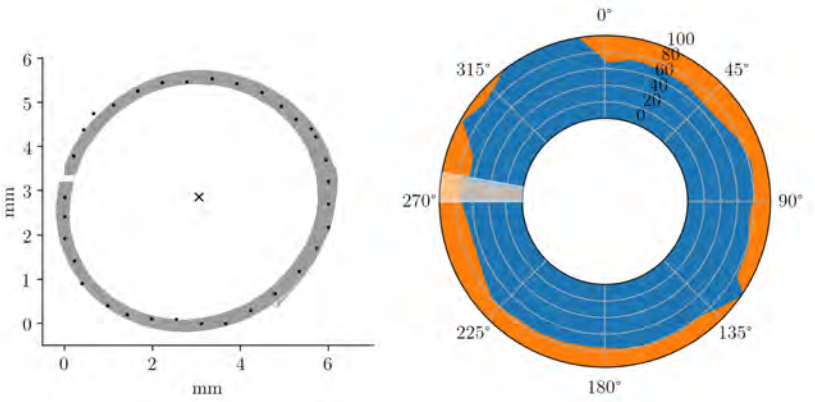

Figure 4.5: *A figure in two parts which shows the thickness of the inner layer using data on cortical holes in a sample taken from 10% shaft length. A mosaic of CT scans of a swan's first primary (P1) is shown on the left with a black showing the centre of 33 SRCT scans (n=33). The leading edge of the feather is on the left of this image. A polar graph on the right shows the thickness (%) using data extracted from two-dimensional histograms like those presented above. Blue indicates that fibres are axially oriented. Orange indicates an outer layer, which has radially oriented fibres.*

calamus beneath the vane attachment, and only one layer above the point of vane attachment and this point is firmly disproved by clear evidence of two layers further up the shaft, which are presented later in section 4.4 on page 108.

Figure 4.6 shows that the outer layer observed around most of the circumference of the calamus is not present by 30% shaft length and the entire cortical thickness is then composed of fibres oriented longitudinally. All 35 overlapping scans indicated 100% thickness of the longitudinal layer. The same is true of Figure 4.7 which presents overlapping data from 22 scans taken of a section at 50% length, Figure 4.8 shows 17 scans of overlapping data taken from 70% shaft length and Figure 4.9 which shows data from 7 overlapping scans taken at 90% shaft length. This data shows that the whole cortical thickness is composed from longitudinally oriented

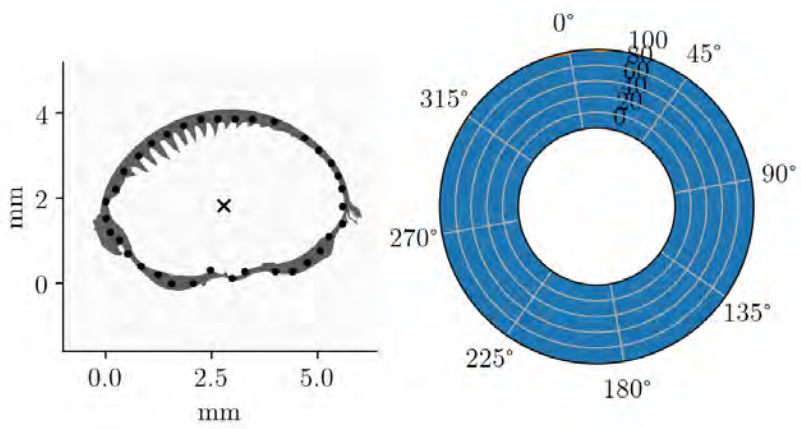

Figure 4.6: *A figure in two parts which shows the thickness of the inner layer using data on cortical holes. A mosaic of CT scans is shown on the left with a black dot on the centre of 35 SRCT scans (n=35) taken from a sample cut at 30% shaft length. A polar graph on the right shows the thickness (%) using data extracted from two-dimensional histograms as presented above. These fibres are axially oriented.*

material, and if the subsequent section on orientation shows no pattern of variation it might be appropriate for a single scan to represent the layup of the whole section, so long as the section is well clear of the superior umbilical region.

Given the overlap of data, results are very convincing that in the first feather, there are only two layers in the calamus and one in the rachis. These results reinforce the proposal made by *Maderson et al.* (2009) of a superior umbilical region, as a zone rather than line of delimitation between calamus and rachis. However, the scanned volume is just 0.8 mm on each side and more scans would be needed proximally and distally to confirm this proposal properly. This could potentially be accomplished by future workers using optical methods.

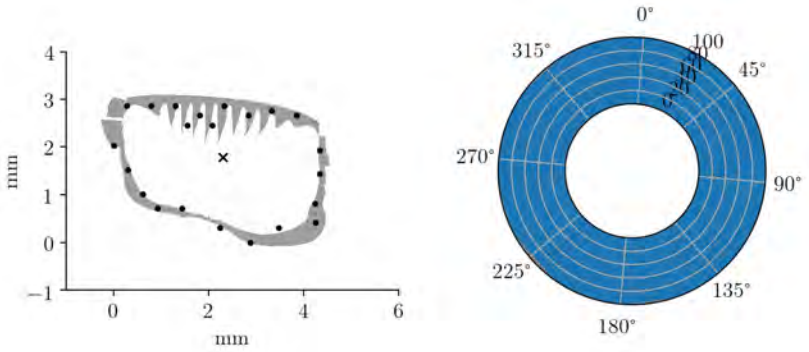

Figure 4.7: *A figure in two parts, which shows the thickness (%) of the inner layer using data on cortical holes. A mosaic of CT scans is shown on the left with a black dot on the centre of 22 SRCT scans (n=22) taken from 50 % shaft length. A polar graph on the right shows the thickness using data extracted from two-dimensional histograms as presented above. Blue indicates that fibres are axially oriented.*

Replicate feathers

Figure 4.10 collates the polar cortex diagrams presented in preceding figures into one. Figures 4.11 and 4.12 then present replicate data on two more feathers. In some cases *e.g.* the 90% section in Figure 4.12, the data is a lighter colour. This overlay indicates that real data is not present and the layer thickness is an interpolation. This is necessary because too few holes were detected to form a signal of sufficient quality. Both figures present data from the first primary of a swan and each section is only scanned four times; at the dorsal surface and the ventral surface and at the leading and trailing edges. An outer layer is observed in the 10% sections, in all four locations, of both the second and third replicate feathers, with average thicknesses of 17.7 and 24.4% respectively. The outer layer also extends into the sections taken from 30% shaft length in both replicates. In the second bird, the outer layer is observed at the dorsal and leading positions with an average thickness of 16.3%, and it is possibly detected at the trailing position but as it

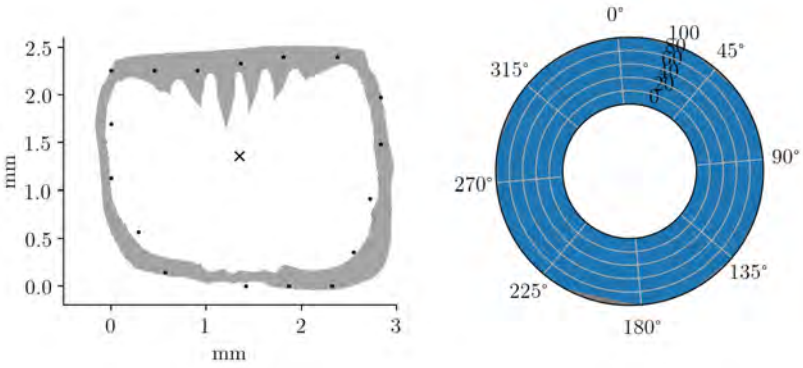

Figure 4.8: *A figure in two parts, which shows the thickness of the inner layer using data on cortical holes. A mosaic of CT scans is shown on the left with a black dot on the centre of 17 SRCT scans (n=17) taken from 70% shaft length. A polar graph on the right shows the thickness using data extracted from two-dimensional histograms as presented above. Blue indicates that fibres are axially oriented.*

is very small this observation should be considered cautiously. In the third bird, the outer layer is observed at all locations at 30% length, with an average thickness of 27.3%. The presence of the outer layer at 30% in replicate feathers also supports the proposal of a superior umbilical region but there is clearly a need for further work.

Data on the thickness of the longitudinal layer from all three feathers at 10% and 30% shaft length is presented in Table 4.1.

In all three birds, no outer layer is observed at a shaft length greater than 30%.

4.2.2 Layer Orientation

Figures 4.13–4.17 show how the distribution of angle data from the inner layer changes around the cortex of the feather shaft. In each length-wise section there is a small amount of deviation from the global mean but no pattern was observed around the feather. This suggests that a layer can be treated as a single unit

Table 4.1: *A table to show the relative thicknesses of layers in the calami of three replicate feathers. The error in each value in the table is half the width of one bin in the two-dimensional histograms used to place the delimitation. The number of bins scales with the number of cortical holes present, but is never less than 30, which corresponds to an error of 1.5%. The overall error in the averages is estimated from the largest difference between each value and the average.*

Position	Bird 1		Bird 2		Bird 3	
	10	30	10	30	10	30
			Length (%)			
Dorsal	66.7	100	83.8	100	80	79.1
Leading	65.5	100	77.6	83.3	76.7	71.8
Ventral	79.3	100	81.9	84.3	65.4	83.3
Trailing	77.1	100	85.7	96.4	80	68.7
Average	72.15 ±7	100 ±0	82.3 ±5	91.0 ±8	75.5 ±10	72.7 ±11

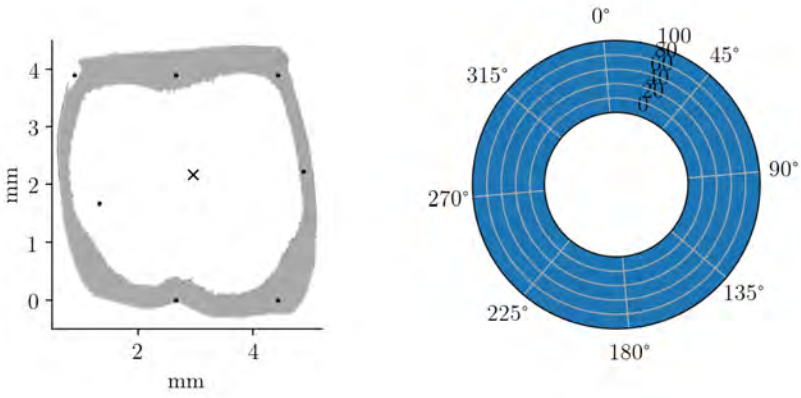

Figure 4.9: *A figure in two parts, which shows the thickness of the inner layer using data on cortical holes. A mosaic of CT scans is shown on the left with a black dot on the centre of 7 SRCT scans (n=7) taken from 90% shaft length. A polar graph on the right shows the thickness using data extracted from two-dimensional histograms as presented above. Blue indicates that fibres are axially oriented.*

and data from all scans can be summed. Figures 4.18–4.22 then show hole distributions with average values and two-dimensional histograms to show this data with percentage distance. Figure 4.18 is interesting because it shows a shadow at 90°next to the inner cortical edge, which is due to small or spherical holes being assigned an orientation. This is also the reason some counts can be seen at 0°in the outside layer, and accounts for the large spreads in box and whisker plot presented as Figure 4.13. Figures 4.19–4.21 show very clearly that there is only a single layer oriented at 0°in the rachis and Figure 4.22 shows the same but with noisier data which is caused by smaller counts, because the sample itself is smaller and contains fewer holes. The spherical hole artefact is also more prominent here where there are fewer holes.

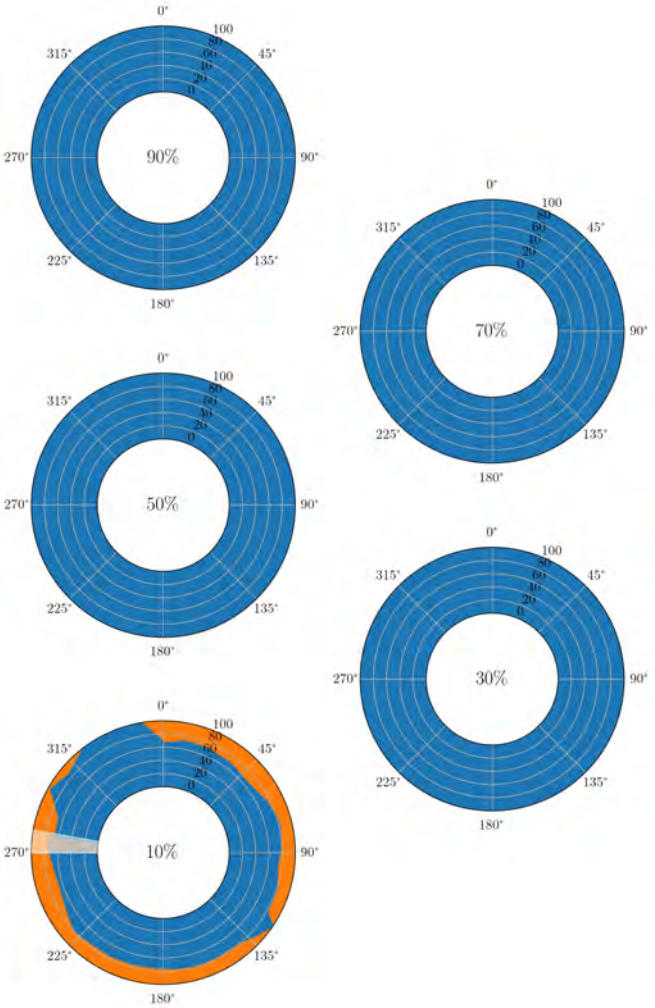

Figure 4.10: *Polar graphs which shows the thickness of the inner and outer layers of the first primary (P1) at five length-wise places using data on cortical holes. The length-wise position (% of total shaft length) of each polar cortex diagram is indicated in the centre of each graph. At 30% shaft length a typical thickness is ≈0.3 mm, and at 90% shaft-length this decreases to ≈0.1 mm. Blue indicates the inner layer in which fibres are axially oriented. Orange indicates the outer layer, in which the fibres are radially oriented. The length-wise position (% of total shaft length) is shown in the centre of each schematic.*

Figure 4.11: *Polar graphs which shows the thickness of the inner and outer layers of the first primary (P1) at five length-wise places using data on cortical holes on a replicate feather. Blue indicates the inner layer in which fibres are axially oriented. Orange indicates the outer layer, in which the fibres are radially oriented. The length-wise position (% of total shaft length) is shown in the centre of each schematic. Transparency indicates missing data.*

Figure 4.12: *Polar graphs which shows the thickness of the inner and outer layers of the first primary (P1) at five length-wise places using data on cortical holes on a second replicate feather. Blue indicates the inner layer in which fibres are axially oriented. Orange indicates the outer layer, in which the fibres are radially oriented. The length-wise position (% of total shaft length) is shown in the centre of each schematic. Transparency indicates missing data.*

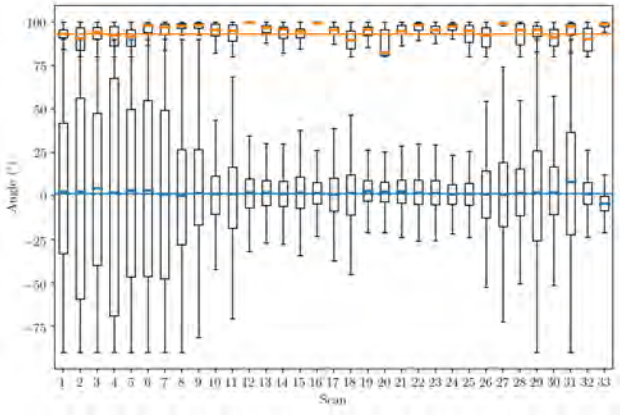

Figure 4.13: *A box and whiskers plot which shows angle data from each scan around the cortex from the 10% section and shows uniform orientation. Each scan is one point from Figure 4.5, and there is one box for each layer. The lines shown in each box are means, and the overlying line is the larger mean from a fitted double Gaussian distribution.*
Some of the whiskers are not visible within the axis range. This is a feature of the method and is caused by background noise.

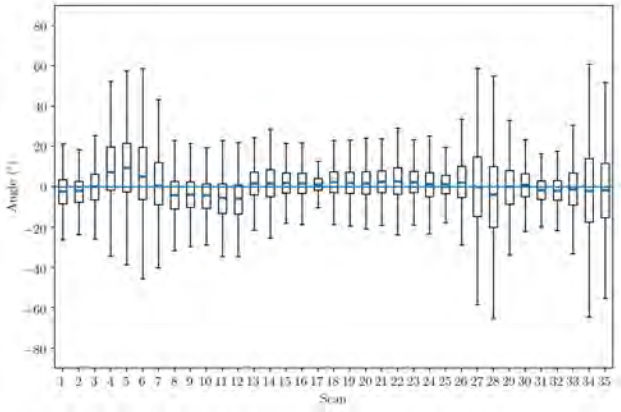

Figure 4.14: *A box and whiskers plot which shows angle data from each scan around the cortex from the 30% section and shows uniform orientation. Each box is one point from Figure 4.6. The lines shown in each box are means, and the overlying line is the larger mean from a fitted double Gaussian distribution.*

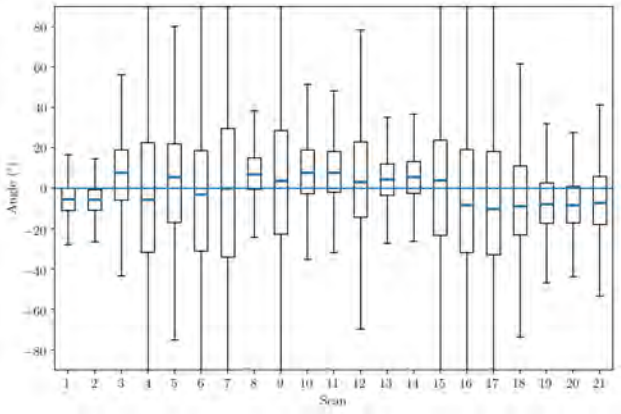

Figure 4.15: *A box and whiskers plot which shows angle data from each scan around the cortex from the 50% section and shows uniform orientation. Each box is one point from Figure 4.7. The lines shown in each box are means, and the overlying line is the larger mean from a fitted double Gaussian distribution.*

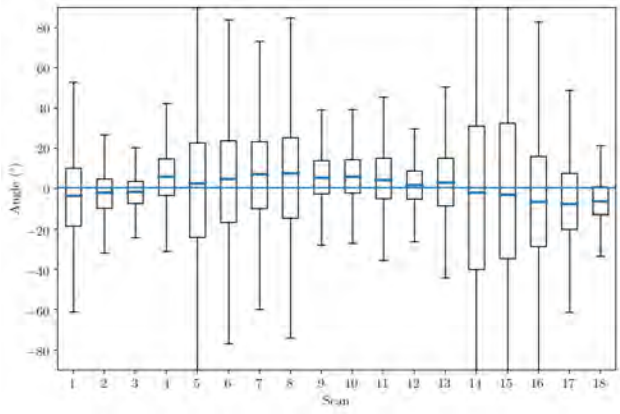

Figure 4.16: *A box and whiskers plot which shows angle data from each scan around the cortex from the 70% section and shows uniform orientation. Each box is one point from Figure 4.8. The lines shown in each box are means, and the overlying line is the larger mean from a fitted double Gaussian distribution.*

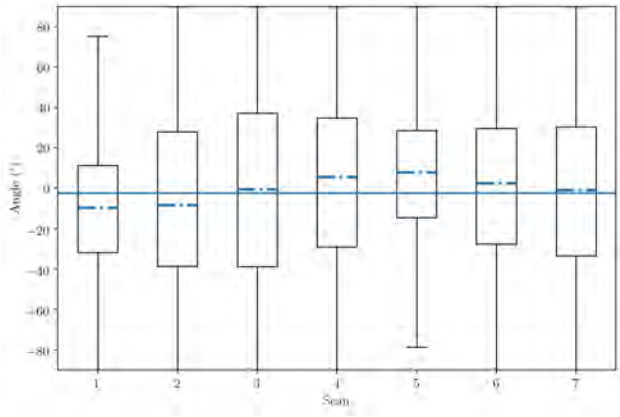

Figure 4.17: *A box and whiskers plot which shows angle data from each scan around the cortex from the 90% section and shows uniform orientation. Each box is one point from Figure 4.9. The lines shown in each box are means, and the overlying line is the larger mean from a fitted double Gaussian distribution.*

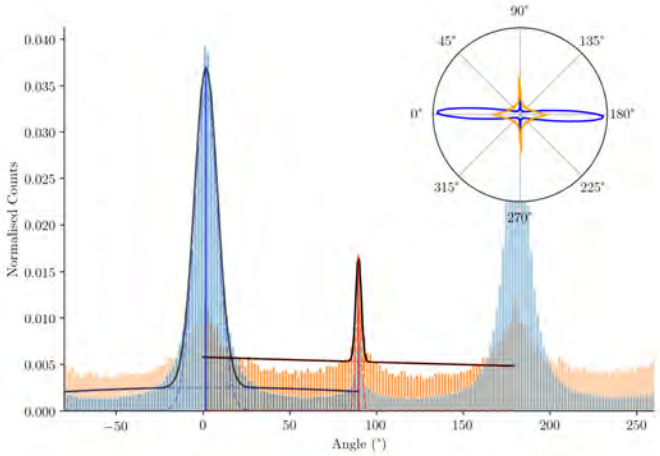

(a)

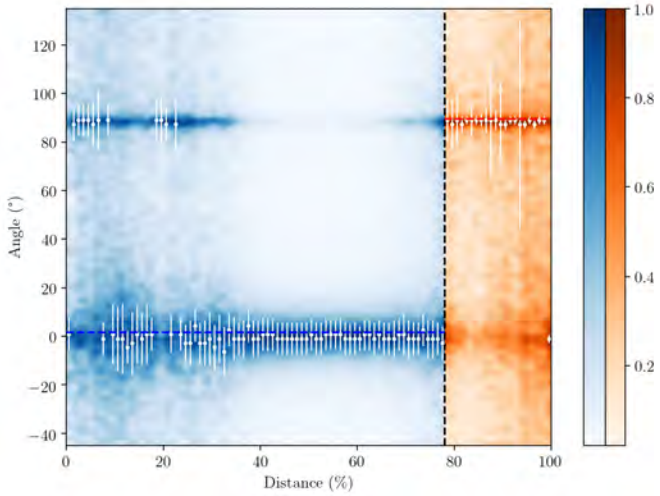

(b)

Figure 4.18: *Figure* ***a)*** *shows a histogram of concatenated angle data taken from 33 scans around the shaft cortex taken at 10% length from the base of the calamus. Data is presented in 100 bins of 1.8°, which have been normalised and a double Gaussian distribution is fitted to each layer. The inner layer is coloured blue and represents longitudinally oriented fibres. The outer layer contains radially oriented fibres and is coloured orange. Figure* ***b)*** *shows a 2-dimensional histogram. The data has been normalised by the peak in each vertical bin, and each layer used a different colour map. Two layers are seen. Although it appears there are 2 layers this is likely an artefact due to low count.*

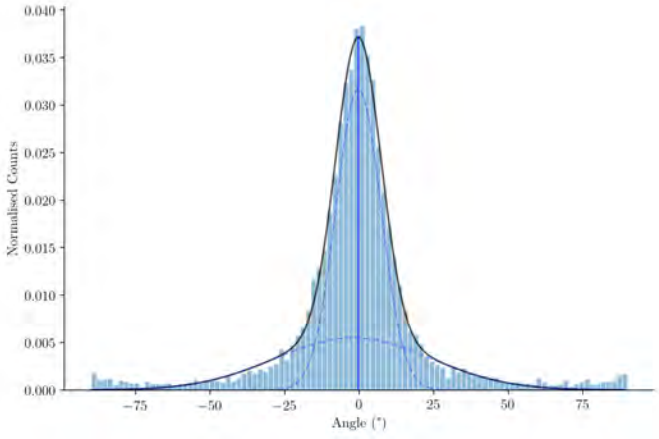

(a)

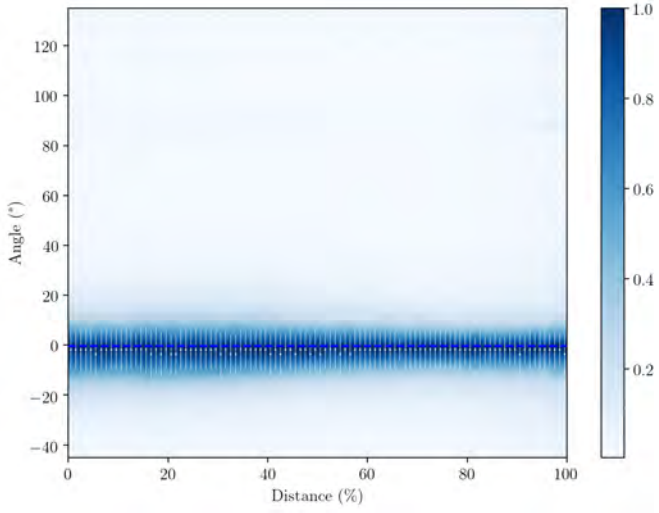

(b)

Figure 4.19: *Figure* ***a)*** *shows a histogram of concatenated angle data taken from 35 scans around the shaft cortex taken at 30% length from the base of the calamus. Data is presented in 100 bins of 1.8°, which have been normalised and a double Gaussian distribution is fitted to each layer. The inner layer is coloured blue and represents longitudinally oriented fibres. The outer layer contains radially oriented fibres and is coloured orange. Figure* ***b)*** *shows a 2-dimensional histogram. The data has been normalised by the peak in each vertical bin, and each layer used a different colour map. Only one layer is seen.*

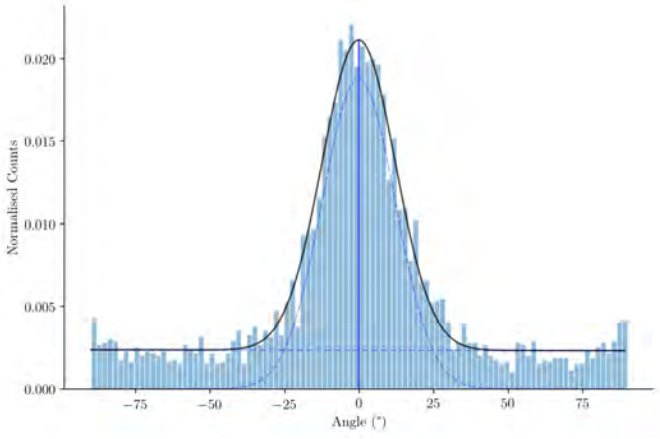

(a)

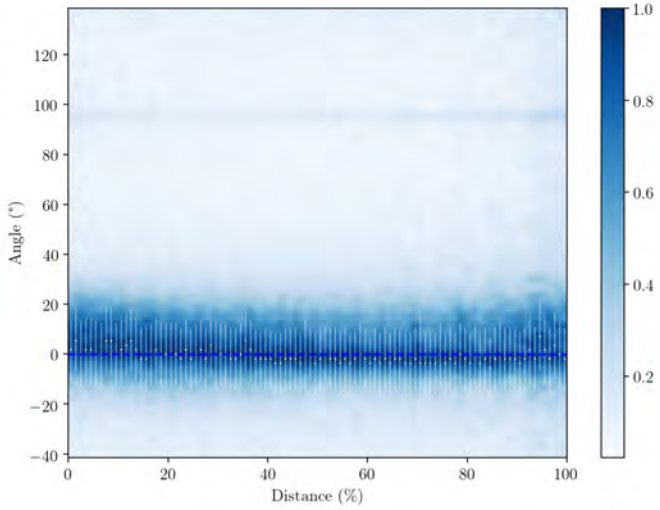

(b)

Figure 4.20: *Figure* ***a)*** *shows a histogram of concatenated angle data taken from 22 scans around the shaft cortex taken at 50% length from the base of the calamus. Data is presented in 100 bins of 1.8°, which have been normalised and a double Gaussian distribution is fitted to each layer. The inner layer is coloured blue and represents longitudinally oriented fibres. The outer layer contains radially oriented fibres and is coloured orange. Figure* ***b)*** *shows a 2-dimensional histogram. The data has been normalised by the peak in each vertical bin, and each layer used a different colour map.*

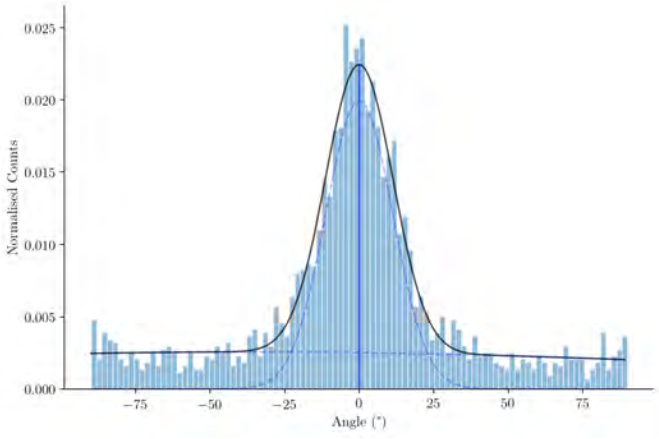

(a)

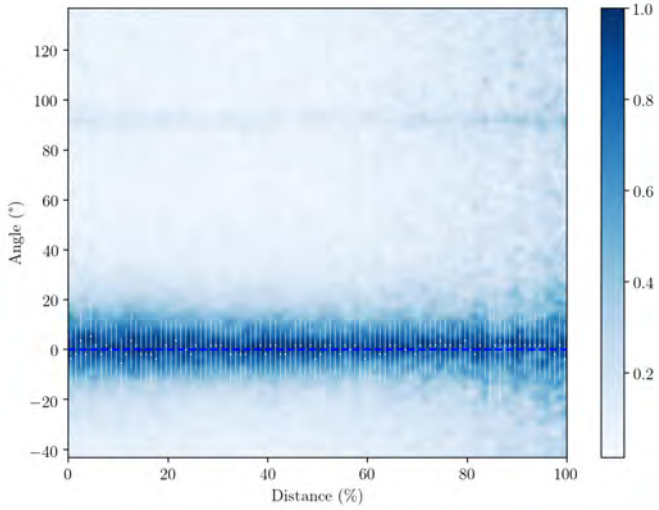

(b)

Figure 4.21: *Figure **a)** shows a histogram of concatenated angle data taken from 17 scans around the shaft cortex taken at 70% length from the base of the calamus. Data is presented in 100 bins of 1.8°, which have been normalised and a double Gaussian distribution is fitted to each layer. The inner layer is coloured blue and represents longitudinally oriented fibres. The outer layer contains radially oriented fibres and is coloured orange. Figure **b)** shows a 2-dimensional histogram. The data has been normalised by the peak in each vertical bin, and each layer used a different colour map.*

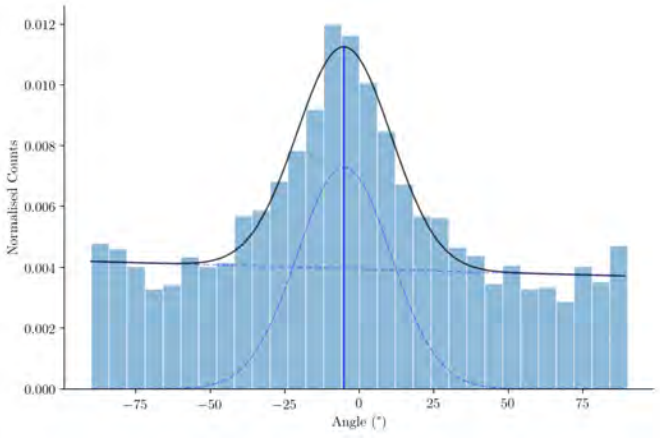

(a)

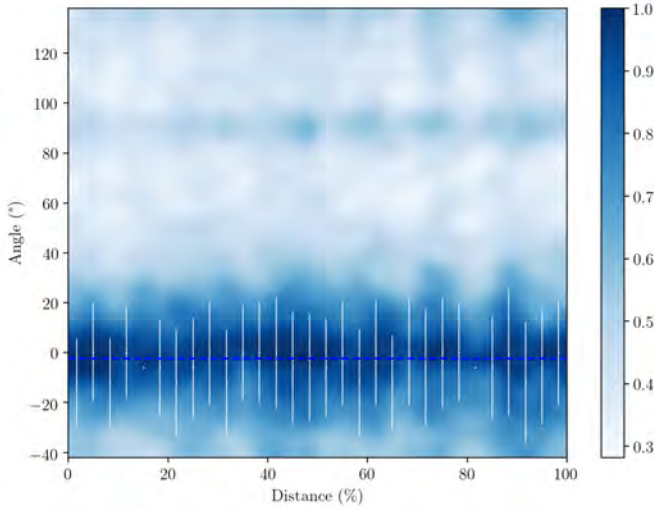

(b)

Figure 4.22: *Figure* ***a)*** *shows a histogram of concatenated angle data taken from 7 scans around the shaft cortex taken at 90% length from the base of the calamus. Data is presented in 100 bins of 1.8°, which have been normalised and a double Gaussian distribution is fitted to each layer. The inner layer is coloured blue and represents longitudinally oriented fibres. The outer layer contains radially oriented fibres and is coloured orange. Figure* ***b)*** *shows a 2-dimensional histogram. The data has been normalised by the peak in each vertical bin, and each layer used a different colour map.*

Table 4.2: *A table to show the orientation of layers in all feathers scanned. Data taken from the same length-wise sections have been concatenated and standard deviations are presented as confidence limits. Values quoted in the table are angles in degrees.*
∗Not enough holes to determine orientation
∗∗Outer layer no observed.

	Outer	Inner	Outer	Inner			
Bird	10	10	30	30	50	70	90
				% length from base of calamus			
Bird 1	87.73 ±3.25	1.27 ±7.03	∗∗	-0.07 ±7.54	-1.34 ±13.2	-0.38 ±-10.96	-1.44 ±0.37
Bird 2	*	1.65 ±6.86	∗∗	3.08 ±8.11	2.73 ±14.74	2.52 ±9.12	3.32 ±17.31
Bird 3	*	-0.62 ±7.20	89.97 ±11.65	-0.07 ±7.54	-1.65 ±14.36	-0.34 ±5.46	-2.03 ±13.7

4.3 Hole frequency

In the course of processing the data recorded in this work, it was revealed that the outer part of the cortex contained fewer holes, whether there was one layer or two.

This might simply be because there were fewer holes in the outer layer, or because the filtering protocol was less appropriate for the holes in this region. Figure 4.23 shows histograms of the number of holes for two datasets which demonstrate how a small number of holes can mislead an observer into thinking layers were present or absent due to a lack of data.

To check the observed decrease in the number of holes, histograms were normalised by the peak in each distance bin and by the average of the whole distance bin. This would reveal any signal that was being obscured by larger counts in the inner layer, which sometimes revealed that a scan which looked like two layers was in fact only one layer.

This step proves to be very important, because the smaller number of holes towards the outer edge of the cortex can be obscured by the larger counts in bins in the middle and close to the inside edge. In datasets where only one layer is present, it can appear that there are two layers, simply due to hole counts; this effect is shown in Figure 4.23. This dataset is a good example because the recorded data might suggest two layers, but normalising the data confirms that there is only one. In most cases where an outer layer is observed, the directional data of the outer layer was also obscured by larger counts in the inner layer. The position of the layer boundary was also usually underestimated.

Some example count data is presented in Figure 4.24. Nearly all tomograms show that there are many more holes in the outer part of the inner cortical layer, and frequency of holes decreases towards the inner cortical surface. Though a texture can be seen in the outer layer it is much more difficult to discern similar holes in the outer layer by eye, even after filtering and attempts at segmentation. This raises a question about why the holes are there

to begin with. Three explanations seem possible.

The first is that the holes are not a feature of feather keratin construction. Rather, that they are the result of mechanical wear. Where there is an outer layer, this explanation makes sense in the context of the parallel axis theorem, which would show that strain increases along the radius of a bend in a feather deformed under a bending load. However, this explanation does not explain why there are fewer holes in the outermost part of the shaft when there is only one layer. *Lingham-Soliar* (2015) considers high work of fracture, ability to resist many loading cycles, crack resistance and possibly vibration dampening as selective pressures. Of these, only vibration dampening may explain the presence of cortical holes. Some fatigue experiments with a piece of feather could observe whether holes and flaws are generated. If so, a section could be fatigued or damaged to generate holes which could then be used for studying the fibre alignment. This approach is sometimes used in the study of artificial composites and this work will be proposed in the Further Work section on page 176.

The second is that the holes are actively formed in the developing feather. These holes have not been the subject of any cellular work thus far and correspondence with one of the leading authorities on feather morphogenesis (*Maderson et al.*, 2009) has not resulted in any sensible hypotheses.

The third and most simple explanation is that there is no functional explanation.

4.4 Supporting optical work

Some further optical microscopy was performed on cross-sections embedded in resin and polished in preparation for spectroscopic work, shown in Figure 3.11 on page 58. These included the first, third and fifth primaries of the right hand wing (P1, P3, and P5) from all three swans.

These optical micrographs, when considered in the context of the CT scans already presented, also suggest that the calamus—

rachis delimitation according to most workers is not the same as the multi-layered—single-layered delimitation, and could be considered to occur in the superior umbilical region suggested by *Maderson et al.* (2009). Optical micrographs were taken from the same feathers, though not in the same length-wise positions, to complement the CT data, see Figure 3.11.

Figure 4.25 shows that while very little information can be seen in terms of fibre alignment, layers are clearly seen in the proximal shaft. Table 4.3 shows the thickness of the inner layer in all feather samples, including from feathers P3 and P5 of the three swans. This table expands on the CT data set and reinforces it. It can be seen that the outer layer, when present, can be up to 44% of the cortical width.

Table 4.4 shows optical data which corresponds to CT data already presented. The data show good agreement between the thickness calculated by the CT data and the thickness calculated from optical micrographs. It is unfortunate that the CT datasets and the optical datasets do not overlap. It would not have been possible to CT scan, embed in resin for optical microscopy, prepare for Raman spectra and tensile test every sample due to the different preparation methods required. Both tables show that the results of CT scanning which show the thicknesses of the layers and the orientation are approximately correct and tentatively suggest there is no obvious change on choosing a more distal primary.

Table 4.3 shows that two layers were usually visible in the calamus, but not in the rachis.

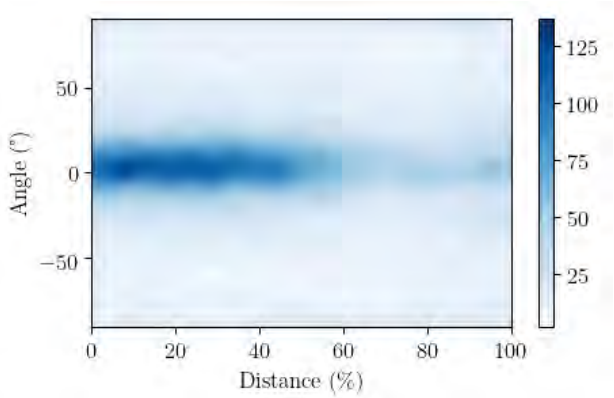

(a) *Not normalised*

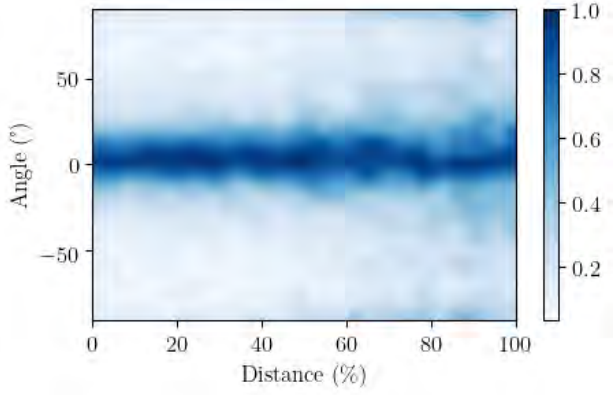

(b) *Normalised by peak in distance bin*

Figure 4.23: *Two histograms present the same CT data, but are normalised using different methods. The data set was chosen to illustrate that missing data might lead to the conclusion that there are two layers.*

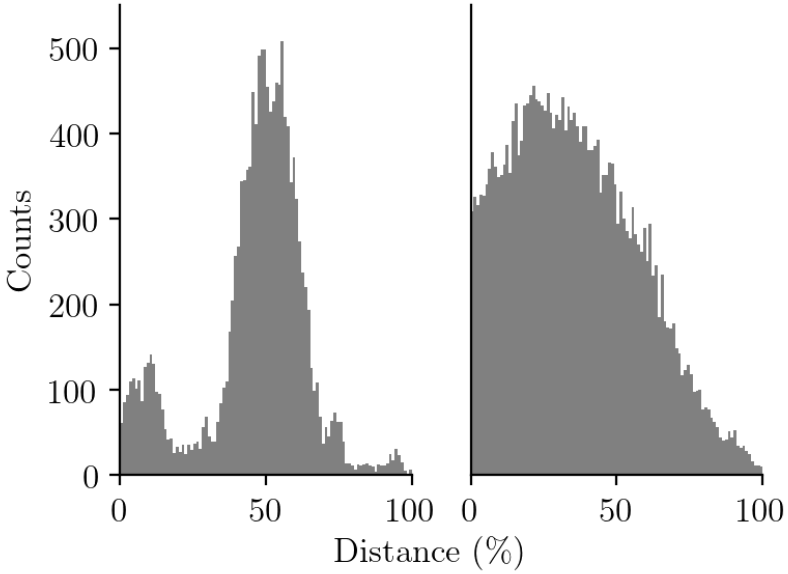

Figure 4.24: *Two histograms show how the distribution of cortical holes in two datasets of a swan feather. These distributions mean it is important to normalise the data by the maximum in each bin, else it is easy to place the boundary of the two in the wrong place. The data sets presented were chosen to illustrate this particular point and observed with edited parameters in the BoneJ program. They are not presented elsewhere in the results section*

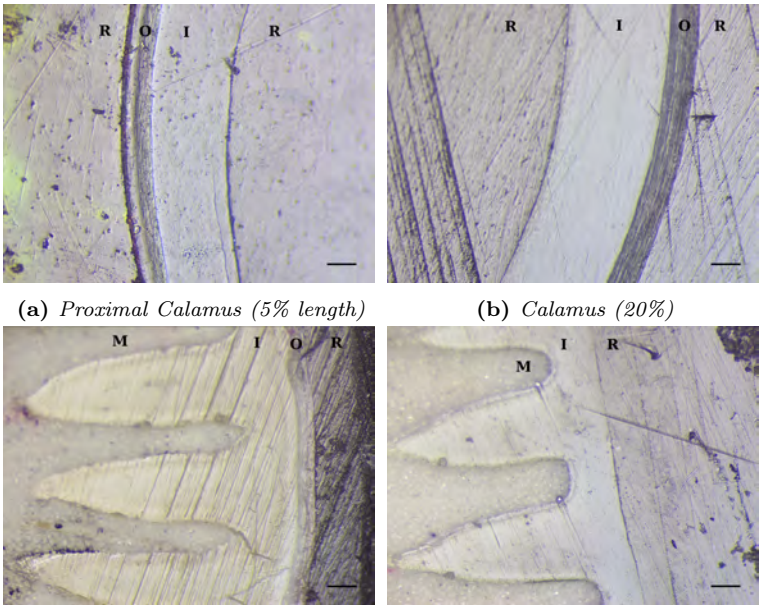

(a) *Proximal Calamus (5% length)*

(b) *Calamus (20%)*

(c) *Discontinuity (40%)*

(d) *Rachis (60%)*

Figure 4.25: *Four optical micrographs (20×) magnification which show the thickness of layers at four places along the rachis. length-wise position is measured from the tip of the calamus. R,O,I and M indicate Resin, Outer layer, Inner layer and medulla, respectively.*
Scale bars 0.1 mm

Table 4.3: *A table to show how layer thickness varies along the shaft as seen from optical micrographs of cross sections from three replicate birds.*
Values quoted are percentage widths.
∗indicates no data, because the sample had been destroyed in other experiments.
Brackets indicate an alternative measurement, which includes the full length of the dorsal ridges.

Length (%)	Position	Bird 1			Bird 2			Bird 3		
		P1	P3	P5	P1	P3	P5	P1	P3	P5
5	D	∗	78	68	79	84	73	∗	∗	∗
	V	∗	70	53	72	82	66	∗	∗	73
20	D	81	79	76	86	74	71	76	78	∗
	V	73	76	71	71	100	77	78	100	78
40	D	∗	77 (91)	100	100	100	100	76 (93)	76 (93)	83 (95)
	V	100	100	100	100	100	100	100	100	100
60	D	100	100	100	100	100	100	100	100	100
	V	100	100	100	100	100	100	100	100	100
80	D	100	100	100	100	100	100	100	100	100
	V	100	100	100	100	100	100	100	100	100

Table 4.4: *A table to compare observations made from SRCT dataset with optical micrographs. Unfortunately a direct comparison is not possible due to staggering the techniques. No major changes are observable.*
∗Data not collected.
O = optical, CT = Synchrotron Radiation Computed Tomography
D = Dorsal, V = Ventral.

	Position	5	10	20	30	40
			Distance (%)			
P1		O	CT	O	CT	O
Bird 1	D	∗	66	81	100	100
	V	∗	79	73	100	100
Bird2	D	79	84	86	83	100
	V	72	81	71	97	100
Bird 3	D	∗	80	76	79	76
	V	∗	65	78	68	100

4.5 Reinterpretation of earlier work

Now that the method has been applied to the SRCT data for which it was designed, it is time to see whether it can be used on previous data. The data, which inspired this project, was presented by *Laurent et al.* (2014). The layup was not the main subject of the paper, it was the presence of layers. The tomograms there were presented only to support some nanoindentation results and their interpretation was descriptive. The thicknesses of the three hypothesised layers—quantified from the tomogram (presented in this thesis as Figure 2.3) shows layers to be 25, 50 and 25% on going from the inner cortical edge to the outer cortical edge. The orientation of these layers were reported as -5, 0 and +45°, respectively. However, this was based on qualitative observation. On reprocessing that data, the methods from this work reveal that the first two layers are in fact one layer, and one is mislead into

thinking that there are two layers of differently oriented fibres due to a change in the frequency of cortical holes. The software measures the layer to be 76.3% of the cortical thickness and oriented at -6.71°. The standard deviation of the angle values for the entire inner layer is 8.9°. The double Gaussian approach cannot be used because the resolution of the scan is low, and fewer holes are resolved with low precision. The outer layer accounts for the rest of the thickness but too few holes are recorded to form a signal from which to calculate the orientation.

The band-pass filter in BoneJ will also treat holes at different resolutions differently and the uncertainty in the calculation of the major axis increases with voxel size. This data was reconstructed at 792 nm voxel resolution.

This over-interpretation of the CT scan suggests that it may have been possible to over-interpret the original nano-indentation results too (and with this knowledge is now seems likely that there were not three layers in the Partridge but only two, and it would suggest that there is not four but two layers in the Bald Eagle studied by *Laurent et al.* (2014). However, in the case of the Bald Eagle is it not that the two outer layers in the original interpretation are in fact one (see Figure B3b(top) on page A10), or even that the outermost layer might have been an indentation on the resin, but it may have been that the two innermost layers are one layer, the two outermost layers are indeed two layers and in fact there is one more layer which had been missed. Now that it has become clear that the layers seen in optical micrographs do correspond to changes in orientation, it looks as though this might be the case. Figure 4.27 shows that there are 4 layers, an inner layer of approximately 70% and then three outer layers of decreasing thickness.

None of the micrographs of the feathers used in the present work show two or three outer layers, and *Lingham-Soliar* (2015) has acknowledged there may sometimes be two layers, but never three or even four.

"We have known for some time that the fibrous struc-

> ture of the rachis cortex is anisotropic—microfibers predominantly longitudinally oriented and a thin layer or two circumferentially oriented."

'Thin' presumably means *Lingham-Soliar* (2015) has not seen any layers approaching 50% thickness either. It is unfortunate that feathers with more than one outer layer did not appear in this work. However, given their small thickness it might have been the case that holes would not have been present in sufficient number or size to measure orientation. It was not previously clear whether the layers seen in optical micrographs perfectly corresponded to layers of differently oriented fibres but that now seems to be the case and therefore the layers which can be seen in Figure 4.27 suggest that there is more work to be done in investigating variation in layup across different taxa.

4.6 Conclusion: rachis layup

Based on more than 150 CT datasets of the feather cortex from the first primary feather of three swans, there is now a more convincing body of evidence that the fibres of the inner cortical layer are aligned with the axis, that this is true around and along the feather, and that there is little within-layer variation of orientation.

The standard deviation of the orientation of the inner cortical layer in the samples investigated in this work is smaller than 15°. This number contains some methodological variance in an imperfect tilt-adjustment, and in voxel-discretisation, which means that this variance can be taken as an upper limit because the real variance is almost certainly smaller. X-ray diffraction work by *Cameron et al.* (2003) shows data with a standard deviation of approximately 5°. From there, this variance can be extrapolated to an effect on mechanical properties because E_1 transforms by multiplication with the square cosine of the rotation in degrees, $E_x = E_1 \times cos\theta^2$ (*Daniel and Ishai*, 2006). Therefore a component of a confidence limit can be calculated for future modelling and finite element experiments. For example, if $E_1 = 10$ GPa, then a

deviation of 5° would correspond to a new modulus $E_x = 9.2$ GPa, or an $\approx 8\%$ reduction in modulus. The real confidence limit would have to account for many more variables such as hydration.

This, of course, makes good functional sense and optical micrographs are now understood much better. It has been established that the outer layer is observable by optical microscopy, and that no observable outer layer in the rachis is not due to an inability to resolve it, which was suspected for a time. Approximate layer orientation has been confirmed and within-layer variation has been investigated such that less sampling is needed in future CT experiments. The stage is set for more meaningful optical studies, and there is now justification for sectioning a large number of feathers from different taxa. This was not the case four years ago when the literature on laminar geometry was much smaller and characterised by descriptive observations.

Finally, there is a single layer in the distal half of the rachis, with all fibres in axial alignment, in all rachises investigated so far. The method presented can measure orientation and the small deviations that may be present. Higher resolution scans are useful if the outer layer is important because holes are smaller and less frequent. Furthermore, it now seems quite certain that *Maderson et al.* (2009)'s zone of discontinuity, where the fibrous laminar structure reflects a changing functional role of the feather shaft is more appropriate than splitting the feather into the rachis and the calamus at the superior umbilicus or even where the vane attaches. Two questions have been raised, which are: Why do the holes exist at all? and Why are there no holes in the outer part of the cortex when there is only a single layer?

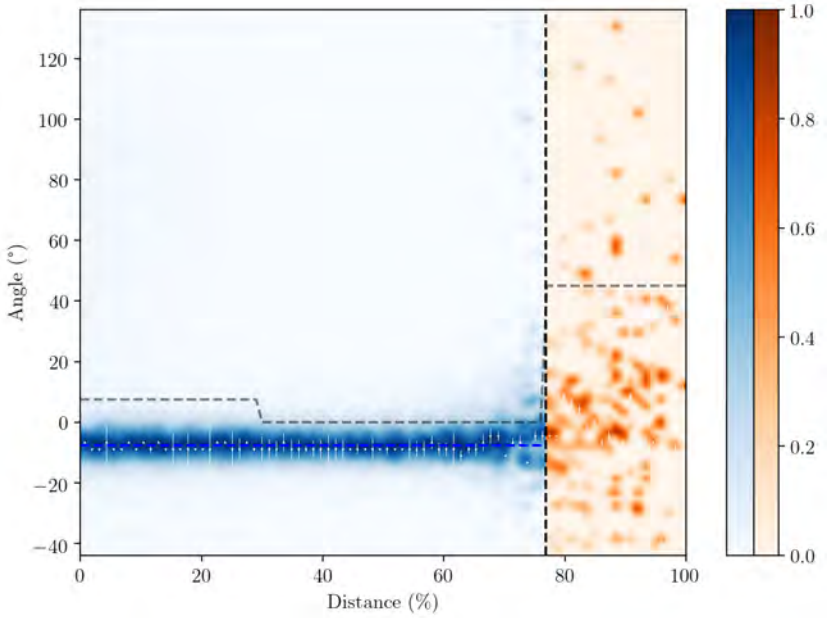

Figure 4.26: *The first CT data on fibre layup in the feather shaft cortex was presented by* Laurent et al. *(2014) to support some indentation data. Three layers were estimated and they were oriented at -5, 0 and +45˚on going from the inner edge of the cortex to the outer edge. The thicknesses of these layers were approximately 25, 50 and 25%, respectively. Their original claim is shown on this 2 dimensional histogram as a dashed line. The software approach presented in Chapter 3 was applied to this dataset and has shown that there are in fact only two layers. The inner layer is* $\approx 78\%$ *of the cortical width and oriented longitudinally. The outer layer did not contain enough holes to extract a value for orientation.*

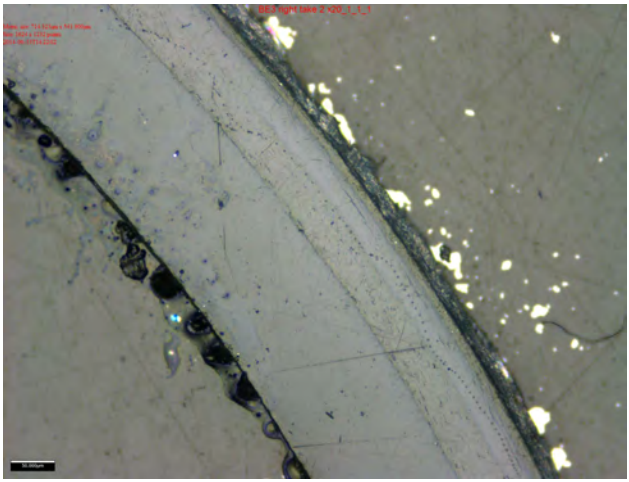

Figure 4.27: *An optical micrograph showing a piece of feather that was used for some nanoindentation work reported by* Laurent et al. *(2014), which shows that there may be as many as four layers in the calamus of primary feathers. This feather is the third primary of the Bald Eagle, sectioned at 30% shaft length.*

Chapter 5

Visualising what cannot be seen

Investigating protein chemistry with Raman spectroscopy

Chapter 2 introduced the concept of protein structure and the importance of understanding secondary structures. Chapter 3 outlined different regions of the vibrational spectrum and the molecular signatures seen in those regions, before example spectra were presented from the Amide I and Amide III regions. Band assignments for all regions to be investigated were presented from the literature and spectra for the Amide I and Amide III regions were both fitted with six Gaussian bands. Those bands contain information about polypeptide side chain residues, α -helix β -sheet and β -turn structures. An example of a fitted spectrum S-S region was also presented, which was fitted with three bands which contain information on the conformation of the S-S bond in cystine residues.

The results presented in this chapter have recently been published in the Journal of Structural Biology (*Laurent et al.*, 2020) and compare band intensities from within the Amide I and Amide III spectral regions. Ratios are used because it is unfair to compare

band areas taken with different experimental parameters. Though the settings used in the spectrometer may have been the same, this method is sensitive to non-flat surfaces, manual focus of the microscope and temperature and so spectra should be treated as though they were recorded using slightly different experimental parameters. It is also not appropriate to compare Gaussian components which have different half-widths.

In order to investigate possible differences in protein secondary structure between the inner and outer regions of the cortices of the shaft samples, band intensity ratios were measured in the Amide I, Amide III and disulphide bond (S-S) regions for the four selected birds. For the Amide I region (1560–1800 cm^{-1}), the six-band fitting method used followed the fits carried out by other groups in this spectral region (Cai and Singh, 1999, Hahn, 2015, Khosa et al., 2013, Church et al., 2010, Zhang et al., 2012, Essendoubi et al., 2019, Akhtar and Edwards, 1997, Blanch et al., 2003). This method gave a good fit to the experimental spectra (Figure 3.13 on page 63). The recommended assignments, which are presented in Table 2 (column 6), were made based on a review of the assignments made in relevant recent literature (Hahn, 2015, Zhang et al., 2012, Akhtar and Edwards, 1997, Maiti et al., 2004). The six fitted bands in the Amide III region (1200–1350 cm^{-1}) (Figure 3.14 on page 64) and the three fitted bands in the S-S (400–600 cm^{-1}) (Figure 3.15 on page 65) were assigned in the same way, see Table 3 (column 5) and Table 4 (column 5) respectively.

Figure 5.1 shows an example of band intensity ratios obtained in the Amide I region for a Gull, Kestrel, Mallard and Swan for samples cut at 40% length. It shows the intensity ratios for the bands at 1668 $cm^{-1}$and 1613 cm^{-1}, which are β -sheet and side-chain bands respectively. For this figure, values for feathers from the left (L) and right (R) wings of the same bird are shown. This is indicated in the figure by the characters 'L' and 'R'. The ratio decreases for all four birds on going from the inner to the outer region. Figure 5.2 shows an example of band intensity ratios obtained in the Amide III region for these Gull, Kestrel, Mallard, and Swan

samples. It shows the band intensity ratios for the bands at 1262 $cm^{-1}$and 1240 cm^{-1}, which are random coil and β -sheet bands respectively. It can be seen that the experimental errors are greater in Figure 5.2 than Figure 5.1, and as a result, no clear trend can be seen in Figure 5.2, although based on the trend seen in Figure 5.1 an increase in the band intensity ratio 1262 cm^{-1}: 1240 cm^{-1}(random coil:β -sheet) might have been expected on going from the inner to the outer region.

A Raman spectrum in the S-S region recorded for the shaft of the left wing of a Mallard cut at 40% length is presented in Figure 3.15, on page 65. Three bands were fitted to this spectrum with band maxima of 525, 540 and 560 cm^{-1}, which correspond to two different conformations of a CC-S-S-CC unit in cystine groups (*Akhtar and Edwards*, 1997) (G-G-G and G-G-T) and an S-S stretch coupled with a cystine residue absorption respectively (*Akhtar and Edwards*, 1997). The ratio of the G-G-G conformation to the total disulphide bonds has been suggested as a criterion for the stability of disulphide groups in keratin (*Choe et al.*, 2017, *Essendoubi et al.*, 2019) and this would indicate that the band intensity ratio 510 cm^{-1}:525 cm^{-1}should decrease on going from the inner to the outer region. Unfortunately, no trend could be observed for this ratio on going from the inner to the outer region as the experimental errors are large.

As the signal-to-noise was better in the Amide I region than the Amide III and S-S regions, the experimental band intensity ratios in the Amide I region showed the lowest experimental errors compared to those in the other two regions (compare for example the experimental errors in Figure 5.1, Figure 5.2). As a result, most attention was given to band intensity ratios in the Amide I region to investigate possible differences in protein structure between the inner and outer regions. Inspection of the Amide I spectrum in Figure 3.13 shows that the bands at 1553 and 1585 cm^{-1}(assigned to ring modes) are much weaker than the other bands at 1613, 1640, 1668 and 1692 cm^{-1}. This was also found in all Amide I spectra recorded. Therefore, only the four more intense bands were used to

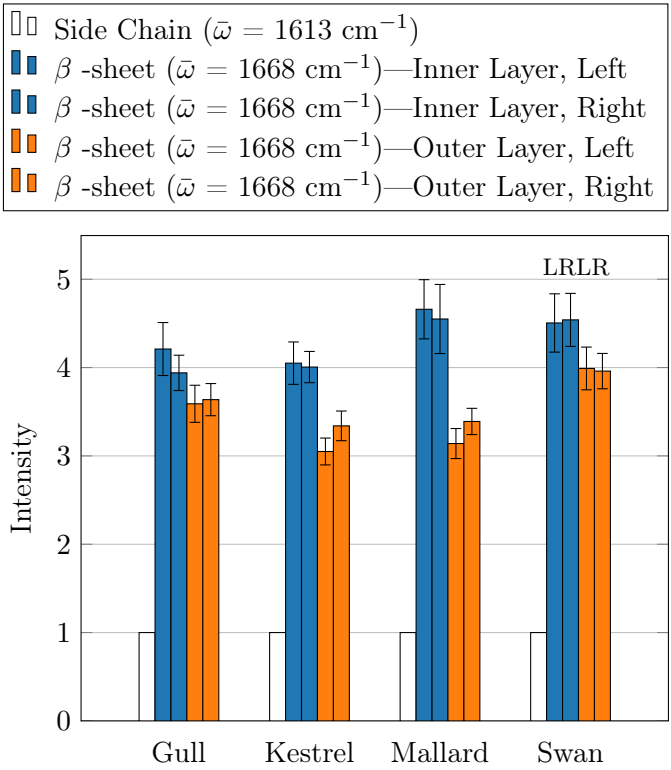

Figure 5.1: *Band intensity ratios in feathers from the Gull, Kestrel, Mallard, and Swan. The β -sheet is represented by a scattering at $\bar{\omega}$ = 1668 cm^{-1} and the side chain by scattering at $\bar{\omega}$ = 1613 cm^{-1}. These bands correspond to β -sheet and side-chain respectively. The side-chain contribution is set to 1. Values for feathers from the left (L) and right (R) wings of the same bird are shown, and the order is Inner L, then Inner R; Outer L, then Outer R. This is indicated in the graph by the characters 'L' and 'R'*

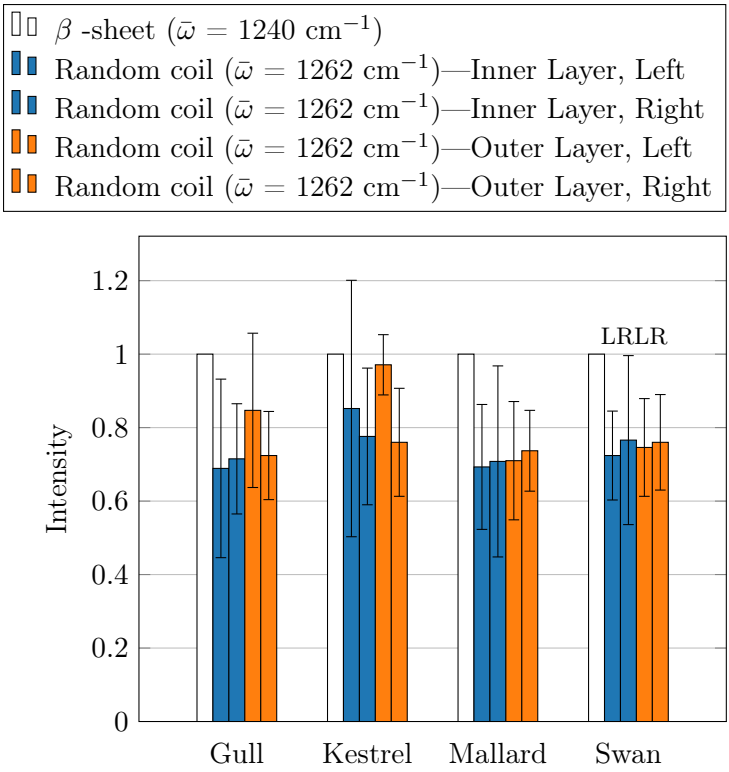

Figure 5.2: *Band intensity ratios 1262:1240 cm^{-1}in the Amide III region of feathers from a Gull, Kestrel, Mallard and Swan. These bands correspond to random coil and β -sheet respectively. The β -sheet contribution is set to 1. Values for feathers from the left (L) and right (R) wings of the same bird are shown, and the order is Inner L, then Inner R; Outer L, then Outer R. This is indicated in the graph by the characters 'L' and 'R'*

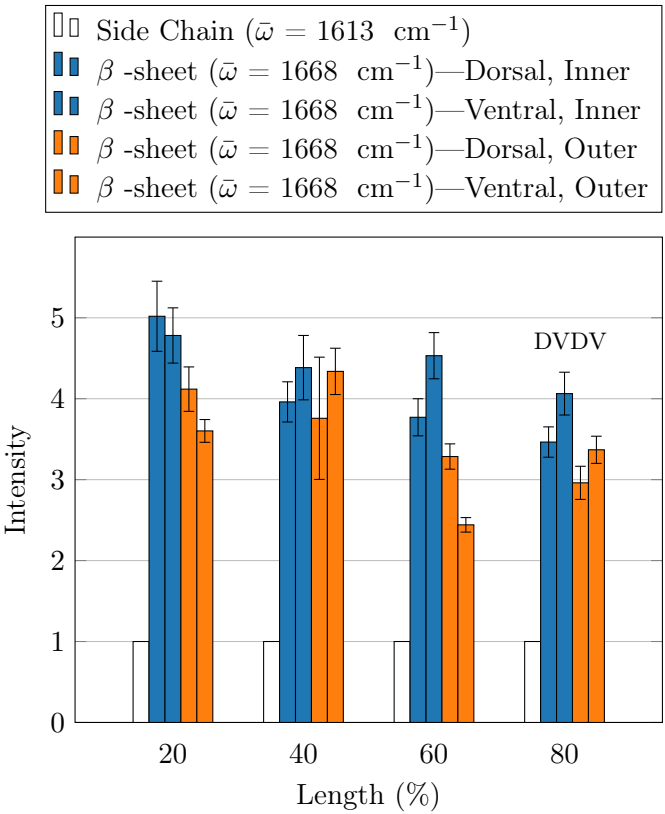

Figure 5.3: *Band intensity ratios 1668:1640 cm^{-1} in the Amide I region of feathers from a Swan. Spectra were taken from cross-sections of feathers at 20, 40, 60 and 80% length from the base of the calamus. The β -sheet is represented by a scattering at $\bar{\omega}$ = 1668 cm^{-1} and the side chain by scattering at $\bar{\omega}$ = 1613 cm^{-1}. Side Chain contribution is set to 1. Values for the dorsal and ventral of the same layer are shown, and the order is Inner Dorsal, then Inner Ventral; Outer Dorsal, then Outer Ventral. This is indicated in the graph by the characters 'D' and 'V'*

determine band intensity ratios, with the intensity of three bands being evaluated relative to the intensity of the 1613 cm^{-1}band i.e. the following ratios were evaluated: (a) 1668 cm^{-1}:1613 $cm^{-1}\beta$ -sheet : side chain, (b) 1640 cm^{-1}:1613 $cm^{-1}\alpha$-helix : side chain and (c) 1692 cm^{-1}:1613 $cm^{-1}\beta$ -turn : side-chain. Of these ratios, (a) which involves the β -sheet band at 1668 cm^{-1}might be expected to show the largest change if there is a change in protein structure between the inner and outer regions (*e.g.* an increase in β -sheet s from β -keratin) as β -keratin is known to provide more rigidity than α-keratin (*Alibardi and Toni*, 2006). This proved to be the case on going from the inner to the outer regions. Examples of the change of the ratio (a) are shown in Figure 5.1. These observed trends were the same for all four birds with all three ratios decreasing from the inner to the outer region. These results indicate that there is more β -sheet in the inner region, than the outer region of the cortex, relative to side-chain groups. There was no significant change in ratios (b) and (c) on going from the inner to the outer regions, taking into account experimental errors (see the SI section).

Although we have observed that the β -sheet component is larger in the inner region than the outer region, it is difficult to determine the reason for this in terms of change in keratin structure. An increase of β -keratin in the inner region, relative to the outer region, may reflect an increase in segment C in the inner region (caused by larger C segments in the different β -keratin s present and/or a greater β-content in the C segments in the same proteins (*Fraser and Parry*, 2019, 2014, *Parry et al.*, 2019). It might also be caused by different relative fractions of fibre: matrix in each region.

Band intensity ratios were also measured in the Amide I, Amide III and S-S regions for the outer regions of the shafts of the four birds studied in this work at the dorsal, ventral, trailing and leading positions at 40% of the rachis length from the base. Again particular attention was given to ratios measured in the Amide I region. For the bands (a)-(c) measured for these four positions,

no trend in the ratios (a) - (c) could be observed between these positions and, within experimental error, each ratio was the same in the four positions.

The Amide I band intensity ratios (a) - (c) were also investigated at different positions along the length of selected shaft samples from Swan feathers, at the dorsal and ventral positions. Spectra were taken from cross-sections of Swan shafts at 20, 40, 60, and 80% of the length from the base of the shaft at the dorsal and ventral positions. Nine feathers were investigated—three feathers (P1, P3 and P5) from the right wings of three Swans (*Cygnus spp.*). Figure 5.3 shows an example of results obtained for band intensity ratio. Inspection of all the results indicates that there is a decrease in ratio (a) on going from the inner to the outer regions, but there are no significant changes in these ratios along the length of a shaft or between the dorsal and ventral positions.

The observed change in ratio (a) from the inner to the outer region of a shaft apply to all four of the birds studied and could therefore represent the first report of a new neornithine synapomorphy as the trait is observed in a basal order Anseriformes (Swan, Mallard) as well the derived order Falconiformes (Kestrel), though more work would need to be done on other groups to confirm a neornithine synapomorphy. This would imply that bird feathers adapted to a selection pressure before the groups investigated in this paper, or perhaps all extant birds, diverged from the root of the avian phylogeny.

Conclusions

In this work, Raman spectra were recorded from the inner and outer regions of feather shaft cross-sections of four birds; Swan, Gull, Mallard and Kestrel. Spectra were obtained in the range 3200–100 $cm^{-1}$and were analysed in three regions; Amide I (1560–1800 cm^{-1}), Amide III (1200–1350 cm^{-1}) and S–S (400–600 cm^{-1}). For each sample investigated, the Amide I region showed the best signal–noise and information on the protein secondary structures in the inner and outer regions of the cortex were obtained from

these measurements. It was concluded that the β -sheet component is larger in the inner region than the outer region relative to the protein side chain components.

This trend was also observed along the length of a shaft, but no significant difference in this behaviour was observed at different distances from the base of the shaft or between dorsal or ventral positions. therefore, towards answering question 2 on page 2— Do the different reduced modulus values of the inner and outer cortical regions correlate with differences in the protein secondary structures within these regions?— It is concluded that differences in protein secondary structure between regions can be observed and they would contribute to the difference in properties of these regions. This is consistent with the proposal that E_r values observed by (*Laurent et al.*, 2014) are greater in the inner region than the outer region. It also makes sense in application for the load bearing inner region to be stiffer than the outer region which would prevent buckling. However, this investigation does not observe any differences in sections cut at different lengths along a shaft or between different feathers on the wing.

In summary, this work has shown that Raman spectroscopy can be used effectively to study the change in protein secondary structure of the inner and outer regions of a feather shaft. It is anticipated that with improvement of the technique and sample preparation methods that more detail will be derived concerning the protein secondary structures in these regions. It would certainly be advantageous if the Amide III region, as well as the S-S region, could be used with the Amide I region, with an internal standard band such as the side-chain band in the Amide I region to monitor changes of protein secondary structure.

From a biomimicry standpoint it would be interesting to consider how a composites engineer would design a structure for the same application. The author believes the structure would take approximately the same shape as the shaft in cross-section, but with a constant but tapering cross-section. The rachis would be made from unidirectional fibres and the dorsoventral thickening

composed from additional strips of unidirectional cloth. Whilst it might seem sensible from an evolutionary perspective to vary composition of the matrix or the fibres in different layers, from a manufacturing perspective it would be much simpler to adjust these properties by adjusting the thickness of layers possessing the same properties.

Chapter 6

Loading with an isotropic assumption

Tensile testing

Some useful structural and material properties have been measured and presented in Chapters 4 and 5. The lay-up and material variation within the layers are two pieces of the form-function puzzle, but they are not easily related without load-response data. In this chapter, tensile test data is presented from different parts of the feather shaft. It is presented with no special treatment first, and then reinterpreted using Classical Laminate Theory in Chapter 8.

6.1 Results

6.1.1 Tensile testing with an isotropic assumption

Figure 6.1 shows that if the laminate is considered a single piece of isotropic material, the elastic modulus varies between approximately 5 and 15 GPa. The colour indicates whether the sample was taken from the dorsal part or the ventral part of the feather shaft and some of the samples also show some curvature in the $\sigma : \varepsilon$ response. No grouping is apparent; if there was difference between

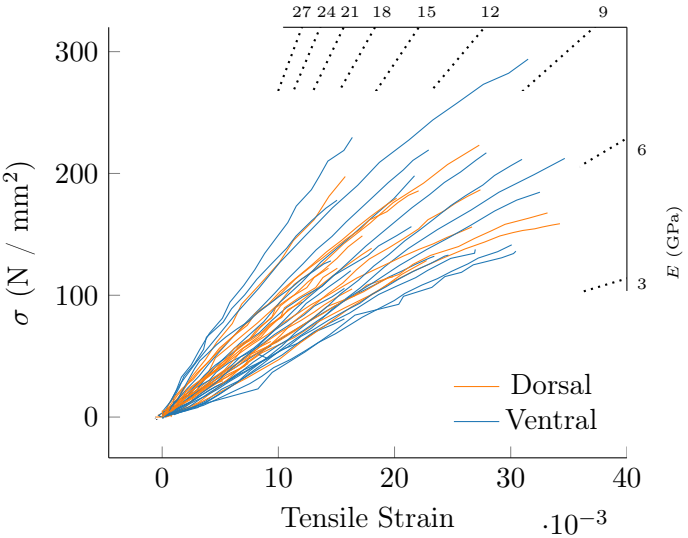

Figure 6.1: *A figure to show stress / strain curves for all tensile samples. Blue lines indicate that the sample is from the ventral position, and orange lines indicate the sample is from the dorsal position. The stiffest sample is ≈ 15 GPa and the most elastic sample is ≈ 5 GPa, most samples are between 5 and 9 GPa.*

the dorsal and ventral parts of the feather, the orange lines and the blue lines would group together.

Figure 6.2 shows the same data but plots the derivative of tensile stiffness $\frac{\delta\sigma}{\delta\varepsilon}$ by central differences, to approximate a straight line. Small strains only are presented to avoid issues rooted in non-uniformity, and colour again indicates whether the section was from the dorsal or ventral surface of the shaft. This graph reveals that the range of E observed was actually 5–10 GPa and not 5–15. This figure also shows no apparent grouping.

Figure 6.3 shows the same data with different colour mappings. Each subfigure deals with a different variable, individual, position on the wing, and position along the feather are all considered and these plots all present cross-sectional area using line thickness. Some groupings can be seen. In the first subfigure (a), Bird 3 seems

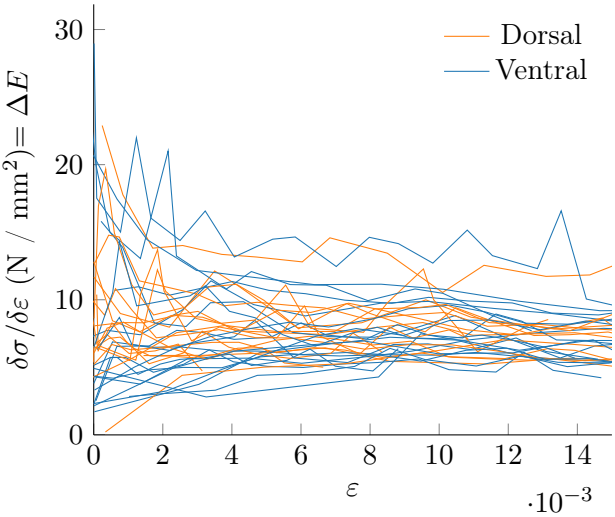

Figure 6.2: *This graph shows the stress and strain for all samples tested. It shows the same data presented in Figure 6.1, but presents $\delta\sigma/\delta\varepsilon$ instead of σ. Blue lines indicate that the sample is from the ventral position, and orange lines indicate the sample is from the dorsal position. The stiffest sample is $\approx$ 15 GPa and the least stiff sample is $\approx$ 5 GPa, though most samples are between 5 and 9 GPa.*

to have lower values and also a smaller standard deviation. In the second (b) tests from P5 also seem to be lower. In the third graph (c) no apparent groupings are visible.

6.1.2 Statistical analysis

One-way ANOVAs were performed using the Pingouin package for Python (*Vallat*, 2018). Results for tests between tensile test results $\frac{\delta\sigma}{\delta\varepsilon}$ of different groupings of the sample pieces are presented in Table 6.3 and post-hoc test results are presented in Table 6.4. The analysis is repeated within birds and is presented in Tables 6.5, 6.6 and 6.7.

Within sample

ANOVA results indicate that there is no significant difference between the dorsal and ventral positions but that there are differences between birds, feathers and lengthwise sections, based on variances.

Pairwise *post-hoc* tests which compare sample means suggest that the tensile behaviour of the *laminate* does not differ with respect to variance between Birds 1 and 2, between Feathers 2 (P3) and 3 (P5) or between Dorsal or Ventral pieces (at $p = 0.9$), but that Bird 3 is different from Birds 1 and 2 (the means of tensile test results from Birds 1,2 and 3 are 8.04, 8.48 and 6.69 GPa, respectively); feather P1 is different from feathers P3 and P5 (means of test results from P1, P3 and P5 are 8.3, 7.49 and 7.45 respectively) and also that there are multiple pairwise differences between lengthwise sections and they can be seen in Table 6.4.

Because the number of birds sampled is so small, it is difficult to explain the difference between them, although it is likely due to being a different species, being a different weight, or being a different sex. Unfortunately these attributes are not known.

Although feathers P3 and P5 are not significantly different at $\alpha = 0.1$, a trend is revealed in their means—that mean effective E seems to decrease with position on the wing and this deserves more investigation to see if the trend holds within each bird, see Table, 6.2.

As with the feather positions, the differences are seen between lengthwise sections reveal another trend— that the mean effective E seems to decrease with distance along the shaft, see Tables 6.1. Note also that the number of significant pairwise test results between sections becomes more convincing if the calamus (section 0–10% length) is not included. The lack of significant difference between the 10–30% section and the 30–50% section, and also between the 50–70% section and the 70–90% section indicate that the trend is weak because adjacent sections would not be statistically dissimilar.

Note that a larger sample was planned and it can be seen in

Table 6.1: *A table which shows that the average effective E decreases along the rachis (distally). Values presented to 3 d.p. (average values from nine swan feathers tested)*

0–10%	10–30%	30–50%	50–70%	70–90%
8.957	8.504	8.045	7.138	6.473

Table 6.2: *A table which shows that the average effective E decreases with feather position (towards the body of the bird). Values presented to 3 d.p.*

P1	P3	P5
8.307	7.497	7.450

Chapters 4 and 5 that this was intended to be the case, however due to a machine failure, data was not recorded for 20 pieces.

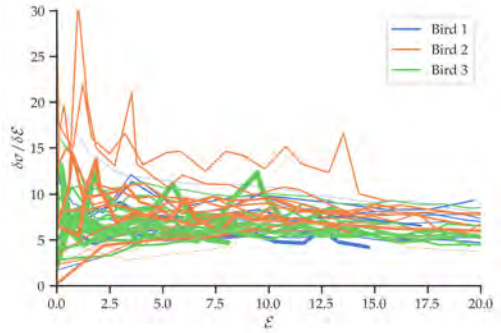

(a)

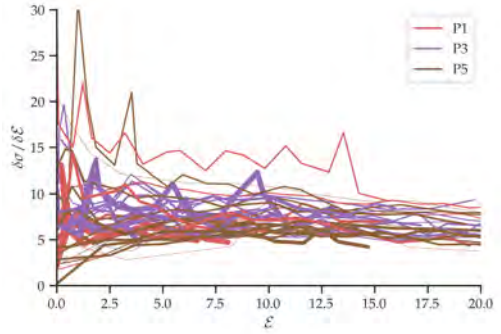

(b)

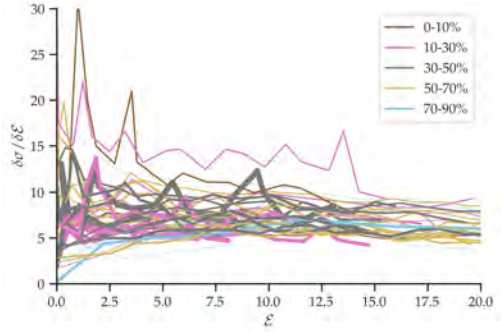

(c)

Figure 6.3: *This figure presents $\sigma : \varepsilon$ for all samples tested. In this figure, the data is coloured to present the data in three catgories. They are* ***(a)*** *grouped by bird,* ***(b)*** *grouped by feather and* ***(c)*** *grouped by section. In all graphs, the line thickness scales with cross-sectional area of the tensile piece because smaller areas should be associated with larger errors due to the way cross-sectional area was measured.*

Table 6.3: *One-way ANOVA results between different groupings of tensile test pieces. Degrees of freedom (sample size - 1) are presented for each test. n.b. *p < 0.1, **p < 0.01, ***p<0.001*

Source	ddof1	ddof2	F	p-unc	np^2	Result
sample	39	662	26.81	1.86e-110	0.61	Sig Diff ***
bird	2	699	21.20	1.16e-09	0.06	Sig Diff ***
feather	2	699	4.54	1.10e-02	0.01	Sig Diff *
position	1	700	1.80	1.80e-01	0.003	Not Sig Diff
section	4	697	9.33	2.37e-07	0.051	Sig Diff ***

Table 6.4: *Post-hoc Tukey test results following the ANOVA tests presented in Table 6.3 between different groupings of tensile test pieces. Post-hoc test results between samples are not presented due to their number (n=662). n.b. *p < 0.1, **p < 0.001, ***p<0.0001.*

	A	B	mean(A)	mean(B)	diff	SE	tail	T	p-tukey	efsize	eftype	Result
Between Birds												
0	1	2	8.04	8.48	-0.44	0.32	two-sided	-1.39	0.355	-0.136	hedges	Not Sig Diff
1	1	3	8.04	6.70	1.34	0.32	two-sided	4.11	0.001	0.410	hedges	Sig Diff**
2	2	3	8.48	6.70	1.78	0.28	two-sided	6.35	0.001	0.546	hedges	Sig Diff **
Between Feather												
3	P1	P3	8.31	7.50	0.81	0.32	two-sided	2.54	0.030	0.243	hedges	Sig Diff*
4	P1	P5	8.31	7.45	0.86	0.31	two-sided	2.76	0.016	0.257	hedges	Sig Diff*
5	P3	P5	7.50	7.45	0.05	0.30	two-sided	0.16	0.900	0.014	hedges	Not Sig Diff
Between Position												
6	dors	vent	7.90	7.55	0.34	0.25	two-sided	1.34	0.180	0.101	hedges	Not Sig Diff
Between Section												
7	0	1	8.96	8.50	0.46	0.60	two-sided	0.76	0.900	0.138	hedges	Not Sig Diff
8	0	3	8.96	8.05	0.91	0.59	two-sided	1.56	0.500	0.278	hedges	Not Sig Diff
9	0	5	8.96	7.14	1.82	0.59	two-sided	3.12	0.016	0.555	hedges	Sig Diff*
10	0	7	8.96	6.47	2.49	0.63	two-sided	3.93	0.001	0.755	hedges	Sig Diff**
11	1	3	8.50	8.05	0.45	0.35	two-sided	1.32	0.500	0.140	hedges	Not Sig Diff
12	1	5	8.50	7.14	1.36	0.34	two-sided	4.00	0.001	0.417	hedges	Sig Diff**
13	1	7	8.50	6.47	2.03	0.42	two-sided	4.84	0.001	0.619	hedges	Sig Diff**
14	3	5	8.05	7.14	0.91	0.33	two-sided	2.79	0.042	0.277	hedges	Sig Diff*
15	3	7	8.05	6.47	1.57	0.41	two-sided	3.87	0.001	0.480	hedges	Sig Diff*
16	5	7	7.14	6.47	0.66	0.40	two-sided	1.66	0.463	0.203	hedges	Not Sig Diff

Table 6.5: *One-way ANOVA results within feathers from a single bird, between different sections of the feather. Columns A and B use a shorthand where section 0 is 0–10% length, 1 is 10–30%, 3 is 30–50%, 5 is 50–70% and 7 is 70–90%. Degrees of freedom (sample size -1) are presented for each test. n.b. *p < 0.1, **p < 0.01, ***p<0.001.*

Bird	ddof1	ddof2	F	p-unc	np2	Result
1	4	158	32.075	1.47e-19	0.448	Sig Diff ***
2	4	272	40.444	1.40e-26	0.373	Sig Diff ***
3	2	259	3.906	2.13e-02	0.029	Sig Diff *

Table 6.6: *Tukey tests within feathers from a single bird, between different sections of the feather. n.b. *p < 0.1, **p < 0.01, ***p<0.001.*

	A	B	mean(A)	mean(B)	diff	SE	tail	T	p-tukey	efsize	eftype	Result
0	0	1	4.22	7.94	-3.72	0.68	two-sided	-5.47	0.001	-1.36	hedges	Sig Diff *
1	0	3	4.22	13.98	-9.76	0.94	two-sided	-10.35	0.001	-3.52	hedges	Sig Diff *
2	0	5	4.22	6.87	-2.65	0.76	two-sided	-3.51	0.004	-0.97	hedges	Sig Diff *
3	0	7	4.22	10.51	-6.29	0.89	two-sided	-7.05	0.001	-2.27	hedges	Sig Diff *
4	1	3	7.94	13.98	-6.04	0.79	two-sided	-7.67	0.001	-2.21	hedges	Sig Diff *
5	1	5	7.94	6.87	1.07	0.55	two-sided	1.96	0.287	0.39	hedges	Not Sig Diff
6	1	7	7.94	10.51	-2.57	0.73	two-sided	-3.54	0.004	-0.94	hedges	Sig Diff *
7	3	5	13.98	6.87	7.11	0.86	two-sided	8.34	0.001	2.59	hedges	Sig Diff *
8	3	7	13.98	10.51	3.47	0.98	two-sided	3.55	0.004	1.25	hedges	Sig Diff *
9	5	7	6.87	10.51	-3.64	0.80	two-sided	-4.57	0.001	-1.33	hedges	Sig Diff *
Bird 2												
10	0	1	14.53	10.93	3.60	0.88	two-sided	4.10	0.001	1.13	hedges	Sig Diff *
11	0	3	14.53	8.57	5.96	0.84	two-sided	7.06	0.001	1.88	hedges	Sig Diff *
12	0	5	14.53	8.21	6.32	0.89	two-sided	7.10	0.001	1.98	hedges	Sig Diff *
13	0	7	14.53	5.61	8.91	0.84	two-sided	10.59	0.001	2.81	hedges	Sig Diff *
14	1	3	10.93	8.57	2.36	0.56	two-sided	4.23	0.001	0.75	hedges	Sig Diff *
15	1	5	10.93	8.21	2.72	0.63	two-sided	4.35	0.001	0.86	hedges	Sig Diff *
16	1	7	10.93	5.61	5.32	0.55	two-sided	9.58	0.001	1.67	hedges	Sig Diff *
17	3	5	8.57	8.21	0.36	0.58	two-sided	0.63	0.900	0.11	hedges	Not Sig Diff
18	3	7	8.57	5.62	2.96	0.50	two-sided	5.89	0.001	0.93	hedges	Sig Diff *
19	5	7	8.21	5.62	2.59	0.58	two-sided	4.51	0.001	0.82	hedges	Sig Diff *
Bird 3												
20	1	3	5.82	6.85	-1.03	0.39	two-sided	-2.67	0.021	-0.53	hedges	Sig Diff *
21	1	5	5.82	6.80	-0.98	0.37	two-sided	-2.60	0.026	-0.51	hedges	Sig Diff *
22	3	5	6.85	6.80	0.08	0.26	two-sided	0.19	0.900	0.03	hedges	Not Sig Diff

Table 6.7: *Tukey tests within feathers from a single bird, between different positions (dorsal and ventral) of the feather. n.b. *p < 0.1, **p < 0.01, ***p<0.001.*

	A	B	mean(A)	mean(B)	diff	SE	tail	T	p-tukey	efsize	eftype	Result
1	dors	vent	9.03	7.19	1.91	0.55	two-sided	3.51	0.001	0.548	hedges	Sig Diff *
2	dors	vent	8.39	8.56	-0.17	0.48	two-sided	-0.35	0.732	-0.042	hedges	Not Sig Diff
3	dors	vent	6.67	6.72	-0.05	0.24	two-sided	-0.22	0.832	-0.027	hedges	Not Sig Diff

Table 6.8: *Tukey tests within feathers from a single bird, between different feathers on the wing. n.b. *p < 0.1, **p < 0.01, ***p<0.001*

	A	B	mean(A)	mean(B)	diff	SE	tail	T	p-tukey	efsize	eftype	Result
Bird 1												
0	P1	P3	9.72	7.23	2.49	0.78	two-sided	3.20	0.004	0.702	hedges	Sig Diff **
1	P1	P5	9.72	8.05	1.66	0.77	two-sided	2.17	0.078	0.470	hedges	Not Sig Diff
2	P3	P5	7.23	8.05	-0.82	0.61	two-sided	-1.35	0.368	-0.233	hedges	Not Sig Diff
Bird 2												
3	P1	P3	9.65	7.71	1.94	0.61	two-sided	3.18	0.004	0.495	hedges	Sig Diff **
4	P1	P5	9.65	8.43	1.22	0.60	two-sided	2.05	0.102	0.312	hedges	Not Sig Diff
5	P3	P5	7.71	8.43	-0.72	0.54	two-sided	-1.32	0.384	-0.183	hedges	Not Sig Diff
Bird 3												
6	P1	P3	6.97	7.45	-0.47	0.28	two-sided	-1.69	0.210	-0.258	hedges	Not Sig Diff
7	P1	P5	6.97	5.75	1.22	0.27	two-sided	4.59	0.001	0.666	hedges	Sig Diff ***
8	P3	P5	7.45	5.75	1.70	0.29	two-sided	5.86	0.001	0.924	hedges	Sig Diff ***

Within birds

Following some tentative results within the whole sample, the same analysis was repeated within each bird, though tests between lengthwise sections and between feathers are the main focus. ANOVA reveals differences between lengthwise sections within all three birds (Table 6.5). It is worth noting here, that some data is missing from Bird 3, due to samples being lost in the preparation process or because the tensile test failed due to stress concentrations introduced in the sample preparation process. *Post-hoc* tests, however, do not corroborate the observation of decreasing modulus along the feather within Bird 1 or Bird 3 (see Table 6.6), though a decrease is observed along the feather shaft in Bird 2.

ANOVA also reveals differences between feathers in all three birds, though *post hoc* tests again do not corroborate the proximal decrease (see Table 6.8. To be thorough, differences between dorsal and ventral positions were also revisited within each bird and it was found that there was no significant difference in Birds 2 and 3, but that there was a difference in Bird 1 where means were 9.03 and 7.12 GPa, respectively (see Table 6.7).

6.2 Discussion

Lees et al. (2017) report that within species, I is an adequate proxy for EI, but that between species this is no longer the case. *Bachmann et al.* (2012) also reports that mechanical properties are more to do with geometry and less to do with E, that broadly speaking E does not change. To that effect it is a shame a larger sample couldn't be tested which also included specimens from different species. It is quite difficult to test samples from feathers much smaller than those of a swan and still control for the variables considered above.

The ANOVA results which consider the whole sample clearly show that effective E is not constant, and pairwise test revealed two possible trends. They were a decrease in modulus along the

rachis and a decrease in modulus with proximity to the body in feathers. The former perhaps has a functional explanation in that the shaft at any lengthwise point has to resist the moments applied by the feather area distal to that point, if I does not scale with the moment, then E would be expected to change and would likely be expected to decrease (*Pennycuick*, 2008). It is also the case that the vane chord is smaller, though rachis I also decreases and may explain that. The latter might have been expected given that P1 has a different vane shape (there is no emargination), and that the vertical component of load may be slightly different for each of these feathers because wing loading is not evenly distributed along the chord and the aerodynamic centre of pressure is at the quarter-chord position (*Pennycuick*, 2008), and finally because P1 has to resist more oncoming drag. That observation might also be explained by increasing shear stress along the length of the feather.

However, all of these results should be interpreted cautiously because the sample is small and because there are differences between individuals. Individual differences means that it is likely that some, if not all, of the variance observed between other groupings is explained by differences between individuals. These results then call for repeated analysis within birds to confirm the trend.

Upon individual analysis the results still show that E is certainly variable, but they also show no convincing evidence of change with section, length or position. This finding contradicts results by *Macleod* (1980), who reported that effective modulus *increases* along the length of pelvic contour feathers, by *Cameron et al.* (2003) who found that better alignment of keratin fibres increases stiffness along the feather and also results by *Wang and Meyers* (2017) who demonstrated an increase in dorsal tests between the calamus, the mid-shaft and the rachis, though they did not control for individual variation and the trend was not present in lateral or ventral samples. At the time of writing there are no tests between different feathers which offer a comparison. Overall, the statistical analyses within birds was inconclusive, no trend was observed in E between sections along the feather, between dorsal and ventral

positions or between feathers P1, P3, and P5.

6.2.1 Limitations

This testing approach is quite standard, but usually applied to pieces which have been made to exact specifications. In the commercial world, these specimens are generally large because specimens are manufactured rather than harvested and because larger samples are easier to test. Biological tissues are comparatively small in size. Therefore, aspects which are usually ignored for the sake of simplicity and because their effects are small within uniform pieces introduce potentially larger errors in this case. Some of these limitations are considered briefly here before Chapter 7 attempts to address one of the most significant emissions.

'Engineering stress' is not 'True stress'. The difference lies in accounting for changing cross-sectional area during the test. The Poisson effect means that for an isotropic specimen, or any specimen where $E_1 > E_2$, the gauge length will become narrower under load and this will have a corresponding effect on cross-sectional area. Cross-sectional area is a term in the equation which calculates stress $\sigma = N/A$, and is therefore also present in the equation which uses stress to calculate modulus $E = \sigma/\varepsilon$. The effect of changing cross-sectional area is usually small and if samples are very similar it is common practice to ignore it. Taking this change into account would involve measuring strain in two other dimensions for a test conducted on a rectangular prism. Measuring these two other strains becomes even more complicated if one of those dimensions is very small, as is the case in a flat plate, and with dissected feather shaft samples. This effect is probably still quite small in dissected feather shaft samples but it does mean that the reported moduli will be smaller than the true value.

Hysteresis is the phenomenon in which the value of a physical property lags behind changes in the effect causing it. In tensile testing this is normally called a strain-rate dependency and can be mostly accounted for by using a higher rate of strain. Hysteresis was observed in some testing which came before this present work,

which is why the rate of extension used in this work was chosen. Testing samples of different sizes with a uniform rate of extension also introduces this problem, though it is difficult to see a way around it. To record the same amount of data in a shorter period of time is an extra requirement of the test apparatus and is no problem for physical strain gauges but the varying geometry of feather samples requires video extensometry. Unfortunately, the use of video extensometry introduces a trade-off because either less data is recorded, or expensive equipment with higher frame rates and/or data transfer rates needs to be sourced.

The curvature in Figure 6.1 is a manifestation of strain-rate dependency, which has either been introduced by the method or is present as a viscoelastic response (as reported by (*Fortier et al.*, 2012, *Gao et al.*, 2014)) or both. Considering viscoelasticity in more detail is beyond the scope of the current work and no further consideration will be made.

The final and most important consideration is that Chapter 4 has shown there to be a layer of differently oriented fibres in the calamus and superior umbilical region. If the material is similar, or at least is E_1 of the inner layer is larger than E_2 of the outer layer then not considering this would also lead to underestimating E_1. This is probably the most significant effect but it also compounds other smaller effects. Chapter 7 will reanalyse those samples in the calamus and apply Classical Laminate Mechanics.

Chapter 7

Loading a laminate

Chapter 6 did not reveal a trend in the tensile test results between feathers P1, P3, and P5, between dorsal and ventral positions or between the length-wise sections. Some limitations were detailed in section 6.2.1. One of the most serious limitations was not accounting for differences in the laminar structure, especially when the layer which is ignored is oriented perpendicular to the principal loading direction. Chapter 4 showed there was a differently oriented layer of fibres in the calamus and superior umbilical region and this should therefore be considered in the analysis of tensile pieces from the calamus because there is likely to be a significant mechanical effect. That effect would be an underestimation of E_1 if E_1 is significantly larger than E_2. The reanalysis that follows uses equations from Classical Laminate Mechanics (*Daniel and Ishai*, 2006, *Kaw*, 2006) and applies them to the experimental setup shown in Figure 3.9 on page 50 to estimate the stiffnesses Q_{11} Q_{22}, which relate to E_1 and E_2

7.1 Obtaining Q_{11}, Q_{22}

A transversely orthotropic material can be fully characterised by five independent elastic constants (*Daniel and Ishai*, 2006). They are $E_{xx}, E_{yy}, \nu_{xy}, \nu_{yx}$ and G. E is a modulus of elasticity, ν is a

ratio of strains in orthotropic directions and G is a shear modulus. For the special case of a two-ply laminate, where the laminae are roughly oriented at 0°(Layer 1) and 90°(Layer 2) to the loading axis, the shear modulus is not required and only four constants are needed. The equations to follow will consider such a laminate and solve for Q. Q is a stiffness matrix which is needed to calculate E

Assumptions:

1. $Q_{12} = Q_{21}$
2. Two layers are oriented 0°and 90°

The first assumption is appropriate because each layer can be treated as a thin laminate in plane-stress conditions, and this is one reduction that can be made in the stress-strain relations (*Daniel and Ishai*, 2006).

If

$$\left[\begin{array}{c} N_x \\ N_y \\ N_\gamma \\ \hdashline M_x \\ M_y \\ M_\gamma \end{array}\right] = \left[\begin{array}{c:c} A & B \\ \hdashline C & D \end{array}\right] \left[\begin{array}{c} \varepsilon_x \\ \varepsilon_y \\ \varepsilon_\gamma \\ \hdashline \kappa_x \\ \kappa_y \\ \kappa_\gamma \end{array}\right] \tag{7.1}$$

where A is the extensional stiffness matrix, B and C are coupling matrices and D is a shear matrix, then where moments are controlled and there are two layers in the laminate,

$$A_{i,j} = Q_{i,j}|_1 \cdot t_1 + Q_{i,j}|_2 \cdot t_2 \tag{7.2}$$

where $t_1 = z_{top1} - z_{bottom1}$, and Qs are the stiffnesses that populate A, then the stress-strain relations become

$$\begin{bmatrix} N_x \\ N_y \\ N_{\gamma y} \end{bmatrix} = \sum_k t_k \cdot \begin{bmatrix} Q_{xx} & Q_{xy} & Q_{x\gamma} \\ Q_{yx} & Q_{yy} & Q_{y\gamma} \\ Q_{\gamma x} & Q_{\gamma y} & Q_{\gamma\gamma} \end{bmatrix} \begin{bmatrix} \varepsilon_x \\ \varepsilon_y \\ \gamma \end{bmatrix} \tag{7.3}$$

for a laminate where the loading axis is denoted $_{x,y}$.

Then, suppose the two-layered laminate has layers oriented at 0° and 90° to the loading axis, transverse load N_y and shear stress N_γ can be set to 0, the stress-strain relations become:

$$\begin{bmatrix} N_x \\ N_y = 0 \end{bmatrix} = \begin{bmatrix} Q_{11}t_1 + Q_{22}t_2 & Q_{12}t_1 + Q_{21}t_2 \\ Q_{21}t_1 + Q_{12}t_2 & Q_{22}t_1 + Q_{11}t_2 \end{bmatrix} \begin{bmatrix} \varepsilon_x \\ \varepsilon_y \end{bmatrix} \quad (7.4)$$

where the principal axes of the layers are denoted $_{1,2}$ and with stiffness matrices B, C and $D = 0$. Matrices B and C are coupling stiffnesses and matrix D comprises the bending stiffnesses. $Q_{16}, Q_{26}, Q_{61}, Q_{62}$ and $Q_{66} = 0$

Then, a pair of equations can be obtained:

$$N_x = \quad (Q_{11}t_1 + Q_{22}t_2)\varepsilon_x + (Q_{12}t_1 + Q_{21}t_2)\varepsilon_y \quad (7.5)$$
$$N_y = 0 = (Q_{21}t_1 + Q_{12}t_2)\varepsilon_x + (Q_{22}t_1 + Q_{11}t_2)\varepsilon_y \quad (7.6)$$

and the strains can be brought inside the parentheses to produce:

$$N_x = \quad \varepsilon_x Q_{11}t_1 + \varepsilon_x Q_{22}t_2 + \varepsilon_y Q_{12}t_1 + \varepsilon_y Q_{21}t_2 \quad (7.7)$$
$$N_y = 0 = \varepsilon_x Q_{21}t_1 + \varepsilon_x Q_{12}t_2 + \varepsilon_y Q_{22}t_1 + \varepsilon_y Q_{11} \quad (7.8)$$

If $Q_{12} = Q_{21}$, and they become:

$$N_x = \quad \varepsilon_x t_1 Q_{11} + \varepsilon_x t_2 Q_{22} + \varepsilon_y (t_1 + t_2) Q_{12} \quad (7.9)$$
$$N_y = 0 = \varepsilon_x (t_1 + t_2) Q_{12} + \varepsilon_y t_1 Q_{22} + \varepsilon_y t_2 Q_{11} \quad (7.10)$$

and Equation 7.10 can be solved for Q_{12}:

$$Q_{12} = \frac{\varepsilon_y t_1 Q_{22} + \varepsilon_y t_2 Q_{11}}{-\varepsilon_x (t_1 + t_2)} \quad (7.11)$$

Equation 7.11 can then be substituted into Equation 7.9 to give:

$$N_x = \varepsilon_x t_1 Q_{11} + \varepsilon_x t_2 Q_{22} - \frac{\varepsilon_y{}^2}{\varepsilon_x}(t_1 Q_{22} + t_2 Q_{11}) \quad (7.12)$$

where $\nu_{xy} = -\frac{\varepsilon_y}{\varepsilon_x}$.

$$N_x = (\varepsilon_x t_1 + \varepsilon_y t_2 \nu_{xy}) Q_{11} + (\varepsilon_x t_2 + \varepsilon_y t_1 \nu_{xy}) Q_{22} \tag{7.13}$$

alternatively,

$$N_x \varepsilon_x = (\varepsilon_x{}^2 t_1 - \varepsilon_y{}^2 t_2) Q_{11} + (\varepsilon_x{}^2 t_2 - \varepsilon_y{}^2 t_1) Q_{22} \tag{7.14}$$

and then

$$Q_{11} = \frac{E_1}{1 - \nu_{12}\nu_{21}} = \frac{1}{\nu_{12}} Q_{12} \tag{7.15}$$

$$Q_{22} = \frac{E_2}{1 - \nu_{12}\nu_{21}} = \frac{1}{\nu_{21}} Q_{12} \tag{7.16}$$

again where $Q_{12} = Q_{21}$.

Figure 7.1 shows values for E which have already been published. Section 2.3 has argued that those values should not strictly be compared but they do provide reasonable boundaries and expectations for the stiffnesses calculated using the Equations 7.15 and 7.16. However $Q \neq E$ because terms in the stiffness matrix are subject to the Poisson effect. As a result, estimates for E are lower then Q and Equation 7.15 sets $E = 0.84Q$ when $\nu = 0.4$, which is the value used by *Soons et al.* (2012) in their modeling work.

7.2 Reanalysis of tensile data

Axial and transverse strains were used with load data and the equations presented in Section 7.1 to calculate the stiffnesses Q_{11} and Q_{22}. They can be plotted against one another for each frame of video extensometry data and if Poisson's ratio is known then there is a point on each line which can be taken to represent Q_{11} and Q_{22}. Thus, each line should intersect with every other line at this point. Figure 7.2 shows an example dataset and it can be seen that the intersection point is non-physical, which indicates that some error has been introduced.

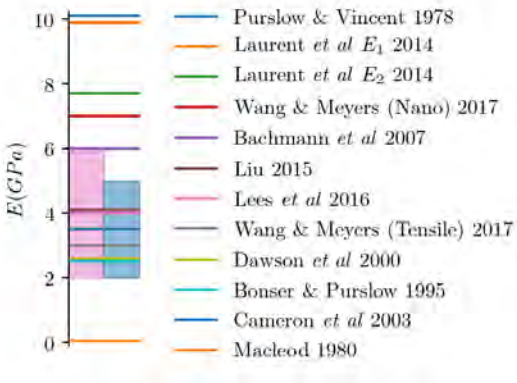

Figure 7.1: *Modulus values reported in the literature (see Chapter 2 for some analysis. Cameron (blue) and Lees (pink) report ranges of data.)*

That error is most likely to be in the transverse strain data. It might be because the method used is not precise enough to capture such small transverse strains, or because of the complex cross-sectional geometry of the test pieces. 'Complex' in this context, means that the pieces were not deforming in the way a flat sample would, and were curling, flattening, or deforming in local areas due to the ventral grooves or dorsal stiffening bars. This will be discussed in more detail in the next section.

In that case, average values for both stiffnesses still provide reasonable limits for the true stiffnesses, when combined with the isotropic boundary condition and $Q_{22} > 0$.

Figure 7.3 shows average values for 8 tensile tests, only 5 lines are visible because three datasets presented negative (non-physical) Q_{22} values. More than 8 samples with two cortical layers were tested but some were lost due to failure caused by imperfect dissection and cracks propagating from the grip jaws.

The Poisson's ratio for each sample and the average values for those tests with plausible values are presented in Table 7.1. These ratios were calculated after anomalous values were removed (values that were negative or more than two orders of magnitude different).

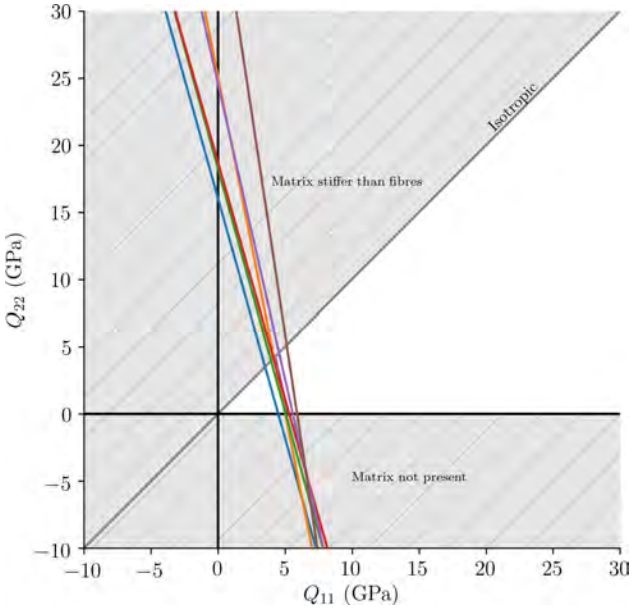

Figure 7.2: *A plot of Q_{22} vs. Q_{11} for a single tensile test. Q_{11} and Q_{22} can be computed using the equation presented in section 7.1. In this graph, each line represents a single time-stamp from the tensile data. Dashed lines are mean values for Q_{11} and Q_{22}. It can be assumed that at a minimum, the real values will not be above the isotropic line, because anisotropy has been demonstrated. It can also be assumed that the real value does not fall beneath the X axis, because this means Q_{22} is either 0 or below, which is non physical.*

The average value was $\nu = 0.4$ with a standard deviation of 0.18 when all datasets were combined. Though the sample is very small this is the first value to be presented from pieces of calamus using a repeatable method.

Most materials have Poisson's ratio values ranging between 0.0 and 0.5 and most biological materials have Poisson's ratio values between approximately 0.3 and 0.4 (*Wang*, 2016). This observation suggests that the error which has caused datasets to present negative Q_{22} values is more likely to have been complex cross-sectional

Table 7.1: *A table which shows the average values for Poisson's ratio from tensile tests in which both strains were adequately recorded, after erroneous values were removed. Global averages are also presented.*

Dataset	ν_{xy}	$\sigma_{\nu_{xy}}$
0	0.36	0.12
1	0.51	0.10
2	0.16	0.06
3	0.36	0.17
4	0.53	0.11
All	0.4	0.18

geometry than a noisy signal in the transverse strain data. This means that repeating the experiment with better strain measurement would likely not have yielded very different results but a smaller sample piece should have been used which is less likely to deform unexpectedly. In practice this would still entail using a better method of measuring transverse strain because the signal-to-noise ratio would decrease with a smaller piece. So, the question arises—Can the data which contains unreliable transverse strain measurements still be used? The mechanism by which error has been introduced should be considered in more detail before any further treatment or interpretation can proceed.

7.3 Transverse strain measurements are unreliable in three samples

Transverse strain measurements in 3 out of 8 samples are inaccurate, and this inaccuracy is better explained by complex geometries and small deformations than they are by noise because all of the data are noisy. Video playback of the extensometry data from one experiment very clearly shows how this transverse expansion under

axial loading might have been recorded.

In this work, the circular calamus was longitudinally bisected into dorsal and ventral parts, which then have a semi-circular cross section. When a beam of this cross section is put under tension it tries to flatten the arc of the cross section because a stiffness is resisting tension. This manifests as a perceived widening to an observer in the axial plane, and this widening is likely to be greater than the contraction due to Poisson's effect. This arc is also flattened by the grips, which sometimes cause a crack to form when they are tightened, which then propagates under load, or the crack may form under load if not already formed upon tightening the grips. This also makes the measurement of transverse strain unreliable because in that case the sample is effectively two separate pieces. Both of these effects could be addressed by testing a thinner sample. However, the production of thinner samples was found to be extremely difficult in that notches were produced that might cause the test to fail suddenly, and this would also augment any effects present due to small variations in local geometry, which is a feature of biological samples. One such variation, which is commonly found in the superior umbilical region, is the formation of dorsal ridges and a corresponding thin section between them. This has the effect of shortening the gauge width to effectively 0, and is another cause of the cracking mentioned in the preceding paragraph. There is no way to account for this properly.

If this flattening is misleading the analysis it might then be fair to set the transverse strains equal to zero, but that would introduce another assumption, that $dEA/dz = 0$ in the gauge length tested.

7.3.1 $dEA/dz \to 0$ for small sections but not for a whole feather

When *Purslow and Vincent* (1978) presented the first paper on the mechanical properties of primary feathers, they presented an equation (which has been repeated in this thesis as equation 2.1 on page 24) which is correct for a beam of constant EI, *i.e.* where dEI/dz is small. However, with the discovery of layers in the calamus this

assumption is inappropriate for testing the whole feather and Section 6.2.1 also listed works by *Cameron et al.* (2003), *Macleod* (1980), *Wang and Meyers* (2017) which further support that conclusion. However, SRCT scans show this assumption is likely true within the gauge lengths tested in this work and the equations that follow show that any term which contains a differential of EI goes to zero in this case.

$$\frac{d\delta}{dz} = \theta \tag{7.17}$$

$$\frac{d^2\delta}{dz^2} = \frac{d\theta}{dz} = \frac{M}{EI} \tag{7.18}$$

$$\begin{aligned}\frac{d^3\delta}{dz^3} =& \frac{d^2\theta}{dz^2} = \frac{d}{dz}\left(\frac{M}{EI}\right) = \\ & \frac{1}{EI}\frac{d}{dz}(M) + M\frac{d}{dz}\left(\frac{1}{EI}\right) = \\ & \frac{F}{EI} - \frac{M}{(EI)^2}\frac{d}{dz}(EI)\end{aligned} \tag{7.19}$$

$$\begin{aligned}\frac{d^4\delta}{dz^4} =& \frac{d^3\theta}{dz^3} = \frac{d^2}{dz^2}\left(\frac{M}{EI}\right) = \\ & \frac{d}{dz}\left(\frac{F}{EI} - \frac{M}{(EI)^2}\frac{d}{dz}(EI)\right) = \\ & \frac{q}{EI} - 2\frac{F}{(EI)^2}\frac{d}{dz}(EI) + 2\frac{M}{(EI)^3}\frac{d}{dz}(EI) - \frac{M}{(EI)^2}\frac{d^2}{dz^2}(EI)\end{aligned} \tag{7.20}$$

So, if $dEA/dz = 0$, it is reasonable to set transverse strain equal to zero for all datasets. The calculation of Q_{11} and Q_{22} can then be repeated with this condition and Figure 7.3 re-drawn as Figure 7.4, which shows the average line for each of eight datasets. Global averages and standard deviations are shown on the isotropic line for Q_{22} and on the X axis for Q_{11} and the mean values are $Q_{11} \leq 5.49 \pm 2.11$ and $Q_{22} \leq 4.29 \pm 1.68$. This give effective limits as $3.4 < Q_{11} < 7.6$ and $0 < Q_{22} < 5.9$. If $\nu = 0.4$, then E values are $E_1 = 4.59$ and $E_2 = 3.6$

These values are lower than those reported in Chapter 6, which is to be expected but also lower than those derived from earlier nanoindentation work (*Laurent et al.*, 2014) which were $Q_{11} = 10.7$ and $Q_{22} = 7.8$ but still well within the other reported moduli which have been presented in Figure 7.1.

These values are also more spread out than might have been expected. This could be due to differences in protein structure which have been identified in Chapter 5 and by the use of Engineering Strain rather than True Strain.

The sample is too small to justify bold claims about the material constants of feather keratin, and perhaps even swan primary feathers but it is now clear that failing to consider laminar geometry in the analysis of mechanical data from the calamus or the superior umbilical region could lead to a large under-estimation of the stiffness matrix Q and the moduli E_1 and E_2. There is work to be done in expanding the sample size, the size of the sample space (more feathers and more species) and by refining the preparation of samples such that a thin sample is used, which does not suffer from problems caused by semicircular geometry, by improving the measurement of transverse strain, by introducing a method to measure the third orthogonal strain and finally, by applying this approach to calami where there are more than two layers or where the outside layer is not perpendicular to the axially aligned inner layer. This will be set out in the Further Work section on page 176.

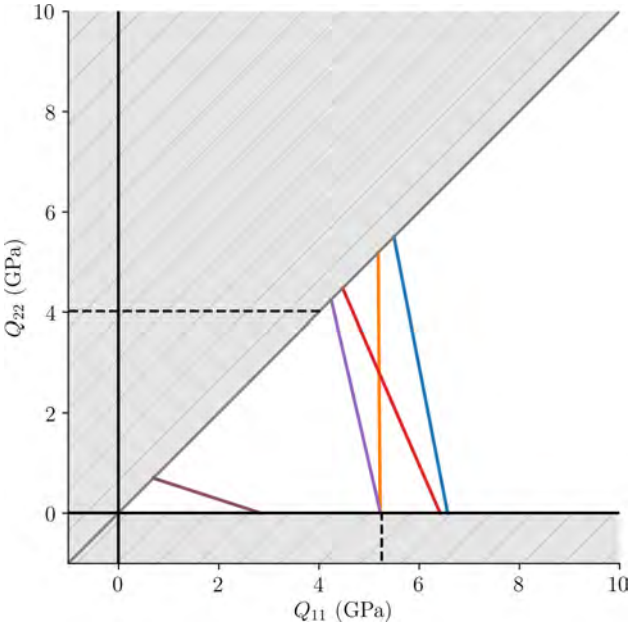

Figure 7.3: *A plot of average Q_{22} vs. average Q_{11} for tensile tests in the calamus. Q_{11} and Q_{22} can be computed using the equations presented in section 7.1. In this graph, each line represents a single point in time from the tensile data. Dashed lines then set out some proposed boundary conditions to constrain possible values. It can be assumed that at a minimum, the real values will not be above the isotropic line, because anisotropy has been demonstrated. It can also be assumed that the real value does not fall beneath the X axis because this is non-physical.*

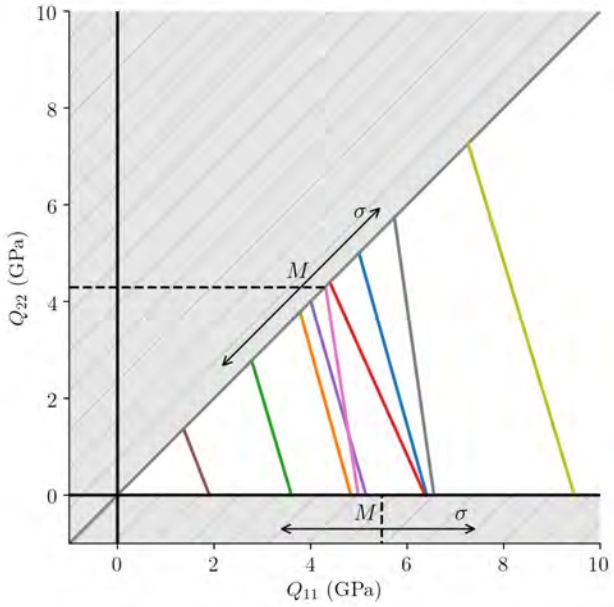

Figure 7.4: *A plot of average Q_{22} vs. average Q_{11} for multiple tensile tests, where transverse strain is set to 0. Q_{11} and Q_{22} can be computed using the equations presented in section 7.1. In this graph, each line represents an average value over the whole loading period from one tensile dataset. M indicates the global mean and is pictured with standard deviations.*

Chapter 8

How laminar structure, geometry and material properties affect EI

E is multivariate

Three objectives were identified in Section 1 on page 2. Chapter 2 introduced context and background to these objectives, before three respective questions were posed in the Method's section. The three following chapters dealt with experimental data and analysis to address these questions, though discussion was mostly restricted in scope to the question posed and results from other chapters were not considered. This section will set those three chapters, and the results obtained, into a more coherent discussion of feather mechanics.

8.1 E or I: Material Properties or Geometry?

Bending stiffness EI of a simple cantilever comprises Young's modulus, E, and the second moment of area, I. This means that where

one of these variables is approximately constant, variation in bending stiffness should be largely explained by variation in the other variable. In many engineering applications, this is often the case. However, can the same be said of a bird feather? There is no question that I changes along a feather shaft—the question is does E change as well. This section will discuss two important papers which report contradictory information and then make the case for variability in E.

***Bachmann et al.* (2012)** compared the stiffnesses EI and second moments of area I between pigeons and owls. No significant variation in indentation modulus was found between the two birds (However, differences in indentation modulus between proximal and distal regions were found in both), though, calculated bending stiffnesses were found to be very different due to the contribution from the second moment of area. Bachmann *et al.* have interpreted the results to claim that flexural stiffness is predominantly influenced by the geometry of the feathers. This position is shared by *Purslow and Vincent* (1978), though later work by Purslow reports that E does increase distally (*Bonser and Purslow*, 1995).

***Lees et al.* (2017)** looked at using I to predict flight ability in fossil bird taxa following an earlier paper by some of the same authors (*Nudds and Dyke*, 2010) which suggested that it might be possible to make inferences about flight ability from the external measurements of feathers preserved in rocky strata. Central to that idea is the assumption that the material and structural properties of a primary flight feather may be consistently calculated from the external diameter of the feather rachis, which is the only dimension that is likely to relate to structural properties available from fossils. Using three-point bending tests, *Lees et al.* (2017) showed that there is a relationship between mechanical properties (maximum bending moment M_{max} and bending modulus E_{bend}) and external morphological parameters (rachis length, diameter and second moment of area at the calamus) in 180 primary feath-

ers from four species of bird of differing flight style. The results showed that intraspecifically, both E_{bend} and M_{max} were strongly correlated with all three morphological measures. However, without accounting for species, are a poor predictor of rachis structural properties. This suggests that E is not constant across all feathers, and this is supported by *Bonser and Purslow* (1995) and *Cameron et al.* (2003). A reasonable question to ask at this point is—is one single variable responsible or at least approximately representative of shaft stiffness? It seems not to be the case and the sections to follow will explain this by comparing some simpler artificial beams.

8.1.1 A cantilevered steel rod

Consider a cantilevered beam made from steel. Mild steel has a modulus of ≈ 200 GPa. Though this material property is constant, mild steel has been engineered to support myriad different loads in a cantilever configuration, from springy diving boards, to sturdy bridges. Because E is constant, what is responsible for the change in bending stiffness is a change in I. I can be increased by keeping the same cross-sectional shape but adding more material (consider a steel tooth-pick *vs.* a concrete reinforcement bar) or by keeping the amount of material constant but changing the shape (consider a round bar *vs.* an 'I' beam). Often the strategy is to optimise the shape for a given load, and then expand the size until the loading requirement can be safely sustained, because steel and design have associated costs.

8.1.2 A cantilevered biological beam

Like the previous example, it is also true that the structure of keratin is highly conserved (*Greenwold and Sawyer*, 2011). Following this information, it is not unreasonable to expect mechanical properties to be largely constant. This should mean that, as in the case of a cantilevered steel beam of constant cross-section, variation in bending stiffness would be controlled by the amount of keratin material used and the shape of its cross-section. This was in fact

reported by *Bachmann et al.* (2012) in the paper entitled *Flexural stiffness of feather shafts: geometry rules over material properties.* However, more comprehensive analysis in a paper entitled *Rachis morphology cannot accurately predict the mechanical performance of primary feathers* by *Lees et al.* (2017) showed that this was not the case. Could it be that E is not constant after all?

8.1.3 A case for the likelihood of variability in E

If the data and results that have been presented in the preceding chapters are set aside for a moment, then it is reasonable to ask—Does it make sense that E would vary, given that the feathers are a very costly tissue to produce and the penalty for possessing inadequate feathers is likely death? Figure 8.1a, shows how primary feathers flex in stable flight. One can imagine that the wing becomes fixed and the feathers become a cantilever, and this is shown by the hatched box in Figure 8.1b. From observation, it seems that the feather's deflections are approximately parabolic, which is shown in Figure 8.1c. Beginning from this parabolic deflection, Moment-area theorem says it is possible to predict change in angle by using:

$$\theta = \frac{d\delta}{ds} \approx \frac{d\delta}{dx}, \tag{8.1}$$

which would result in a constant change of angle as shown in Figure 8.1d Taking the second derivative results in the $\frac{M}{EI}$ diagram, which would also be constant, as shown in Figure 8.1e.

$$\frac{M}{EI} = \frac{d\theta}{dx} \tag{8.2}$$

$\frac{load}{EI}$ would follow the same value for the whole beam if there are no weak points, and the whole beam is only as strong as it needs to be. This is a reasonable expectation when a penalty is conferred for increasing weight or expending more energy. To obtain EI, the moment, M, would need to be known and this line of reasoning can go no further.

Considering the load on the feather, q, in the bottom subfigure, Figure 8.1i. In reality the load would be approximately elliptical, but varying with the width of the vane. For the sake of simplicity, and because performing the same thought experiment with an elliptically distributed load makes only a very small difference, an equally distributed load is assumed

Moment-area theory also says that shear stress Q can be found by integration, as shown in Figure 8.1h.

$$Q = \int q dx \tag{8.3}$$

and then the moment is obtained by a second integration to form a quadratic, as shown in Figure 8.1g.

$$M = \int Q dx \tag{8.4}$$

and we arrive again at EI but no further progress can be made by intuition, though it is clear that I has been optimised from Figure 2.2 on page 9. *Lees et al.* (2017) reports a gamma distribution and both *Pennycuick* (2008) and *Lees et al.* (2017) report that I does not adequately predict flexural stiffness. This means that E *must* change, by some mechanism. Ideally, E and I would be separated (measured) which has proven to be non-trivial, if laminar properties are considered.

8.1.4 Multivariate E in fibre-composites

The mechanical properties of fibre composites are both more complicated and less understood than those of mild steel. Variation in mechanical performance can come from a number of variables, such as fibre/matrix fraction (within and between layers), different properties of the fibres or the matrix, the number of layers, the orientation of those layers, consistent orientation of fibres within the layers, *etc.*

Chapter 4 showed that the layup of a bird feather is not fixed in the feather shaft, and there exists at least one extra layer of radially

aligned fibres in the calamus that extends distally into the superior umbilical region. Intuition may make the case that if the laminate E_x does not change but layup does, then material E_1 *does* change. Chapter 5 showed that the makeup of individual layers changes. Although it's not clear whether this change is driven by a change in volume fraction, or a change in the makeup of fibres, the results of Chapter 5 show that there is inter-layer variation in E or that E *does* change. Chapter 6 showed that for feathers from *Cygnus spp.*, effective E ranges from 5 to 15 GPa, and that the variation does not appear to be well explained by place on the wing, position (dorsal or ventral), section (place along the feather), or individual bird. These results come from an experiment in which geometry was controlled, which leads to the conclusion that E *does* change. By the application of classical laminate mechanics, and by intuition, work in Chapter 7 has showed that E *does* change, and in the layups present in Swan primary feathers it might account for as much as 15% change. *Considering the results of these three chapters together, results have shown that a significant part of variability in E_{lam} comes from changes in layup, and changes in E_1 might come from changes in protein structure and consistent alignment.*

The next section will consider why changing these variables might be likely from functional, ecological and developmental perspectives.

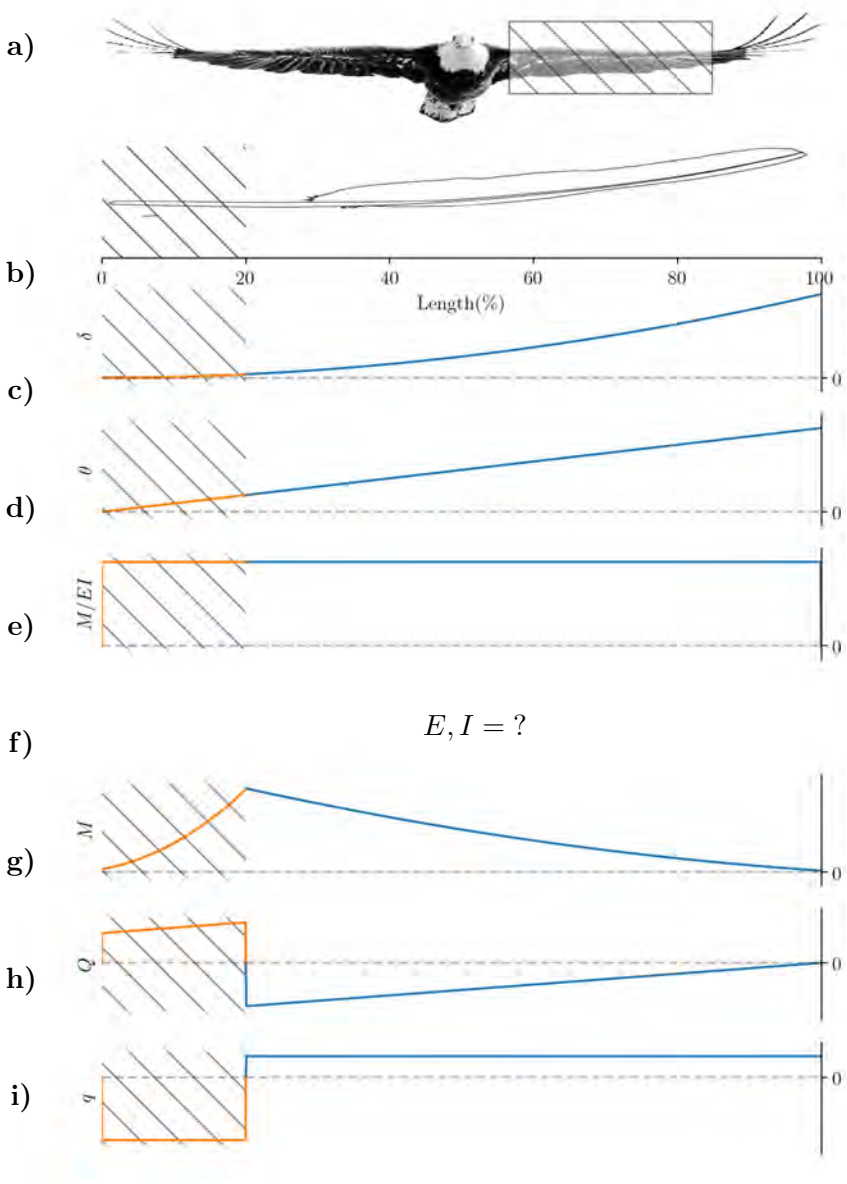

Figure 8.1: *Continued overleaf*

Figure 8.1: *A figure shows how mechanical terms vary with along the length of the feather shaft. From the top down, subfigure* ***a)*** *show how a primary feather deforms in flight and* ***b)*** *shows a cantilevered feather. Graphs* ***c-e)*** *show how* ***c)****deflection,* δ*,* ***d)****angle* θ*, and* ***e)*** *moment over stiffness, change along the feather by derivation. From the bottom up, graphs* ***i-g)*** *show how* ***i)*** *load* q*,* ***h)*** *shear force* Q *and* ***g)*** *moment* M*, might change along the feather shaft, which resists a distributed load and is cantilevered by the ligaments and tendons of the post-patagium and at the proximal end, by the carpometacarpus and wing digit bone material. Subfigure* ***f)*** *makes the point that* E *and* I *need to be separated and measured to properly characterise the mechanical behaviour of the bird feather shaft.*

8.1.5 E and I vary for different reasons and in different places

There is now a body of evidence that both E and I change along the length of the feather shaft and that variation in bending stiffness EI is not dominated by one or the other when talking about the feather shaft as a whole tissue.

Figure 8.1 shows how some mechanical properties might be expected to change along a cantilevered beam with respect to a planar load (and these relations are well known in mechanical engineering, where the two regions are termed the anchor arm and the cantilever arm). This figure shows how the shaft can be split into two functional parts, whether or not these parts are delimited at the calamus / rachis boundary by other definitions. From this standpoint, the largest moment and load are experienced at the boundary between them. In most industrial structures the entire beam is a constant prism which is able to resist the maximum of those forces. This is mostly because the design and manufacture of something so variable increases the cost by a huge amount, though where the same pressures are driving design and manufacture *e.g.* an aircraft wing, some similar adaptations have been implemented in terms of changing geometry, and by using fibre composites for weight reduction.

Clever tricks in changing the modulus E are not as common because joining materials is difficult and introduces another set of problems. It is also the case in most engineering applications that the trade-off can be compensated for elsewhere. For example in an aircraft wing, weight / frontal area *etc.* can be compensated by thrust coming from a bigger engine or different fuel, or weight can be saved elsewhere, but this is not possible for a bird that is trying to survive in competition, and that constructs feathers by extruding them from a follicle which can be adapted as the feather is deployed. For a bird it makes more sense to divide the feather into three regions, the calamus, the superior umbilical region and the rachis. The most distal part, the rachis, resists bending loads and would fail by buckling. Here, that failure is best resisted by

a foam core which is explained by parallel axis theory, and the structure can be thought of as a sandwich structure with thin lateral walls. In many birds, dorsal teeth form to add more bulk to the dorsal part of the cortex to further resist bending forces. The lateral tissue of the rachis serves as an attachment point for the vane more than it does to resist loading. The most proximal part, the calamus, which is beneath the skin and partly articulated in bone, is unlikely to be the failure point and will not buckle, so it does not require a foamy medulla. However, the vane will induce a torsional load which can only be resisted in the anchor-arm of the beam and so a layer of radially aligned fibres becomes useful. These fibres are not present further up the shaft as previously thought. In between these regions is a zone of delimitation, the superior umbilical region, where the moment and shear force is highest. To resist the moment, I is varied by the formation of dorsal teeth and ventral ridges, a thicker dorso-ventral aspect and medullary foam is still observed. This thickening and the form of the plumulaceous region is explained by developmentary reasoning. If the amount of tissue allocated to the vane is reduced (as it would be to form the plumulaceous barbs), then the additional tissue could enhance the size and ventro-lateral extent of the superior umbilical region (*Maderson et al.*, 2009). Figure 8.2 shows that I increases to a maxima somewhere near the maximum moment as pictured in Figure 8.1g, and this seems to be true across multiple birds using data from multiple experiments. As well as varying I, a layer of radial fibres begins to form where the torsion becomes relevant in the anchored arm of the cantilever, the calamus. This region is the most likely to fail, and the failure mode could be in buckling or shear. This shear failure might explain the difference in protein structure, because the outer layer has more α-configured residues which may indicate more matrix is in place to better resist shear failure band builds on the work began more than 70 years ago by *Rudall* (1947). It also makes sense that the feathers are supported by the soft tissue of the post-patagium because if the bird does hit a gust or some turbulence, or even clips the feather on a branch as

it flies past, some of this force can be absorbed and distributed by the soft tissue of the post-patagium which means that the material which inserts into the bone does not need to be as tough or fatigue resistant. Apart from thermoregulation this might also suggest why feathers are not emarginated here, so that large forces can also be absorbed by the adjacent feather and transmitted to the skeleton to stop local failures. Two of these regions (the rachis and the calamus) regions already fit with common terminology but now the proposal by *Maderson et al.* (2009) to include a third section called the superior umbilical region is convincing, where for chiefly functional reasons but also developmental reasons there are adaptations which mean that the material is different from the rachis and the calamus and neither of those terms appropriately describe the form or function of the feather shaft in this region.

8.2 Summary

Many workers and some figures presented earlier in this work (Figures 4.18-4.22, on page 101) have shown that I varies along a feather shaft (*Bachmann et al.*, 2012, 2007, *Lees et al.*, 2017, *Pennycuick*, 2008). However, it seems that variation in I alone does not adequately explain variation in bending stiffness EI. This leads to the conclusion that E also varies along a feather shaft, which has also been reported by other workers (*Bonser and Purslow*, 1995, *Cameron et al.*, 2003, *Laurent et al.*, 2014, *Macleod*, 1980, *Purslow and Vincent*, 1978, *Wang et al.*, 2012) and reinforced by work in Chapters 4, 5 and 6. This had previously been seen as an inconsistency by *Bachmann et al.* (2012) and *Lees et al.* (2017), but when the layup, as discovered by *Lingham-Soliar et al.* (2010), is considered from a mechanical perspective a more coherent explanation forms.

The feather is best thought of as a 3-part composite beam. The proximal part of the shaft, to which the vanes attach, should still be called the rachis. This part is characterised by a quadrilateral cross section with dorsal teeth and a medullary substantia which

help it to resist bending loads and failure by buckling. All of the fibres in this part are axially oriented. The calamus is the proximal, sub-dermal part of the feather which is characterised by a circular cross section. It has two layers of fibres, an inner layer of fibres which extends into the rachis and an outer layer of radial fibres to resist a torque applied by the vane. It does not contain a medullary substantia because it would be unlikely to fail by buckling. In-between these two regions is the superior umbilical region, which has a sub-circular cross section and two layers of fibres though the outer layer of fibres tapers away towards the rachis. It may fail either by buckling or in shear, but the sub-circular cross section reduces stress-concentrations that would be present in a structure with radial fibres wrapping a square prism. The outer layer resists torsion and the inner layer resists bending, which is also supported by medullary substantia. Both bending forces and shear forces are supported by the adjacent feather and this as well as the post-patagial tendon act as a toughening mechanism to reduce the likelihood of shear failure.

The calamus / rachis delimitation has always been an ambiguous area in avian biology, but given that the feather is a functional appendage and it is under functional pressure, function should also define the terms used to describe its form where possible. The work in this thesis has formed a more coherent naming convention and solved some of the inconsistencies which have been the subject of recent work (*Bachmann et al.*, 2012, *Lees et al.*, 2017).

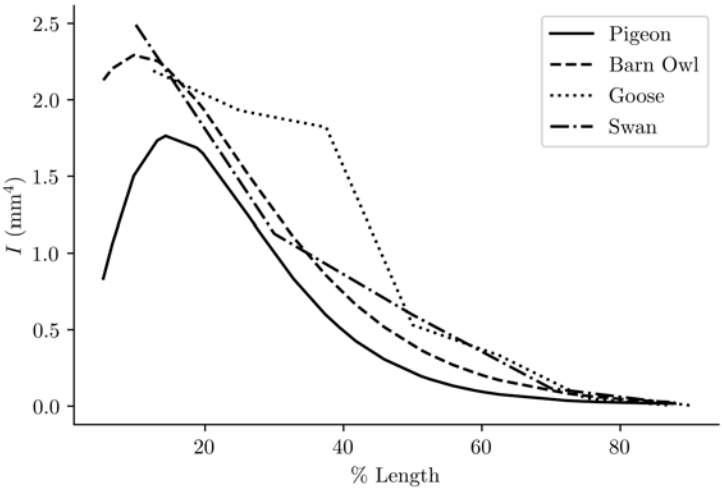

Figure 8.2: *This graph shows the second moment of area as a function of shaft length for shaft cross sections in four birds. The goose data come from* Pennycuick *(2008). It is only described as a primary feather. The barn owl and pigeon data come from* Bachmann et al. *(2012) and are average values from six replicate fifth primaries (P5). The swan data comes from CT data already presented in Chapter 4 and is from the first primary (P1). It can be seen that whilst the second moment of area, I, varies a small amount—there is no clear difference between these birds which are markedly different in phylogeny, flight style and weight, and of course the feathers are also from different places on the wing. This further reinforces the conclusions of* Lees et al. *(2017), that I is a poor predictor of flexural stiffness or flight ability.*

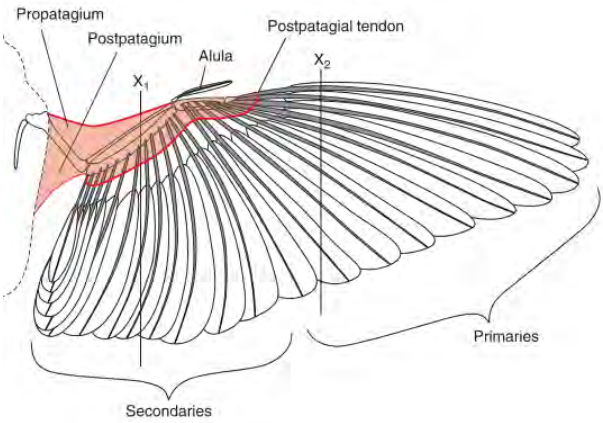

(a) *Dorsal perspective-*

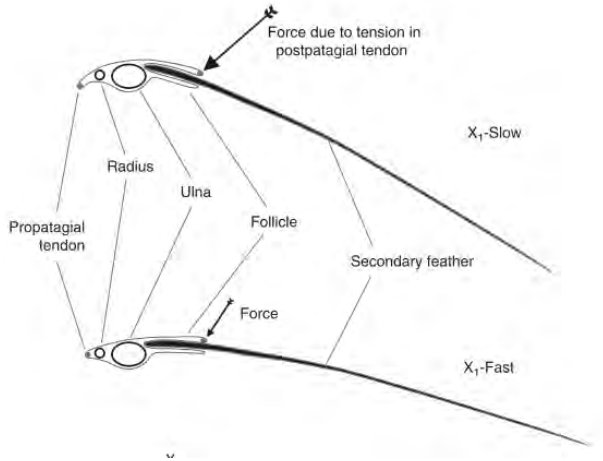

(b) *Lateral perspective*

Figure 8.3: *A figure to show the functional parts of the wing anatomy from a materials perspective. The figure shows the feathers, how they articulate into the metacarpus, and the soft-tissue support given to the superior-umbilical region by the post-patagial tendon. This anatomy would relieve loading at the cantilevered point so that load is passed to the soft tissue and the adjacent feather before an individual feather yields, effectively increasing toughness. Both figures reproduced from* Pennycuick *(2008)*

Chapter 9

Conclusions and further work

9.1 Conclusions

The major objective of this work was to look at selected primary feathers in order to gain an improved understanding of their laminar structure and mechanical properties. As outlined in Chapter 1 three questions were to be addressed in order to achieve this objective. The questions were:

Q1 What is the geometry of the laminar composite in the cortex of a primary flight feather shaft?

Results from the first repeatable method to measure layer orientation and thickness have indicated that there can be two or three layers in the proximal calamus but the orientation of them remains unknown. There are only two in the distal calamus of all samples considered in this work. The outer layer can account for up to half of the cortical width in this region and it extends past most definitions of the rachis-calamus boundary before it tapers into nothing. This suggests that common definitions should be updated and the zone of discontinuity proposed by *Maderson*

et al. (2009) is now the most appropriate. By approximately 40% length from the tip of the calamus, the zone of discontinuity has finished, the outer layer is no longer present and the rachis proper has been reached. Here, there is only one layer of fibres and they are axially oriented.

Q2 Are there differences in the structure of the proteins which make up the different layers of the feather shaft?

Chapter 5 presented the first vibrational spectra from intact feathers and clear data to indicate that the rachis layers are different, and that the inner layer contains more β -sheet configured protein. It also seems that there is within-layer variation, where the inner part of the inner layer contains more β -sheet than the outer part of the inner layer.

Q3 Are the layers mechanically relevant and is the isotropic assumption appropriate?

Chapter 4 shows that there are layers with differently oriented fibres in the proximal shaft but not in the distal shaft. Chapters 7 and 9.1, notably section 7.2, show that the layers do have a mechanical effect the first calculated estimates for E_1 and E_2 at the laminar level of the structural hierarchy, demonstrate that the isotropic assumption is not appropriate.

Aside from the answers provided for these questions, there have been some other significant contributions.

- Work published by *Laurent et al.* (2019) evaluated the available techniques on their ability to observe laminar geometry in feathers. The paper has added a large number of images of the feather microstructure to the literature and suggested that three techniques could have been used to address to Question 1, but that only SRCT was practicable within the constraints of this project. Future workers will find this paper useful in their refinement of the CT method, extension

of the data presented in this thesis, or in their application of scanning confocal polarised microscopy or serial-block-face scanning electron microscopy to feathers or other keratinous material when the techniques become more accessible.

- A major step in approaching Question 1 has been the development of both the concept of using interstitial holes in the cortex to infer fibre orientation and in implementing the analysis.

- The correct energy to use at a synchrotron for computed tomography of feather rachis samples is 14 KeV.

- On the application of Raman spectroscopy to feather keratin, the first Raman spectra from the Amide I and Amide III regions of intact feathers have been presented and methods used to record and analyse spectra have been developed. A lasting contribution in this aspect are band assignments made in three regions of the Raman spectrum, the Amide I, Amide III and S-S regions.

- On accounting for variation in mechanical properties, the holes in the cortex may be a contributing source.

- A collection of feathers and wings now exists at the University of Southampton, which has already supported this project and three masters projects. The author hopes this collection will be maintained and grown to support undergraduate and postgraduate projects in the future. Any student wishing to expand this collection can contact the author for a list of names and local businesses who might provide feathers in the future.

- A formal relationship between the Institute of Vertebrate Palaeontology and Palaeoanthropology (IVPP) of the Chinese Academy of Science, and the University of Southampton / The National Oceanography Centre has been established such that a framework is now in place for student exchange.

Further Work

The results of this thesis demonstrate that a number of valuable experiments could be performed and lines of enquiry investigated in the future. When the author proposed a masters' project on the biomechanics of feathers in 2014, the line of inquiry was supposed to begin and end with variation in second moment of area along the rachis. Nearly four years later, variation in the second moment has not been fully understood and the introduction of this thesis hinted that more questions would be uncovered than answered. Some of these questions are presented in the sections to follow.

Prehistoric development and flight

Examination of Amber fossils

- *Thomas et al.* (2014) used Raman spectroscopy to look for colour pigments in amber-preserved fossil-feathers. Using a 1064 nm light source, they were able to confirm the presence of melanin in fossil feathers but could not find any evidence for carotenoid pigments. They present spectra from modern feathers, fossil feathers preserved in rock and fossil feathers preserved in amber. All of these spectra, plus many more, are included as raw data in the supplement of their paper.

  Whilst they did not investigate protein structure, they have confirmed the possibility of obtaining Raman spectra from feathers preserved in Amber. Unfortunately, the spectra presented in their supplement do not resolve the Amide I or Amide III regions well at all. As part of the present work, all of the spectra of *Thomas et al.* (2014) were smoothed with a Savitsky-Golay filter and plotted, but no information can be extracted from the spectral regions fitted in Chapter 5, and fitting those regions was not possible.

  It would be extremely interesting to obtain similar spectra to those presented earlier in this thesis from feathers preserved

in Amber.

- *Xing et al.* (2018, 2016) have also presented synchrotron images of well resolved avialan bone and feathers preserved in Amber. These scans do not resolve the textures of holes or even the cross-sections of the feathers, but their images suggest it could be just the small matter of changing optics and scan parameters to be able to revisit the questions posed in Chapter 4 and apply them to amber-preserved feathers.

Understanding feather material

- The method used in Chapter 4 could also be improved with an automatic thresholding method, which would allow some investigation into the number and size of holes between species, feathers and pieces of feather.

- Chapter 4 makes use of the holes observed in the rachises of feathers, but it has also revealed that these holes are not always present through the entire cortex and are rarely seen in the calamus. It is currently unknown why these holes exist and whether they are actively formed and have a functional purpose, or whether they are passively formed and result from mechanical deformation. It would be an interesting study to look at a series of developing feathers to answer that question, or to perform high cycle testing on a newly grown feather.

- Chapter 4 also did not manage to present the layup in the calamus, and it is clear that the elliptical holes present in the rachis cannot be used to answer this question. It remains a question deserving of further investigation, whether the investigation attempts to use even more highly resolved CT scanning or ptychography or some other method.

- Chapter 4 looked at primary feathers from swans, but not from other birds. A large amount of data was collected at

DLS to that effect but inadequate reconstructions did not permit them to be used. They are archived on tape at the Diamond Light Sourceand should be reconstructed with the GridRec algorithm to check that the data really cannot be used. If they cannot, there is currently no data on the layup in different birds, apart from the swan presented in this work, 3 samples presented by *Laurent et al.* (2014) (which does included data from the chicken, bald eagle and partridge) and some very qualitative reports by *Lingham-Soliar* (2015) made in the course of some other work which was slightly different in scope.

- Chapter 5 showed that Raman spectroscopy, using the Amide I region, can be used effectively to study the change in protein secondary structure of the inner and outer layers of a feather calamus. It is anticipated that with improvement of the technique and sample preparation methods that much more detail will be derived concerning the protein structures in these layers, particularly if the Amide III and S-S regions can be used with the Amide I region.

- Chapter 6 measured how the material performs under tension, but this does not mimic exactly how that material is loaded in application, and there were some challenges in sample preparation and holding. Some workers have argued that a 3 or 4 point bending test is more appropriate. However, given the development of full field methods, it might even be possible in the future to perform Digital Image Correlation on a feather in a wind tunnel or even Digital Volume Correlation on a sample loaded inside a CT scanner.

With the conclusions presented above and the further work proposed, it is clear that major advances in the understanding of feathers can be achieved, and a new area of science has been opened.

Bibliography

Akhtar W and Edwards HG. Fourier-transform Raman spectroscopy of mammalian and avian keratotic biopolymers. *Spectrochimica acta. Part A, Molecular and biomolecular spectroscopy*, **53**(96), 81–90 (1997). ISSN 13861425.

Alibardi L and Toni M. Cytochemical, biochemical and molecular aspects of the process of keratinization in the epidermis of reptilian scales. *Progress in Histochemistry and Cytochemistry*, **40**(2), 73–134 (2006). ISSN 00796336.

Almutawah A, Barker SA and Belton PS. Hydration of gluten: A dielectric, calorimetric, and fourier transform infrared study. *Biomacromolecules* (2007). ISSN 15257797.

Andersen A and Kak A. Simultaneous Algebraic Reconstruction Technique (SART): A superior implementation of the ART algorithm. *Ultrasonic Imaging*, **6**(1), 81–94 (1984). ISSN 0161-7346.

Astbury WT and Woods HJ. X-Ray Studies of the Structure of Hair, Wool, and Related Fibres. II. The Molecular Structure and Elastic Properties of Hair Keratin. *Philosophical Transactions of the Royal Society A: Mathematical, Physical and Engineering Sciences* (1934). ISSN 1364-503X.

Atwood RC, Bodey AJ, Price SW, Basham M and Drakopoulos M. A high-throughput system for high-quality tomographic reconstruction of large datasets at diamond light source. *Philosophical*

Transactions of the Royal Society A: Mathematical, Physical and Engineering Sciences (2015). ISSN 1364503X.

Bachmann T. Pers Comms (28 March) (2014).

Bachmann T, Emmerlich J, Baumgartner W, Schneider J and Wagner H. Flexural stiffness of feather shafts: geometry rules over material properties. *The Journal of Experimental Biology*, **215**(Pt 3), 405–15 (2012). ISSN 1477-9145.

Bachmann T, Klän S, Baumgartner W, Klaas M, Schröder W and Wagner H. Morphometric characterisation of wing feathers of the barn owl Tyto alba pratincola and the pigeon Columba livia. *Frontiers in Zoology*, **4**(1), 23 (2007). ISSN 1742-9994.

Banhart J. *Advanced tomographic methods in materials research and engineering*. Oxford University Press (2008). ISBN 9780199213245.

Barth A. Infrared spectroscopy of proteins. *Biochimica et Biophysica Acta (BBA) - Bioenergetics*, **1767**(9), 1073–1101 (2007). ISSN 0005-2728.

Barth A and Zscherp C. What vibrations tell about proteins. *Quarterly Reviews of Biophysics*, **35**(4), S0033583502003815 (2002). ISSN 00335835.

Berkovich ES. Three-Faceted Diamond Pyramid for Studying Microhardness by Indentation. *Zavodskaia laboratoriia* (1950).

Bertram J and Gosline J. Functional design of horse hoof keratin: The modulation of mechanical properties through hydration effects. *J.Exp. Biol.*, **130**, 121–136 (1987).

Blanch EW, Hecht L and Barron LD. Vibrational Raman optical activity of proteins, nucleic acids, and viruses. *Methods*, **29**(2), 196–209 (2003). ISSN 1046-2023.

Boccaccio A, Ballini A, Pappalettere C, Tullo D, Cantore S and Desiate A. Finite element method (FEM), mechanobiology and biomimetic scaffolds in bone tissue engineering. *International journal of biological sciences*, **7**(1), 112–132 (2011). ISSN 1449-2288.

Bonser RHC and Purslow P. The Young's modulus of feather keratin. *The Journal of Experimental Biology*, **198**(4), 1029–1033 (1995).

Borgudd J. Mechanical properties of bird feathers–influence of UV-radiation and mechanical fatigue. *A Lund Techn. Univ. Report TVSM-5121* (2003).

Busson B, Engström P and Doucet J. Existence of various structural zones in keratinous tissues revealed by X-ray microdiffraction. *Journal of Synchrotron Radiation*, **6**(5), 1021–1030 (1999). ISSN 0909-0495.

Buurlage JW, Kohr H, Jan Palenstijn W and Joost Batenburg K. Real-time quasi-3D tomographic reconstruction. *Measurement Science and Technology*, **29**(6), 064005 (2018). ISSN 0957-0233.

Buurlage JW, Marone F, Pelt DM, Palenstijn WJ, Stampanoni M, Batenburg KJ and Schlepütz CM. Real-time reconstruction and visualisation towards dynamic feedback control during time-resolved tomography experiments at TOMCAT. *Scientific Reports 2019 9:1*, **9**(1), 1–11 (2019). ISSN 2045-2322.

Buxbaum E. *Fundamentals of protein structure and function*. Springer, Berlin (2015). ISBN 9783319199191.

Cai S and Singh BR. Identification of β-turn and random coil amide III infrared bands for secondary structure estimation of proteins. *Biophysical Chemistry*, **80**(1), 7–20 (1999). ISSN 0301-4622.

Calabri L, Pugno N, Rota A, Marchetto D and Valeri S. Nanoindentation shape effect: experiments, simulations and modelling. *J. Phys.: Condens. Matter*, **19**(19) (2007).

Calvaresi M, Eckhart L and Alibardi L. The molecular organization of the beta-sheet region in Corneous beta-proteins (beta-keratins) of sauropsids explains its stability and polymerization into filaments. *Journal of Structural Biology*, **194**(3), 282–291 (2016). ISSN 10958657.

Cameron GJ, Wess TJ and Bonser RHC. Young's modulus varies with differential orientation of keratin in feathers. *Journal of Structural Biology*, **143**(2), 118–123 (2003). ISSN 10478477.

Chirgadze YN, Fedorov OV and Trushina NP. Estimation of amino acid residue side-chain absorption in the infrared spectra of protein solutions in heavy water. *Biopolymers*, **14**(4), 679–694 (1975). ISSN 0006-3525.

Choe C, Schleusener J, Lademann J and Darvin ME. Keratin-water-NMF interaction as a three layer model in the human stratum corneum using in vivo confocal Raman microscopy. *Scientific Reports*, **7**(1), 15900 (2017). ISSN 2045-2322.

Chou SF, Overfelt Ra and Miller ME. Anisotropic mechanical behavior of keratin tissue from quill shells of North American porcupine (Erethizon dorsatum). *Materials Science and Engineering A*, **557**, 36–44 (2012). ISSN 09215093.

Church JS, Poole AJ and Woodhead AL. The Raman analysis of films cast from dissolved feather keratin. *Vibrational Spectroscopy*, **53**(1), 107–111 (2010). ISSN 09242031.

Corning WWR and Biewener AA. In vivo strains in pigeon flight feather shafts: Implications for structural design. *Journal of Experimental Biology*, **201**(22), 3057–3065 (1998). ISSN 1477-9145.

Dalla Valle L, Nardi A, Bonazza G, Zuccal C, Emera D and Alibardi L. Forty keratin-associated proteins form the hard layers of scales, claws, and adhesive pads in the green anole lizard, Anolis carolinensis. *Journal of Experimental Zoology Part B: Molecular and Developmental Evolution*, **314B**(1), 11–32 (2010). ISSN 15525007.

Daniel I and Ishai O. *Engineering mechanics of composite materials*. Oxford University Press, Oxford, 2nd edition (2006).

Dawson A, Hinsley S, Ferns P, Bonser RHC and Eccleston L. Rate of moult affects feather quality: a mechanism linking current reproductive effort to future survival. *Proc. R. Soc. Lond. B*, **267**(1457), 2093,2098 (2000).

De La Hera I, Hedenström A, Pérez-Tris J and Tellería JL. Variation in the mechanical properties of flight feathers of the blackcap Sylvia atricapilla in relation to migration. *Journal of Avian Biology*, **41**(3), 342–347 (2010). ISSN 09088857.

Dong J, Dinakarpandian D and Carey PR. Extending the raman analysis of biological samples to the 100 micromolar concentration range. *Applied Spectroscopy* (1998). ISSN 00037028.

Doube M, Kłosowski MM, Arganda-Carreras I, Cordelières FP, Dougherty RP, Jackson JS, Schmid B, Hutchinson JR and Shefelbine SJ. BoneJ: free and extensible bone image analysis in ImageJ. *Bone*, **47**(6), 1076–1079 (2010).

Dowd BA, Campbell GH, Marr RB, Nagarkar VV, Tipnis SV, Axe L and Siddons DP. Developments in synchrotron x-ray computed microtomography at the National Synchrotron Light Source. In U Bonse, editor, *Developments in X-Ray Tomography II*, volume 3772, pages 224–236. International Society for Optics and Photonics (1999). ISSN 0277786X.

Dudgeon DE and Mersereau RM. Multidimensional Digital Signal Processing (1985).

Earland C, Blakey P and Stell J. Molecular orientation of some keratins. *Nature*, **196**, 1287–1291 (1962a). ISSN 00280836.

Earland C, Blakey P and Stell J. Studies on the structure of keratin IV. The molecular structure of some morphological components of keratins. *Biochimica et Biophysica Acta*, **56**, 268–274 (1962b). ISSN 00063002.

Essendoubi M, Meunier M, Scandolera A, Gobinet C, Manfait M, Lambert C, Auriol D, Reynaud R and Piot O. Conformation changes in human hair keratin observed using confocal Raman spectroscopy after active ingredient application. *International Journal of Cosmetic Science*, page 12528 (2019). ISSN 0142-5463.

Feo TJ, Field DJ and Prum RO. Barb geometry of asymmetrical feathers reveals a transitional morphology in the evolution of avian flight. *Proceedings of the Royal Society B: Biological Sciences.*, **282**(1803) (2015). ISSN 1471-2954.

Filshie BK and Rogers GE. An electron microscope study of the fine structure of feather keratin. *The Journal of cell biology*, **13**, 1–12 (1962). ISSN 0021-9525.

Fortier P, Suei S and Kreplak L. Nanoscale strain-hardening of keratin fibres. *PloS one*, **7**(7), e41814 (2012). ISSN 1932-6203.

Franck A, Cocquyt G, Simoens P and De Belie N. Biomechanical Properties of Bovine Claw Horn. *Biosystems Engineering*, **93**(4), 459–467 (2006). ISSN 1537-5110.

Fraser BR and Parry DA. Lepidosaur ß-Keratin Chains With Four 34-Residue Repeats: Modelling Reveals A Potential Filament-Crosslinking Role. *Journal of Structural Biology*, page 107413 (2019). ISSN 1047-8477.

Fraser RD and Parry DA. Amino acid sequence homologies in the hard keratins of birds and reptiles, and their implications for

molecular structure and physical properties. *Journal of Structural Biology*, **188**(3), 213–224 (2014). ISSN 10958657.

Fraser RDB and MacRae TP. Structural organization in feather keratin. *Journal of Molecular Biology*, **7**(3), IN9–IN11 (1963). ISSN 00222836.

Fraser RDB and MacRae TP. The molecular structure of feather keratin. In *Proc 16th Int. Ornith. Congress*, pages 443–451. Canberra (1976).

Fraser RDB, MacRae TP, Parry DAD and Suzuki E. The structure of feather keratin. *Polymer*, **12**(1), 35–56 (1971). ISSN 00323861.

Fraser RDB, MacRae TP and Rogers GE. Keratins. Their composition, structure and biosynthesis. *The Quarterly Review of Biology*, **48**(2), 378–379 (1973a).

Fraser RDB, MacRae TP and Rogers GE. Keratins—Their composition, structure and biosynthesis (1973b).

Fraser RDB, MacRae TP, Sparrow LG and Parry DAD. Disulphide bonding in α-keratin. *International Journal of Biological Macromolecules*, **10**(2), 106–112 (1988). ISSN 01418130.

Fraser RDB and Parry DAD. The molecular structure of reptilian keratin. *International Journal of Biological Macromolecules*, **19**(207) (1996).

Fraser RDB and Parry DAD. Molecular packing in the feather keratin filament. *Journal of Structural Biology*, **162**(1), 1–13 (2008). ISSN 10478477.

Fraser RDB and Parry DAD. The structural basis of the filament-matrix texture in the avian/reptilian group of hard a-keratins. *Journal of Structural Biology*, **173**(2), 391–405 (2011). ISSN 10478477.

Fu FN, DeOliveira DB, Trumble WR, Sarkar HK, Singh BR, Fen-NiFu, Singh BR, DeOliveira DB, Sarkar HK and Trumble WR. Secondary Structure Estimation of Proteins Using the Amide III Region of Fourier Transform Infrared Spectroscopy: Application to Analyze Calcium-Binding-Induced Structural Changes in Calsequestrin. *Applied Spectroscopy, Vol. 48, Issue 11, pp. 1432-1441*, **48**(11), 1432–1441 (1994). ISSN 0003-7028.

Fuchs E and Marchuk D. Type I and type II keratins have evolved from lower eukaryotes to form the epidermal intermediate filaments in mammalian skin. *Proceedings of the National Academy of Sciences of the United States of America*, **80**(19), 5857–5861 (1983). ISSN 0027-8424.

Galván I, Jorge A, Ito K, Tabuchi K, Solano F and Wakamatsu K. Raman spectroscopy as a non-invasive technique for the quantification of melanins in feathers and hairs. *Pigment Cell and Melanoma Research*, **26**(6), 917–923 (2013). ISSN 17551471.

Gao JL, Chu JK, Guan L, Shang HX and Lei ZK. Viscoelastic characterization of long-eared owl flight feather shaft and the damping ability analysis. *Shock and Vibration*, **2014**, 1–9 (2014). ISSN 10709622.

Gere JM. *Mechanics of materials*. Thompson, Belmont, CA, 6th edition (2008). ISBN 0071129391.

Goggin PM, Zygalakis KC, Oreffo ROC and Schneider P. High-resolution 3D imaging of osteocytes and computational modelling in mechanobiology: Insights on bone development, ageing, health and disease. *European Cells and Materials*, **31**, 264–295 (2016). ISSN 14732262.

Greenwold MJ and Sawyer RH. Linking the molecular evolution of avian beta (β) keratins to the evolution of feathers. *Journal of Experimental Zoology Part B: Molecular and Developmental Evolution*, **316B**(8), 609–616 (2011). ISSN 15525007.

Hahn MB, Solomun T, Wellhausen R, Hermann S, Seitz H, Meyer S, Kunte HJ, Zeman J, Uhlig F, Smiatek J and Sturm H. Influence of the Compatible Solute Ectoine on the Local Water Structure: Implications for the Binding of the Protein G5P to DNA. *The Journal of Physical Chemistry B*, **119**(49), 15212–15220 (2015). ISSN 1520-6106.

Huang Y, Zhang F, HwangG K, Nix W, Pharr G and FENG G. A model of size effects in nano-indentation. *Journal of the Mechanics and Physics of Solids*, **54**(8), 1668–1686 (2006). ISSN 00225096.

Jackson M and Mantsch H. The use and misuse of FTIR spectroscopy in the determination of protein structure. *Critical Reviews in Biochemistry and Molecular Biology*, **30**(2), 95–120 (1995).

Kadir M, Wang X, Zhu B, Liu J, Harland D and Popescu C. The structure of the "amorphous" matrix of keratins. *Journal of Structural Biology* (2017).

Kak AC and Slaney M. *Principles of Computerized Tomographic Imaging*. IEEE Press, New York, electronic edition (2001). ISBN 978-0-89871-494-4.

Kaw AK. *Mechanics of composite materials*. Taylor & Francis, Boca Raton, 2nd edition (2006). ISBN 0-8493-1343-0.

Kherlopian AR, Song T, Duan Q, Neimark MA, Po MJ, Gohagan JK and Laine AF. A review of imaging techniques for systems biology (2008).

Khosa MA, Wu J and Ullah A. Chemical modification, characterization, and application of chicken feathers as novel biosorbents. *RSC Advances*, **3**(43), 20800 (2013). ISSN 2046-2069.

King S. The bird feather rachis: a morphological and statistical study (2016).

Kyrieleis A, Titarenko V, Ibison M, Connolley T and Withers PJ. Region-of-interest tomography using filtered backprojection: Assessing the practical limits. *Journal of Microscopy*, **241**(1), 69–82 (2010). ISSN 00222720.

Laurent C, Ahmed S, Boardman R, Cook, R.B., Dyke G, Palmer C, Schneider P and DeKat R. Imaging techniques for observing laminar geometry in the feather shaft cortex. *Journal of Microscopy*, page jmi.12820 (2019). ISSN 0022-2720.

Laurent CM, Dyke JM, Cook RB, Dyke G and de Kat R. Spectroscopy on the wing: Investigating possible differences in protein secondary structures in feather shafts of birds using Raman spectroscopy. *Journal of Structural Biology*, **211**(1), 107529 (2020). ISSN 10958657.

Laurent CM, Palmer C, Boardman RP, Dyke G and Cook RB. Nanomechanical properties of bird feather rachises: Exploring naturally occurring fibre reinforced laminar composites. *Journal of the Royal Society Interface*, **11**(101) (2014). ISSN 17425662.

Lees J, Garner T, Cooper G, Nudds RL, Lees J, Garner T and Cooper G. Rachis morphology cannot accurately predict the mechanical performance of primary feathers in extant (and therefore fossil) feathered flyers. *Royal Society Open Science*, **4**(2) (2017).

Li BW, Zhao HP, Feng XQ, Guo WW and Shan SC. Experimental study on the mechanical properties of the horn sheaths from cattle. *Journal of Experimental Biology* (2010). ISSN 00220949.

Lingham-Soliar T. Feather structure, biomechanics and biomimetics: the incredible lightness of being. *Journal of Ornithology*, **155**(155), 323–336 (2013). ISSN 2193-7192.

Lingham-Soliar T. *The vertebrate integument volume 2: Structure, design and function*. Springer-Verlag, Berlin (2015). ISBN 9783662460054.

Lingham-Soliar T. Microstructural tissue-engineering in the rachis and barbs of bird feathers. *Scientific Reports*, **7**, 45162 (2017). ISSN 20452322.

Lingham-Soliar T, Bonser RHC and Wesley-Smith J. Selective biodegradation of keratin matrix in feather rachis reveals classic bioengineering. *Proceedings. Biological sciences / The Royal Society*, **277**(1685), 1161–8 (2010). ISSN 1471-2954.

Lingham-Soliar T and Murugan N. A new helical crossed-fibre structure of β-keratin in flight feathers and its biomechanical implications. *PloS one*, **8**(6), e65849 (2013). ISSN 1932-6203.

Liu ZQ, Jiao D, Meyers MA and Zhang ZF. Structure and mechanical properties of naturally occurring lightweight foam-filled cylinder-The peacock's tail coverts shaft and its components. *Acta Biomaterialia*, **17**, 137–151 (2015). ISSN 18787568.

Lucas AM and Stettenheim PR. *Avian anatomy: Integument (Agricultural Handbook 362)*. United States Department of Agriculture, Michigan (1972).

Macleod GD. Mechanical properties of contour feathers. *J. exp. Biol*, **87**, 65–71 (1980).

Maderson PF, Hillenius WJ, Hiller U and Dove CJ. Towards a comprehensive model of feather regeneration. *Journal of Morphology*, **270**(10), 1166–1208 (2009). ISSN 03622525.

Maiti N, Apetri MM, Zagorski MG, Carey PR and Anderson VE. Raman Spectroscopic Characterization of Secondary Structure in Natively Unfolded Proteins: a-Synuclein. *J. AM. CHEM. SOC*, **126**, 2399–2408 (2004).

Marone F and Stampanoni M. Regridding reconstruction algorithm for real-time tomographic imaging. *Journal of Synchrotron Radiation*, **19**(6), 1029–1037 (2012). ISSN 09090495.

McKittrick J, Chen P, Bodde SG, Yang W, Novitskaya EE and Meyers MA. The structure, functions, and mechanical properties of keratin. *Jom*, **64**(4), 449–468 (2012). ISSN 1047-4838.

Meyers MA, Chen PY, Lin AYM and Seki Y. Biological materials: Structure and mechanical properties (2008).

Meyers MA, McKittrick J and Chen P. Structural biological materials: critical mechanics-materials connections. *Science*, **339**(6121), 773–779 (2013). ISSN 1095-9203.

Müller R. Hierarchical microimaging of bone structure and function (2009).

Naito S and Arai K. Type and location of SS linkages in human hair and their relation to fiber properties in water. *Journal of Applied Polymer Science*, **61**(12), 2113–2118 (1996). ISSN 00218995.

Ng Siang C, Wu P, Fan WL, Yan J, Chen CK, Lai YT, Wu SM, Mao CT, Chen JJ, Lu MYJ, Ho MR, Widelitz RB, Chen CF, Chuong CM and Li WH. Genomic Organization, Transcriptomic Analysis, and Functional Characterization of Avian α- and β-Keratins in Diverse Feather Forms. *Genome Biology and Evolution*, **6**(9), 2258–2273 (2014). ISSN 1759-6653.

Nudds RL and Dyke G. Narrow primary feather rachises in Confuciusornis and Archaeopteryx suggest poor flight ability. *Science*, **328**(5980), 887–9 (2010). ISSN 1095-9203.

Nudds RL, Kaiser G and Dyke G. Scaling of avian primary feather length. *PLoS ONE*, **6**(2) (2011). ISSN 19326203.

Oliver W and Pharr G. An improved technique for determining hardness and elastic modulus using load and displacement sensing indentation experiments. *J. Mater. Res.*, **7**(3), 613–617 (1992).

Olorunnisola AO and Olorunnisola AO. Mechanical Properties of Wood. In *Design of Structural Elements with Tropical Hardwoods*, pages 31–47. Springer (2017).

Otsu N. A threshold selection method from gray-level histograms. *IEEE Transactions on Systems, Man, and Cybernetics*, **9**(1), 62–66 (1979). ISSN 0018-9472.

Overman SA and Jr. GJT. Raman Markers of Nonaromatic Side Chains in an α-Helix Assembly: Ala, Asp, Glu, Gly, Ile, Leu, Lys, Ser, and Val Residues of Phage fd Subunits†,‡. *Biochemistry*, **38**, 4018–4027 (1999).

Pabisch S, Puchegger S, Kirchner HOK, Weiss IM and Peterlik H. Keratin homogeneity in the tail feathers of Pavo cristatus and Pavo cristatus mut. alba. *Journal of Structural Biology*, **172**(3), 270–275 (2010). ISSN 10478477.

Parry DA, Fraser RD, Alibardi L, Rutherford KM and Gemmell N. Molecular structure of sauropsid β-keratins from tuatara (Sphenodon punctatus). *Journal of Structural Biology*, **207**(1), 21–28 (2019). ISSN 10958657.

Pelton JT and McLean LR. Spectroscopic Methods for Analysis of Protein Secondary Structure. *Analytical Biochemistry*, **277**(2), 167–176 (2000). ISSN 0003-2697.

Pennycuick C. *Modelling the flying bird*. Elsevier, London (2008). ISBN 0080557813.

Proctor NS and Lynch P. *Manual of ornithology : avian structure & function*. Yale University Press (1993). ISBN 0300076193.

Purslow P and Vincent JFV. Mechanical properties of primary feathers from the pigeon. *Journal of Experimental Biology*, **72**(72), 251–260 (1978).

Rajkumar BJ and Ramakrishnan V. Vibrational spectroscopic study of dl-methionine dihydrogen phosphate. *Spectrochimica Acta Part A: Molecular and Biomolecular Spectroscopy*, **57**(2), 247–254 (2001). ISSN 1386-1425.

Raman CV. A new radiation. *Proceedings of the Indian Academy of Sciences - Section A*, **37**(3), 333–341 (1953). ISSN 03700089.

Rintoul L, Carter EA, Stewart SD and Fredericks PM. Keratin orientation in wool and feathers by polarized Raman spectroscopy. *Biopolymers - Biospectroscopy Section*, **57**(1), 19–28 (2000). ISSN 00063525.

Rudall KM. X-ray studies of the distribution of protein chain types in the vertebrate epidermis. *BBA - Biochimica et Biophysica Acta* (1947). ISSN 00063002.

Schindelin J, Arganda-Carreras I, Frise E, Kaynig V, Longair M, Pietzsch T, Preibisch S, Rueden C, Saalfeld S, Schmid B, Tinevez JY, White DJ, Hartenstein V, Eliceiri K, Tomancak P and Cardona A. Fiji: an open-source platform for biological-image analysis. *Nature methods*, **9**(7), 676–82 (2012). ISSN 1548-7105.

Soons J, Herrel A, Aerts P and Dirckx J. Determination and validation of the elastic moduli of small and complex biological samples: bone and keratin in bird beaks. *Journal of the Royal Society Interface*, **9**(71), 1381 (2012). ISSN 1742-5662.

Taylor aM, Bonser RHC and Farrent JW. The influence of hydration on the tensile and compressive properties of avian keratinous tissues. *Journal of Materials Science*, **39**(3), 939–942 (2004). ISSN 00222461.

Thomas DB, McGoverin CM, McGraw KJ, James HF and Madden O. Vibrational spectroscopic analyses of unique yellow feather pigments (spheniscins) in penguins. *Journal of The Royal Society Interface*, **10**(83), 20121065–20121065 (2013). ISSN 1742-5689.

Thomas DB, Nascimbene PC, Dove CJ, Grimaldi DA and James HF. Seeking carotenoid pigments in amber-preserved fossil feathers. *Scientific Reports*, **4**, 1–71 (2014). ISSN 20452322.

Tuma R. Raman spectroscopy of proteins: From peptides to large assemblies. *Journal of Raman Spectroscopy*, **36**(4), 307–319 (2005). ISSN 03770486.

Turing AM. The chemical basis of morphogenesis. *Philosophical Transactions of the Royal Society B: Biological Sciences*, **237**(1), 72 (1953). ISSN 0092-8240.

Vallat R. Pingouin: statistics in Python Software • Review • Repository • Archive. *Journal of Open Source Software*, **3**(31), 1026 (2018).

Vincent JFV. *Structural biomaterials*. Princeton University Press (2012). ISBN 0691154007.

Wang B. *Structural and functional design strategies of biological keratinous materials*. Ph.d. thesis, UC San Diego (2016).

Wang B and Meyers MA. Seagull feather shaft: Correlation between structure and mechanical response. *Acta Biomaterialia*, **48**, 270–288 (2017). ISSN 18787568.

Wang B, Sullivan TN, Pissarenko A, Zaheri A, Espinosa HD and Meyers MA. Lessons from the Ocean: Whale Baleen Fracture Resistance (2018).

Wang B, Yang W, McKittrick J and Meyers MA. Keratin: Structure, mechanical properties, occurrence in biological organisms, and efforts at bioinspiration. *Progress in Materials Science*, **76**, 229–318 (2015). ISSN 00796425.

Wang X and Clarke JA. The evolution of avian wing shape and previously unrecognized trends in covert feathering. *Proceedings of the Royal Society B: Biological Sciences*, **282**(1816), 20151935 (2015). ISSN 0962-8452.

Wang X, McGowan AJ and Dyke G. Avian Wing Proportions and Flight Styles: First Step towards Predicting the Flight Modes of

Mesozoic Birds. *PLoS ONE*, **6**(12), e28672 (2011). ISSN 1932-6203.

Wang X, Nudds RL, Palmer C and Dyke G. Size scaling and stiffness of avian primary feathers: Implications for the flight of mesozoic birds. *Journal of Evolutionary Biology*, **25**(3), 547–555 (2012). ISSN 1010061X.

Weaver JC, Milliron GW, Miserez A, Evans-Lutterodt K, Herrera S, Gallana I, Mershon WJ, Swanson B, Zavattieri P, DiMasi E and Kisailus D. The stomatopod dactyl club: A formidable damage-tolerant biological hammer. *Science*, **336**(6086), 1275–1280 (2012). ISSN 10959203.

Weber TP, Borgudd J, Hedenström A, Persson K and Sandberg G. Resistance of flight feathers to mechanical fatigue covaries with moult strategy in two warbler species. *Biology Letters*, **1**(1), 27–30 (2005). ISSN 1744-9561.

Wegst UGK, Bai H, Saiz E, Tomsia AP and Ritchie RO. Bioinspired structural materials. *Nature Materials*, **14**(1), 23–36 (2015). ISSN 14764660.

Weiss IM and Kirchner HOK. Plasticity of two structural proteins: alpha-collagen and beta-keratin. *Journal of the mechanical behavior of biomedical materials*, **4**(5), 733–43 (2011). ISSN 1878-0180.

Willemink MJ and Noël PB. The evolution of image reconstruction for CT—from filtered back projection to artificial intelligence. *European Radiology*, **29**(5), 2185–2195 (2019). ISSN 0938-7994.

Worcester SE. The scaling of the size and stiffness of primary flight feathers. *Journal of Zoology*, **239**(3), 609–624 (1996). ISSN 09528369.

Xing L, Cockx P, McKellar RC and O'Connor JK. Ornamental feathers in Cretaceous Burmese amber: resolving the enigma of

rachis-dominated feather structure. *Journal of Palaeogeography*, **7**(1), 13 (2018). ISSN 2524-4507.

Xing L, Mckellar RC, Wang M, Bai M, O'connor JK, Benton MJ, Zhang J, Wang Y, Tseng K, Lockley MG, Li G, Zhang W, Xu X, O'Connor JK, Benton MJ, Zhang J, Wang Y, Tseng K, Lockley MG, Li G, Zhang W and Xu X. Mummified precocial bird wings in mid-Cretaceous Burmese amber. *Nature Communications*, **7**(12089), 12089 (2016). ISSN 2041-1723.

Zhang Q, Liebeck BM, Yan K, Demco DE, Körner A and Popescu C. Alpha-Helix Self-Assembly of Oligopeptides Originated From Beta-Sheet Keratin. *Macromolecular Chemistry and Physics*, **213**(24), 2628–2638 (2012). ISSN 10221352.

Zhang W, Soman P, Meggs K, Qu X and Chen S. Tuning the Poisson's Ratio of Biomaterials for Investigating Cellular Response. *Advanced functional materials*, **23**(25) (2013). ISSN 1616-301X.

Zhao W, Yang R, Zhang Y and Wu L. Sustainable and practical utilization of feather keratin by an innovative physicochemical pretreatment: high density steam flash-explosion. *Green Chemistry*, **14**(12), 3352 (2012). ISSN 1463-9262.

Appendix

Appendix A

List of Publications

A.1 Journal Articles

Laurent, C.M., de Kat, R., Hillenius, J & Maderson, P.F.A. (In Prep) Feather structure and development: why does the barb hinge lack pith?

Laurent, C.M., Wang, X. & Li, Z. (In Review) Exceptional preservation of feather microstructures in amber from the Middle-Cretaceous of Myanmar.

Laurent, C.M., Dyke, G., Cook, R., Dyke, J. & De Kat, R. (2020) Spectroscopy on the Wing: Investigating possible differences in protein secondary structures infeather shafts of birds using Raman spectroscopy. Journal of Structural Biology, 211 (1) 107529.

Laurent, C.M., Ahmed, S.I., Boardman, R.P., Cook, R.B., Dyke, G., Palmer, C., Schneider, P., & DeKat, R. (2019) Imaging techniques for observing laminar geometry in the feather shaft cortex. *Journal of Microscopy* 277(3) 2019, pp. 1–6

Zitouni, S., **Laurent, C.M.**, Dyke, G. & Jalil, N. (2019) An Abelisaurid Ilium from the Upper Cretaceous (Cenomanian) of Morocco. *Plos ONE* 14(4) e0214055

Fernandez, M.S, Wang, X., Vremir, M. **Laurent, C.M.**, Naish,

D. Kaiser, G & Dyke, G. (2019) A mixed vertebrate nesting assemblage from the Transylvanian Late Cretaceous. *Nature Scientific Reports, 9,(1) 1944*

Laurent, C. M. (2016). Review: Evolutionary Biomechanics: Selection , Phylogeny and Constraint. Quarterly Review of Biology, 90(2).

Laurent, C. M., Palmer, C., Boardman, R. P., Dyke, G., & Cook, R. B. (2014). Nanomechanical properties of bird feather rachises: exploring naturally occurring fibre reinforced laminar composites. Journal of The Royal Society Interface, 11(101).

A.2 Conference presentations

Laurent, C. M. & Dyke, G. - The rediscovery of Burmite and it's palaeontological significance for understanding the development of Avian flight in the mid-Cretaceous. 12th Romanian Symposium of Palaeontology, Cluj-Napoca, Romania. 2019.

Dyke, G., **Laurent, C. M.** & Lendvai, A. The evolution of bird feathers: New and old evidence from the fossil record. 12th Romanian Symposium of Palaeontology, Cluj-Napoca, Romania. 2019.

Laurent, C.M., Ahmed, S.I. Cook, R. B. & de Kat, R. Natural laminates: automated fibre direction and layer thickness from synchrotron CT scans of feathers, 7th Annual Meeting of "Tomography for Scientific Advancement (ToScA)", Southampton, UK. 2018. UK. 2019.

Laurent, C. M., Lendvai, Á., Kövecsi, Sz.-A. & Dyke, G. Fossil evidence for the evolution of feather structure. Ioan Popescu Voitesti Annual Scientific Session, Babeş-Bolyai University, Cluj-Napoca, Romania. 2018.

Laurent, C.M., Ahmed, S.I. Cook, R. B. & de Kat, R. Quantifying laminar layup around and along a bird feather shaft. 6th Annual Meeting of "Tomography for Scientific Advance-

ment (ToScA)", Warwick, UK. 2018.

Dyke, G., **Laurent, C.M**, Lendvai, Á., Kövecsi, Sz.-A. & Manciu, R. Documenting the evolution of avian wing shapes. 19th Annual Meeting of the "Gesellschaft für Biologische Systematic Vienna", Austria. 2018

Laurent, C.M., Ahmed, S.I., Cook, R. B. & de Kat, R. (2018) Inside a feather II: Quantifying laminar layup around and along a bird feather shaft. Society for Integrative and Comparative Biology Annual Meeting, San Francisco USA.

Dyke, G., **Laurent, C.M.**, Lendvai, Á., Kövecsi, Sz.-A. & Manciu., R. Documenting the evolution of avian wing shapes (BIRDWING). Ioan Popescu Voitesti Annual Scientific Session, Babeş-Bolyai University, Cluj-Napoca, Romania. 2017

Laurent, C.M., Schneider, P., Dyke, G., Boardman, R. P., Palmer, C., Cook, R. B. & de Kat, R. (2017) Inside a feather: laminar layup varies around and along bird feather shafts. Wessex DTN Annual Congress.

Laurent, C.M., Schneider, P., Dyke, G., Boardman, R. P., Palmer, C., Cook, R. B. & de Kat, R. (2017) Inside a feather: laminar layup varies around and along bird feather shafts. Society for Integrative and Comparative Biology Annual Meeting, New Orleans USA.

A.3 Invited talks

Laurent, C.M. (2018) The evolution, form and function of feathers. Institute of Zoology, Chinese Academy of Sciences, Beijing, China.

Laurent, C.M. (2017) Synchrotron CT scanning of natural fibrous materials. University of Nyiregyhaza, Hungary.

Laurent, C.M. (2017) Inside a feather. Wessex DTN Annual Congress. University of Bristol, UK.

Laurent, C.M. (2017) Feathers, fibres and forces. University of Debrecen, Hungary.

Laurent, C.M. (2017) Raman spectroscopy: a powerful technique in structural biology. University of Debrecen, Hungary.

Laurent, C.M. (2016) The mechanical properties of primary flight feathers. University of Debrecen, Hungary.

Laurent, C.M. (2016) The mechanical properties of primary flight feathers. University of Babeş Bolyai, Romania.

Laurent, C.M. (2015) The evolution of the integument. Vertebrate evolution and phylogenetics lecture series. National Oceanography Centre, UK.

Laurent, C.M. (2014) The evolution of the integument. Vertebrate evolution and phylogenetics lecture series. National Oceanography Centre, UK.

Curriculum Vitae

Christian Laurent was born in January 1992 in London. He attended Dartford Grammar School from 2003-2010 before he studied Marine Biology and Oceanography at the University of Southampton. He met Dr Gareth Dyke and Dr Colin Palmer, palaeontologists working on the evolution of flight, whilst studying a module on Vertebrate Phylogenetics. He wrote a Master of Research thesis under their tutelage, which resulted in a publication in *J.R. Soc Interface*. Toward the end of his Master's year (2014) he proposed a Ph.D project to continue his work, before leaving to work as a SCUBA instructor in Indonesia. A few months later his studentship had received funding from two scholarships and he was accepted on a programme to begin the following academic year.

In October 2014 he started his doctoral project, also at the University of Southampton, under the principal supervision of Dr Roeland De Kat, an aerodynamicist. The project involved elements of engineering, imaging, biology and chemistry and so he continued to be supervised by Dr Dyke and Dr Palmer, palaeontologists, as well as Dr Richard Cook, a tribologist; Dr Richard Boardman, a physicist working with Computed Tomography; Dr Phillip Schneider, a bio-engineer and imaging specialist; and Professor John Dyke, a physical chemist. The results of this work have been presented above.

During this time he was involved in teaching vertebrate phylogenetics at the National Oceanography Centre (School of Ocean and Earth Science), elementary programming with Python (School

of Engineering) and nozzle aerodynamics (School of Engineering).

He visited Switzerland on multiple occasions to conduct X-Ray Computed Tomography experiments at the Swiss Light Source. This work resulted in a number of conference presentations in the USA and the UK, notably including one of the first 3D exhibitions and definitely the first VR exhibition at the annual meeting of the Society for Integrative and Comparative Biology (4000 members). He conducted similar experiments at the Diamond Light Source in Oxford, and gave a number of invited lectures in Hungary and Romania.

Later, he won an EU grant with Dr Gareth Dyke at Babeș-Bolyai University in Romania, to work full-time for 18 months using structured light to image the surface of bird wings, work which had to be balanced with his continuing doctoral studies.

In April 2018 he visited Beijing to spend three months working at the Institute for Vertebrate Palaeontology and Palaeoanthropology, Chinese Academy of Sciences, to describe feathers preserved in Burmese amber.

He passed his PhD examination, without corrections, under the examination of Professor Adrian Thomas (University of Oxford) and Dr Neil Gostling (University of Southampton) in May 2020.

ISBN 978-1-83853-556-8